UNIVERSITÀ TELEMATICA INTERNAZIONALE UNINETTUNO

FACOLTÀ DI INGEGNERIA

Dottorato di Ricerca in Ingegneria dell'Innovazione Tecnologica

Ciclo
XXXV

Quasi static and dynamic problems in strain gradient (granular) micromechanics

COORDINATORE
Prof. Clemente Cesarano

CANDIDATO
Dott. Valerii Maksimov

SUPERVISORE
Prof. Luca Placidi

Abstract

This work presents a comprehensive continuum theory for 2D strain gradient materials that accounts for a class of dissipation phenomena. The continuum description is constructed by means of a reversible placement function and irreversible damage and plastic functions. In addition to specifying expressions for elastic and dissipation energies, we postulate a hemi-variational principle to derive strain gradient Partial Differential Equations (PDEs), boundary conditions (BCs), and Karush-Kuhn-Tucker (KKT) type conditions. Unlike previous models, our approach does not assume flow rules, and plastic deformation can be derived through the placement function. The derived PDEs and BCs govern the evolution of the placement descriptor, while the KKT conditions govern the damage and plastic variables. To demonstrate the applicability of our model, we conduct numerical experiments on homogeneous cases, which do not require Finite Element simulations. We investigate the induced anisotropy of the response and demonstrate the coupling between damage and plasticity evolution.

Using finite element method this work analyzes the mechanical behavior of materials with granular microstructures in two dimensions using a strain-gradient continuum approach based on micromechanics. We account for tension-compression asymmetry of grain-assembly interactions and microscale damage while linking the continuum scale to the grain-scale mechanisms. Overall, our approach captures microstructural-size-dependent effects and provides a comprehensive understanding of the mechanical behavior of materials with granular microstructures.

It has been showed that a granular micromechanics approach can lead to load-path dependent continuum models. In this study, we extend this approach by introducing an intrinsic 2nd gradient energy storage mechanism in the grain-grain interaction, similar to a pantographic micromechanism. We homogenize the approach and determine the macro-scale mechanical behavior, varying the averaged intergranular distance and the stiffness associated with the pantographic term. Results show that the inclusion of the pantographic term allows for successful modeling and fine-tuning of the desired thickness of the localization zone. Furthermore, we demonstrate that the complex mechanics of load-path dependency can be predicted through micromechanical effects and the introduced pantographic term. Given approach could be used not only in quasi-static but also in dynamic problem. This work presents a dynamic model for the propagation of fractures in materials subjected to strain gradients. The proposed model accounts for the effects of material heterogeneity and microstructure on the fracture behavior by incorporating a strain gradient term into the governing equations. The model is based on a continuum mechanics framework and uses a variational formulation to derive the equations of motion. The numerical implementation is carried out using the finite element method, and the results are validated against experimental data from literature. The simulations show that the strain gradient has a significant effect on the fracture patterns and propagation velocity, especially in materials with small length scales. This work provides a valuable tool for predicting and analyzing fracture behavior in microstructured materials, with potential applications in the design of advanced materials and structures.

List of publications

1. Luca Placidi, Emilio Barchiesi, Francesco Dell'Isola, Valerii Maksimov, Anil Misra, et al.. On a hemi- variational formulation for a 2D elasto-plastic-damage strain gradient solid with granular microstructure. Mathematics in Engineering, AIMS, 2022, 5, pp.1 - 24. 10.3934/mine.2023021 . hal-03700024

2. Valerii Maksimov, Emilio Barchiesi, Anil Misra, Luca Placidi, Dmitry Timofeev. Two-Dimensional Analysis of Size Effects in Strain-Gradient Granular Solids with Damage-Induced Anisotropy Evolution. Journal of Engineering Mechanics. 2021,147(11). doi:10.1061/(ASCE)EM.1943-7889.0002010

3. Luca Placidi, Dmitry Timofeev, Valerii Maksimov, Emilio Barchiesi, Alessandro Ciallella, Anil Misra, Francesco dell'Isola. Micro-mechano-morphology-informed continuum damage modeling with intrinsic 2nd gradient (pantographic) grain-grain interactions. International Journal of Solids and Structures. https://doi.org/10.1016/j.ijsolstr.2022.111880

4. Valerii Maksimov, Luca Placidi, Emilio Barchiesi, Anil Misra, Francisco James León Trujillo. Dynamic modeling of strain gradient fracture propagation. In work

Contents

Chapter 1

Introduction

1.1 Background

Granular materials are ubiquitous in nature and engineering applications, including soil, rock, concrete, powders, and grains . Understanding the mechanics of granular materials is critical for predicting their deformation behavior under various loading and environmental conditions. However, granular materials exhibit complex and diverse deformation behavior, making their mechanics challenging to model and predict.

In recent years, there has been a growing interest in the development of strain gradient-based models for granular materials. Strain gradient theories account for the size-dependent behavior of materials and have been shown to provide more accurate predictions for micro-scale deformation and damage. These models capture the effects of microstructural features on the macroscopic deformation behavior of granular materials.

The development of these models has been driven by the need to understand the behavior of granular materials in geomechanics, civil engineering, and material science applications. For example, in geomechanics, the behavior of soils and rocks is critical for predicting landslides, slope stability, and seismic hazard assessment. In civil engineering, the deformation and failure behavior of concrete and masonry structures is essential for design and maintenance. In material science, granular materials are used in the development of new composites and biomaterials.

This thesis focuses on the mechanics of granular materials using strain gradient-based models. Specifically, the thesis investigates the deformation and damage behavior of strain gradient granular solids with a granular microstructure. The studies presented in this thesis aim to contribute to the development of more accurate and reliable models for predicting the deformation behavior of granular materials. These models can be used in practical applications to improve the design, analysis, and maintenance of structures and materials.

The study of dynamic fracture involves analyzing the breakdown and malfunction of materials and structures in situations where the impact of inertia needs to be taken into account. Fracture phenomena such as dynamic crack propagation and branching are frequently observed in various engineering materials and structures. When subjected to dynamic loading conditions, the failure process of these materials and structures is catastrophic due to the influence of inertia effects.

1.2 Motivation of the work

Numerical simulation is a crucial tool in many fields: numerical simulation is widely used in fields such as engineering, physics, biology, and finance, among others. This is because numerical simulation allows researchers and practitioners to study complex systems that are difficult or impossible to analyze through experimental or analytical methods alone. By using numerical simulation, researchers can obtain detailed information about how a

system behaves, which can inform decision-making and improve our understanding of the world around us.

Most of the software which are used to make numerical simulations in engineering give results that are mesh dependent. In [37] it was showed that using Abaqus software it is possible to simulate 3D problem. The prediction shows very good comparison with experimental data, however the results are mesh dependent. On the one hand, the finer the mesh of finite elements, the better the fit with the experimental data 1.1, and on the other hand, the computational time increases considerably. Obtaining mesh-independent results is an essential task in many fields that rely on simulations, for example in structural mechanics. The accuracy and reliability of simulation results can be affected by several factors, including the size and quality of the mesh used.

One effective approach to achieving mesh-independent results is to use a second-order discretization scheme in the numerical method used to solve the governing equations. This means that the approximation of the solution at each point in the mesh is made with an increased level of accuracy, resulting in more precise and physically accurate results. The use of a second-order scheme can lead to a more efficient and accurate simulation, particularly in cases where the flow behavior is complex or where small-scale features are present.

Additionally, other techniques such as mesh refinement, mesh smoothing, and mesh adaptation can also be used in conjunction with a second-order approach to further improve the quality of the mesh and ensure that the solution is not overly sensitive to the mesh. These techniques involve iteratively refining the mesh in regions where the solution is not well-resolved, smoothing the mesh to eliminate grid-induced numerical noise, and adapting the mesh to better capture the flow behavior.

Overall, utilizing a second-order approach is a critical step in obtaining mesh-independent results, which are necessary for accurate and reliable simulations in a variety of fields. By ensuring that the solution is not overly sensitive to the mesh, engineers and researchers can have greater confidence in the results obtained from their simulations and make more informed decisions based on these results.

1.3 Dissipation in granular media

The scientific literature [19, 29, 48, 45, 79] extensively discusses approaches for handling dissipation in non-conservative physical systems, particularly regarding complex dissipative phenomena like damage and plasticity. These phenomena are of particular interest to the engineering community as they occur in various engineering materials [49, 50, 95], such as structural steel and concrete. However, it is often difficult and economically unfeasible to experimentally validate [55, 80, 5, 86] the tolerance of new architectures to damage and plastic effects, beyond scaled-down trials, with design load cases remaining untested. Therefore, there is an increasing need for reliable modeling and numerical protocols to accurately predict the behavior of structures subjected to damage and plastic effects, addressing this challenge.

Describing complex dissipative phenomena like damage and plasticity presents significant challenges, especially for materials with complex structures like lattices [84, 26, 63] or granular [49, 51] microstructures. In recent years, continuum approaches to modeling damage [1, 2] and plasticity [17, 3, 22, 23, 24, 40, 49, 50, 75, 76] have been developed, including phase field models [4, 7, 8, 82, 44, 42] for analyzing fractures and shear bands. Multiscale approaches [27, 31, 28] that connect low-level descriptions with the continuum have also been proposed [15, 33] to capture complex behavior in the continuum. However, the challenge in damage mechanics is that loss of stiffness and mechanical failure often lead to localized deformation [66, 67], which classical fracture mechanics and damage mechanics struggle to accurately predict. Classical linear elastic fracture mechanics cannot anticipate weakening or nucleation of defects in areas far from existing cracks or boundaries that arise due to material damage or weakness [87, 69]. Similarly, classical damage mechanics experiences instabilities linked to loss of ellipticity, which requires regularization, particularly for simulating coalescence of microfractures and producing results that are independent of numerical simulation's mesh size and shape [39, 85, 21, 12, 9].

In granular micromechanics [70, 49], the objective grain-grain relative displacement is divided into two com-

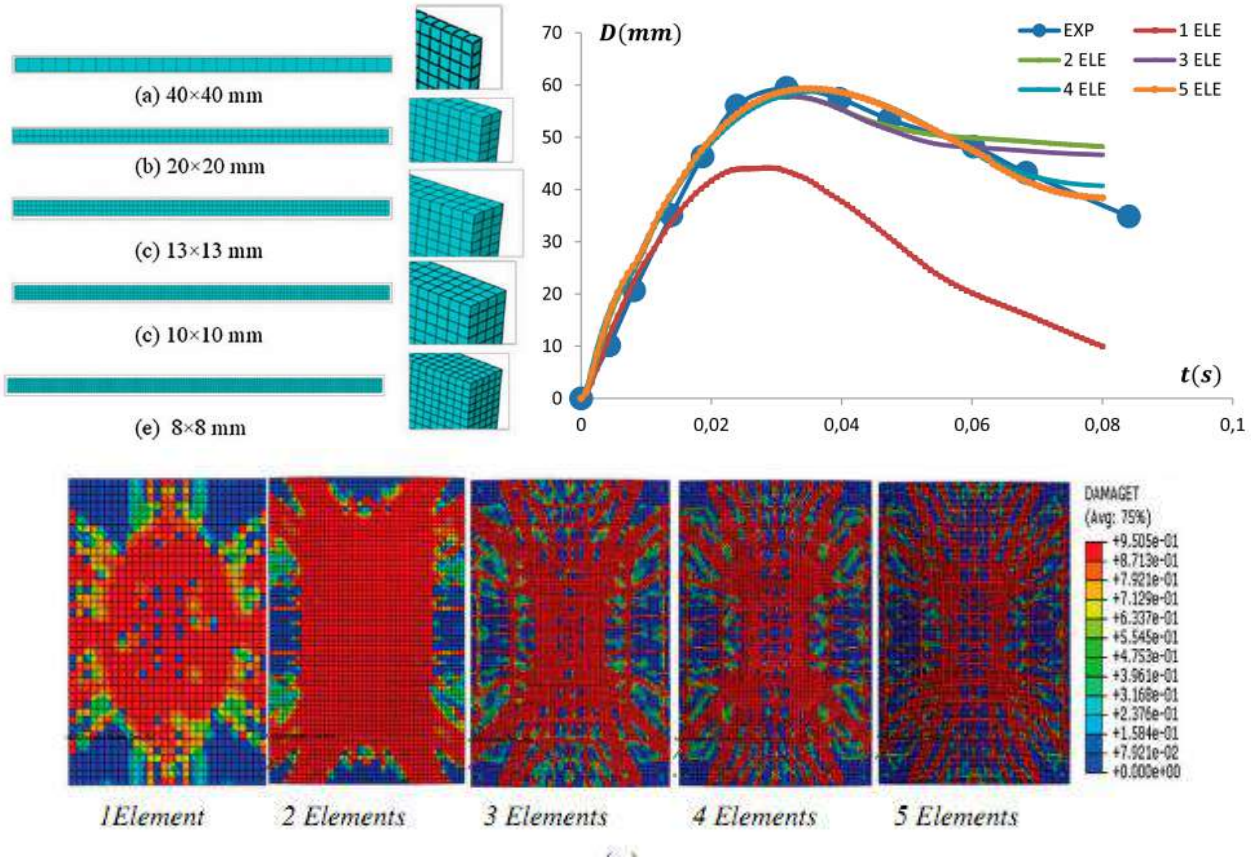

Figure 1.1: Comparison the numerical results with respect to the mesh size.

ponents: the normal component and the tangent component. These components are further decomposed [78, 77] into elastic and plastic parts, which are used to define elastic strain and dissipation energy functions for each grain-grain interaction. Damage is described using normal and tangent damage variables, with only plastic relative displacement in the normal direction being considered. Plastic relative displacement in the tangent direction is not considered because it is not a plastic multiplier and does not affect the results. Numerical results obtained using cyclic loading-unloading histories will be presented to show the hysteretic features of the continuum, and the load-free shape will be used to assess plastic behavior. This approach ensures that plastic strain is compatible with the existence of a placement function, which is not always the case in existing approaches and requires additional compatibility conditions or remedies.

The grain-grain interaction can be simplified as two springs, one for the normal component and one for the tangent component, that experience damage and plastic effects. However, to create a more representative continuum model, an additional energy storage mechanism needs to be introduced that accounts for long-range effects beyond nearest neighbors. This mechanism involves a spring at the micro-scale that accumulates energy based on the gradient of its stretch. At a lower scale, this mechanism can be represented by a pantographic beam with fixed stretch at boundaries, which deforms mainly along the axial direction with low slenderness. This pantographic term can be seen as not only accounting for long-range interactions, but also as a term derived from modeling an actual pantographic sub-structure embedded within grain-grain interactions. In fact, this sub-structure could potentially be created using 3D printing technology in the context of a granular metamaterial [30, 52, 18, 53].

The elastic behavior of the damaged material is determined by the total elastic strain energy, which is expressed in terms of the strain energies associated with each grain-grain interaction. This leads to relationships for first gradient, second gradient, and first-second-gradient interaction elastic module as functions of micro-mechano-morphological

parameters and damage variables. A hemi-variational approach [14, 62, 66, 64, 67, 68, 65] is used to derive Karush-Kuhn-Tucker conditions that lead to evolution equations for grain-grain damage and plastic kinematic variables, as well as Euler-Lagrange equations for the evolution of grain-grain total relative displacement.

It is important to mention that in a granular system, grain-pairs are oriented in different directions. As a result, when subjected to a given loading sequence, they will undergo different loading histories, leading to different damage and plastic evolution for differently-oriented grain-grain interactions. Moreover, damage is defined for both normal and tangential directions, and plasticity is characterized by two plastic multipliers, one for the accumulation of normal plastic relative displacement in tension and another for compression. This results in a highly complex and path-dependent macroscopic response.

1.4 Objectives

In this work, the goal is to create a model for granular media using the variational approach, which is a mathematical method for finding optimal solutions. The model aims to capture the unique properties of granular materials, which are referred to as micro-mechano-morphology. It also takes into account the effects of damage, which is an important dissipative phenomenon that occurs in granular media. Dynamic simulation is a common technique used to study the behavior of granular materials under different conditions, such as stress, strain, and deformation. By incorporating dynamic simulation into the model, researchers can better understand the complex behavior of granular media and design more effective materials for various applications.

Therefore, intermediate objectives of the thesis can be listed as follows:

1. Propose a suitable way to describe how grains interact with each other by using kinematic descriptors that are based on the relative motion of the grain centroids.
2. Create an equation for elastic energy that includes second-gradient terms.
3. Suggest a way to account for dissipation energy that takes into consideration the tension/compression asymmetry of damage.
4. Use a hemi-variational principle to derive the Euler-Lagrange equations and Karush-Kuhn-Tucker (KKT) type conditions to describe evolution of the system.
5. Develop a numerical algorithm to implement the model and solve non-homogeneous problems that lack analytical solutions.
6. Perform a series of numerical experiments to investigate the applicability of the model.
7. Study the mesh-independence of the proposed approach to granular media.
8. Catch the effect of the force of inertia in a dynamic problem.

1.5 Outline

The materials of this thesis is organized as follows.

Chapter 2 recaps and updates a recently developed continuum model for granular materials in order to handle with those important dissipative phenomena as damage and plasticity. A hemi-variational principle was adopted to derive the governing equations, from which we obtain Karush-Kuhn-Tucker (KKT)-kind conditions that specify the progression of damage and plasticity relating to each pair of grains interaction.

Chapter 3 analyze the size effects observed from the results of numerical extension tests.

Chapter 4 is concerned with enhanced, pantographic integranular interaction and explores it by means of numerical simulations with load path dependency.

Chapter 5 analyze the inertia effect and load rate dependence from results of numerical extension tests.

Chapter 6 is left to concluding remarks and perspectives.

Chapter 2

On a hemi-variational formulation for a 2D elasto-plastic-damage strain gradient solid with granular microstructure

Mathematics in Engineering, 5(1): 1–24.
DOI:10.3934/mine.2023021
Received: 25 September 2021
Revised: 21 January 2022
Accepted: 26 January 2022
Published: 29 March 2022

http://www.aimspress.com/journal/mine

Research article

On a hemi-variational formulation for a 2D elasto-plastic-damage strain gradient solid with granular microstructure†

Luca Placidi[1,*], Emilio Barchiesi[2,3,5], Francesco dell'Isola[2], Valerii Maksimov[1], Anil Misra[4], Nasrin Rezaei[1], Angelo Scrofani[2] and Dmitry Timofeev[2]

[1] Faculty of Engineering, International Telematic University UNINETTUNO, Rome, Italy

[2] International Research Center on Mathematics and Mechanics of Complex Systems (M&MoCS), Università degli Studi dell'Aquila, L'Aquila, Italy

[3] École Nationale d'Ingénieurs de Brest, 760 ENIB, UMR CNRS 6027, IRDL, F-29200 Brest, France

[4] Civil, Environmental and Architectural Engineering Department, The University of Kansas, Kansas City, Kansas, USA

[5] Université de Bretagne Sud, Rue de Saint Maudé - BP 92116 56321, Lorient, Cedex, France

† **This contribution is part of the Special Issue:** Models and Methods for Multiscale Systems
Guest Editor: Giulio Giusteri
Link: www.aimspress.com/mine/article/5814/special-articles

* **Correspondence:** Email: luca.placidi@uninettunouniversity.net; Tel: 066920761 Ext. 217.

Abstract: We report a continuum theory for 2D strain gradient materials accounting for a class of dissipation phenomena. The continuum description is constructed by means of a (reversible) placement function and by (irreversible) damage and plastic functions. Besides, expressions of elastic and dissipation energies have been assumed as well as the postulation of a hemi-variational principle. No flow rules have been assumed and plastic deformation is also compatible , that means it can be derived by a placement function. Strain gradient Partial Differential Equations (PDEs), boundary conditions (BCs) and Karush-Kuhn-Tucker (KKT) type conditions are derived by a hemi variational principle. PDEs and BCs govern the evolution of the placement descriptor and KKT conditions that of damage and plastic variables. Numerical experiments for the investigated homogeneous cases do not need the use of Finite Element simulations and have been performed to show the applicability of the model. In particular, the induced anisotropy of the response has been investigated and the coupling between damage and plasticity evolution has been shown.

Keywords: damage mechanics; granular microstructures; Karush-Kuhn-Tucker conditions; strain gradient; 2D continua

1. Introduction

A large amount of scientific literature deals with non-conservative physical systems, where it is necessary to use methods that are able to handle the related dissipation phenomena [3, 16, 28, 38, 54]. In engineering applications [39, 40, 62] a wide range of materials, like steel and concrete, experience dissipative phenomena such as damage and plasticity. That is why they are especially interesting for the engineering community. But building accurate description of these phenomena can be very difficult, especially for complex material systems like granular [39] or lattice-type [25, 58] microstructure. Continuum damage [1, 8] and plasticity [4, 9, 17, 22–24, 32, 39, 40, 49, 50] modeling have been vigorously pursued in the literature, considering the improvements based on phase field models [10, 13, 14, 33, 35, 55] for shear bands and fracture. Multi-scale approaches [6, 27, 34, 42] , in addition to phenomenological ones [56, 57], have been proposed. Their purpose is to link low-scale descriptions with continuum [15, 29, 31] to include complex emerging behaviors in the continuum. Besides, the strain gradient regularization of the elastic response [26, 30] should be considered also in this non conservative context. In this paper we recap, in a new and better way, recently developed continuum model for granular materials undergoing damage and plastic deformations. Damage and plasticity are irreversible phenomena [2, 32, 49, 50]. In this model, the irreversibility is taken into account by assuming that damage and plastic variables are non-decreasing quantities in time [59]. It has been extensively discussed in the literature, that deformed shapes of granular materials may be described in a continuum model by using the relative displacements of the barycenters of the grains, regardless their deformations. Thus, in a coarse-grained description, for a material with a granular micro-structure, the deformation energy as well as the energy dissipated due to damage and plasticity, are expressed in terms of these relative movements. The volumetric energy of deformation, i.e., the deformation energy per unit volume, is assumed to be the sum of deformation energies associated with each intergranular interaction. Each grain-grain interaction is identified by the orientation of the grain-grain direction that, in the continuum limit, are infinite in number. This approach has shown its efficiency in describing granular systems, both at the discrete and at the continuum levels [5, 7, 18, 37, 51, 60, 61]. We also use a variational approach [20, 21]. First of all, we define an objective and reversible kinematic vector variable to measure the relative displacements between grains. Thus, we decompose the objective relative displacement between the grains [39, 48] into two components. The first one is directed along the vector connecting the grain centroids, and it is called the normal component. The second is directed along the orthogonal direction and is called the tangent component. These components are decomposed into elastic and plastic parts. The functionals of elastic deformation and of dissipation energy are defined in terms of these reversible components [52, 53] and of irreversible damage and plastic variables. Damage is defined by two variables, i.e., the normal and the tangential damage variables, that are both a function of grain-grain orientation. On the one part, plastic displacement does not have to be non-decreasing in time. On the other part, it is characterized as the difference between two non-diminishing plastic variables, that are the accumulated plastic relative displacement in tension and in compression, respectively. The evolution of the form of the body that is obtained without external load defines in this approach the evolution of the plastic strain. The elastic evolution of the damaged material is defined by the total elastic strain energy. This type of energy is explained in terms of the elastic energies related to each intergranular orientation. Therefore, dependencies are obtained for the standard elastic modules (4th

order stiffness tensor), of the second gradient elastic modules (6th order stiffness tensor) and of the chiral interaction modules (5th order stiffness tensor). They are functions of parameters describing the damage-elasto-plastic state, describing micro-mechano-morphology, of each orientation. Besides, because of plastic effects, we obtain an expression also of the pre-stress (2nd order tensor) and of the pre-hyperstress (3rd order tensor). The hemi-variational approach [43–46] has been used to obtain Karush-Kuhn-Tucker (KKT) kind conditions, that drive the evolution of damage and plastic irreversible kinematic variables. According to the same derivation, also the Euler-Lagrange equations for the progress of the reversible placement function is obtained. It is worth to be noted that, since grain-pairs are oriented in different directions, for a given loading-sequence, they experience different loads and hence different damage and plastic evolution. Thus, the macroscopic response will be complex and with an intrinsically dependence upon path.

The content of this paper is organized as follows. Section 2 provides a rational recap of the model that was introduced in papers [12,41,44,47,59]. Section 3 provides the scheme of a possible numerical (or analytical) implementation of the model. Section 4 is devoted to the representation of the results for the homogeneous case, where no Finite Element implementation is necessary for the illustration of the results. Section 5 addresses a few concluding comments and future viewpoints.

2. A rational recap of the model

In this section we will recap the model that has been investigated by the authors more widely in different papers [12, 41, 44, 47, 59].

2.1. The elastic energy per unit area

Let $\mathcal{B}$ be the $2D$ reference configuration of a strain gradient elastic body. Its elastic energy U per unit area is assumed to take the following form

$$U = \int_{\mathcal{S}^1} \left[\frac{1}{2} k_{\eta,D} \left(u_\eta^{el} \right)^2 + \frac{1}{2} k_{\tau,D} \left(u_\tau^2 \right) \right], \qquad \forall \boldsymbol{X} \in \mathcal{B} \tag{2.1}$$

where the elastic part u_η^{el} of the normal displacement u_η is postulated be equal to the difference of the total normal displacement u_η and its plastic part u_η^{pl}

$$u_\eta^{el} = u_\eta - u_\eta^{pl}, \tag{2.2}$$

where u_τ is the tangential displacement and both are defined as follows,

$$u_\eta = L G_{ij} \hat{c}_i \hat{c}_j + \frac{L^2}{4} G_{ij,h} \hat{c}_i \hat{c}_j \hat{c}_h, \tag{2.3}$$

$$u_\tau^2 = 4L^2 G_{ij} G_{ab} \left(\delta_{ia} \hat{c}_j \hat{c}_b - \hat{c}_i \hat{c}_j \hat{c}_a \hat{c}_b \right) + 2L^3 G_{ij} G_{ab,c} \left(\delta_{ia} \hat{c}_j \hat{c}_b \hat{c}_c - \hat{c}_i \hat{c}_j \hat{c}_a \hat{c}_b \hat{c}_c \right) \tag{2.4}$$

$$+ \frac{L^4}{4} G_{ij,h} G_{am,n} \left(\delta_{ia} \hat{c}_j \hat{c}_h \hat{c}_m \hat{c}_n - \hat{c}_i \hat{c}_j \hat{c}_h \hat{c}_a \hat{c}_b \hat{c}_c \right),$$

where the unit vector $\hat{c}$ gives the direction of the considered grain-pair interaction and the domain $\mathcal{S}^1$ is the unit circle to which it belongs; the Green-Saint-Venant tensor G and its gradient are tensors of a 2nd and 3rd order,

$$G = \frac{1}{2} \left(F^T F - I \right), \quad \nabla G = F^T \nabla F, \tag{2.5}$$

respectively, where the deformation gradient F and its gradient are defined

$$F = \nabla \boldsymbol{\chi}, \qquad \nabla F = \nabla \left(\nabla \boldsymbol{\chi} \right) \tag{2.6}$$

in terms of the placement function $\boldsymbol{\chi}(\boldsymbol{X}, t)$, that is a function of the position X and of time t. In Eq (2.3) and (2.4), L is the averaged grain-pair distance. Besides, the damaged tangent stiffness is $k_{\tau,D}$ and the damaged normal stiffness is $k_{\eta,D}$. The damaged normal stiffness is assumed to be asymmetric in tension and compression, i.e.,

$$k_{\eta,D} = k^t_{\eta,D} \Theta \left(u^{el}_\eta \right) + k^c_{\eta,D} \Theta \left(-u^{el}_\eta \right), \tag{2.7}$$

where $k^t_{\eta,D}$ is the stiffness in tension that is assumed to be smaller than the stiffness in compression $k^c_{\eta,D} \gg k^t_{\eta,D}$. Besides, the dividing line between tension and compression is given by the sign of the elastic normal displacement u^{el}_η. Thus, the Heaviside function Θ is here used. Damage is modeled, as we have already pointed out, with two variables, i.e., the normal damage D_η, and the tangent damage D_τ. The damage variables D_η and D_τ have the role to reduce the damaged normal stiffness $k_{\eta,D}$ (2.7) and the damaged tangent stiffness $k_{\tau,D}$, respectively,

$$k_{\eta,D} = k_\eta \left(1 - D_\eta \right), \qquad k_{\tau,D} = k_\tau \left(1 - D_\tau \right), \tag{2.8}$$

where the non-damaged normal stiffness k_η and the non-damaged tangent stiffness k_τ have been introduced. Definitions of non-damaged tension (k^t_η) and compression (k^c_η) normal stiffness through the following expressions

$$k^t_{\eta,D} = k^t_\eta \left(1 - D_\eta \right), \qquad k^c_{\eta,D} = k^c_\eta \left(1 - D_\eta \right), \tag{2.9}$$

yield the analogous of (2.7) for the non-damaged normal stiffness, i.e.,

$$k_\eta = k^t_\eta \Theta \left(u^{el}_\eta \right) + k^c_\eta \Theta \left(-u^{el}_\eta \right). \tag{2.10}$$

We therefore obtain, by insertion of (2.10) into $(2.8)_1$, the following expression for the damaged normal stiffness

$$k_{\eta,D} = k_\eta \left(1 - D_\eta \right) = k^t_\eta \left(1 - D_\eta \right) \Theta \left(u^{el}_\eta \right) + k^c_\eta \left(1 - D_\eta \right) \Theta \left(-u^{el}_\eta \right). \tag{2.11}$$

Insertion of (2.2), (2.3), (2.4) and (2.8) into (2.1) yield the elastic energy per unit area in a more compact form as

$$U = \frac{1}{2} \mathbb{C}_{ijab} G_{ij} G_{ab} + \mathbb{M}_{ijabc} G_{ij} G_{ab,c} + \frac{1}{2} \mathbb{D}_{ijhabc} G_{ij,h} G_{ab,c} + \mathbb{P}_{ij} G_{ij} + \mathbb{Q}_{ijh} G_{ij,h}, \tag{2.12}$$

where, accounting for the symmetrization induced by the symmetry of the strain tensor G, the elastic stiffnesses $\mathbb{C}$, $\mathbb{M}$, $\mathbb{D}$, $\mathbb{P}$ and $\mathbb{Q}$ are identified as follows

$$\begin{aligned} \mathbb{C}_{ijab} &= L^2 \int_{\mathcal{S}^1} k_\eta \left(1 - D_\eta \right) \hat{c}_i \hat{c}_j \hat{c}_a \hat{c}_b \\ &+ L^2 \int_{\mathcal{S}^1} k_\tau \left(1 - D_\tau \right) \left(\left(\delta_{ia} \hat{c}_j \hat{c}_b + \delta_{ib} \hat{c}_j \hat{c}_a + \delta_{ja} \hat{c}_i \hat{c}_b + \delta_{jb} \hat{c}_i \hat{c}_a \right) - 4 \hat{c}_i \hat{c}_j \hat{c}_a \hat{c}_b \right) \end{aligned} \tag{2.13}$$

$$\mathbb{M}_{ijabc} = \frac{1}{4}L^3 \int_{\mathcal{S}^1} k_\eta \left(1 - D_\eta\right) \hat{c}_i \hat{c}_j \hat{c}_a \hat{c}_b \hat{c}_c \tag{2.14}$$
$$+\frac{1}{4}L^3 \int_{\mathcal{S}^1} k_\tau \left(1 - D_\tau\right) \left(\left(\delta_{ia}\hat{c}_j\hat{c}_b + \delta_{ib}\hat{c}_j\hat{c}_a + \delta_{ja}\hat{c}_i\hat{c}_b + \delta_{jb}\hat{c}_i\hat{c}_a\right)\hat{c}_c - 4\hat{c}_i\hat{c}_j\hat{c}_a\hat{c}_b\hat{c}_c\right)$$
$$\mathbb{D}_{ijhabc} = \frac{1}{16}L^4 \int_{\mathcal{S}^1} k_\eta \left(1 - D_\eta\right) \hat{c}_i \hat{c}_j \hat{c}_h \hat{c}_a \hat{c}_b \hat{c}_c \tag{2.15}$$
$$+\frac{1}{16}L^4 \int_{\mathcal{S}^1} k_\tau \left(1 - D_\tau\right) \left(\left(\delta_{ia}\hat{c}_j\hat{c}_b + \delta_{ib}\hat{c}_j\hat{c}_a + \delta_{ja}\hat{c}_i\hat{c}_b + \delta_{jb}\hat{c}_i\hat{c}_a\right)\hat{c}_h\hat{c}_c - 4\hat{c}_i\hat{c}_j\hat{c}_h\hat{c}_a\hat{c}_b\hat{c}_c\right)$$
$$\mathbb{P}_{ij} = -L \int_{\mathcal{S}^1} k_\eta \left(1 - D_\eta\right) u_\eta^{pl} \hat{c}_i \hat{c}_j \tag{2.16}$$
$$\mathbb{Q}_{ijh} = -\frac{1}{4}L^2 \int_{\mathcal{S}^1} k_\eta \left(1 - D_\eta\right) u_\eta^{pl} \hat{c}_i \hat{c}_j \hat{c}_h \tag{2.17}$$

According to the legacy of strain gradient continua [11, 19], a consequence of the expression (2.12) for the elastic energy per unit area is the form of both the stress tensor S and the hyper stress tensor T, i.e.,

$$S_{ij} = \frac{\partial U}{\partial G_{ij}} = \mathbb{P}_{ij} + \mathbb{C}_{ijab}G_{ab} + \mathbb{M}_{ijabc}G_{ab,c}, \qquad T_{ijh} = \frac{\partial U}{\partial G_{ij,h}} = \mathbb{Q}_{ijh} + \mathbb{D}_{ijhabc}G_{ab,c} + \mathbb{M}_{ijhab}G_{ab}, \tag{2.18}$$

where $\mathbb{P}$ and $\mathbb{Q}$ take the roles of the pre-stress and the pre-hyper stress, respectively. We oversee that (i) the normal plastic displacement u_η^{pl} has a direct influence, as expected, from (2.16)–(2.17) on the pre-stress and on the pre-hyper stress and (ii) damage variables D_η and D_τ has a direct influence from (2.13)–(2.17) on all the stiffness tensors.

2.2. The dissipation energy per unit area

Damage and plastic variables are dissipative in nature and their evolution are related to the form of the dissipation energy. The dissipation energy per unit area W is the energy dissipated because of irreversible phenomena. An additive decomposition of the dissipation energy is assumed in terms of $W_D = W_D^\eta + W_D^\tau$, the energy dissipated because of damage phenomena (where W_D^η is the part that is due to the normal phenomena and W_D^τ is the part that is due to tangential phenomena), and W_{pl}, the energy dissipated because of plasticity phenomena, i.e.,

$$W = W_D + W_{pl} = W_D^\eta + W_D^\tau + W_{pl}, \tag{2.19}$$
$$W_D^\eta = \int_{\mathcal{S}^1} \frac{1}{2}k_\eta^c \left(B_\eta^c\right)^2 \Theta\left(-u_\eta^{el}\right)\left[-D_\eta + \frac{2}{\pi}\tan\left(\frac{\pi}{2}D_\eta\right)\right] \tag{2.20}$$
$$+ \int_{\mathcal{S}^1} \frac{1}{2}k_\eta^t \left(B_\eta^t\right)^2 \Theta\left(u_\eta^{el}\right)\left[2 + \left(D_\eta - 1\right)\left(2 - 2\log\left(1 - D_\eta\right) + \left(\log\left(1 - D_\eta\right)\right)^2\right)\right],$$
$$W_D^\tau = \int_{\mathcal{S}^1} \frac{1}{2}k_\tau \left[\widetilde{B}_\tau\left(u_\eta^{el}\right)\right]^2 \left[2 + \left(D_\tau - 1\right)\left(2 - 2\log\left(1 - D_\tau\right) + \left(\log\left(1 - D_\tau\right)\right)^2\right)\right], \tag{2.21}$$
$$W_{pl} = \int_{\mathcal{S}^1} \sigma_\eta^t \lambda_\eta^t + \sigma_\eta^c \lambda_\eta^c, \tag{2.22}$$

where B_η^c and B_η^t are two characteristic displacements associated with normal damage dissipation in compression and in tension, respectively. The complicated forms of the assumed dissipated energy

in (2.20)–(2.21) are devoted to obtain, in the subsection 2.5, an exponential and/or an arctangential damage evolution, as it will be proved in (2.42) and (2.43).

For cementitious materials it is intuitive that $B_\eta^t \ll B_\eta^c$. The reason is that, in tension, a smaller amount of elastic normal displacement is needed to activate damage mechanisms. Besides, $\widetilde{B}_\tau\left(u_\eta^{el}\right)$ is the characteristic displacement associated with tangent damage dissipation. It is assumed to depend on u_η^{el}, i.e., on the elastic part of the normal displacement as follows,

$$B_\tau = \widetilde{B}_\tau\left(u_\eta^{el}\right) = \begin{cases} B_{\tau 0} & \text{if } u_\eta^{el} \geq 0 \\ B_{\tau 0} - \alpha_2 u_\eta^{el} & \text{if } \frac{1-\alpha_1}{\alpha_2} B_{\tau 0} \leq u_\eta^{el} < 0 \\ \alpha_1 B_{\tau 0} & \text{if } u_\eta^{el} < B_{\tau 0}\frac{1-\alpha_1}{\alpha_2}, \end{cases} \tag{2.23}$$

where $B_{\tau 0}$, α_1 and α_2 are necessary constitutive parameters needed to express the function $\widetilde{B}_\tau\left(u_\eta^{el}\right)$. These parameters have the role to couple the two terms, namely the addends (2.20) and (2.21), of the damage dissipation energy W_D per unit area. It is worth to be noted that usually, for cementitious materials and in elastic tension, the characteristic tangential displacement $B_\tau = B_{\tau 0}$ is much lower than the one $B_\tau = \alpha_1 B_{\tau 0}$ it is necessary in elastic compression ($\alpha_1 \gg 1$). Indeed, a smaller amount of elastic tangential displacement is needed in elastic extension to activate tangential damage mechanisms with respect to the tangential displacement that is needed in elastic compression. In other words, referring to Eq (2.23), this means both that $B_{\tau 0} < B_{\tau 0} - \alpha_2 u_\eta^{el}$ (which implies $\alpha_2 > 0$, as $u_\eta^{el} < 0$ in compression) and $B_{\tau 0} << \alpha_1 B_{\tau 0}$ (which implies $\alpha_1 \gg 1$).

The plastic dissipation energy function per unit area W_{pl} in (2.22) is assumed to linearly depend on the plastic multipliers λ_η^t and λ_η^c that are the plastic accumulated displacement in tension and in compression, respectively. The plastic normal displacement is defined as the following difference,

$$u_\eta^{pl} = \lambda_\eta^t - \lambda_\eta^c. \tag{2.24}$$

We will show at the end of Subsection 2.5 that the scalars σ_η^t and σ_η^c, defined in (2.22), dictate the yielding conditions (more specifically, they are the characteristic force that is necessary to apply to the grain-pair to activate plastic deformation for no-damage case) of the damage-elasto-plastic grain-pair interaction in tension and compression, respectively. It is worth to be noted that the identification of newly introduced constitutive parameters, i.e. of L, B_η^t, B_η^c, $B_{\tau 0}$, α_1 and α_2, is necessary for the application of the present approach for modeling the mechanical behavior or real materials such as, e.g., concrete.

2.3. The energy functional

The energy functional is defined as the sum of the elastic and dissipation energy,

$$\mathcal{E}\left(\chi, D_\eta, D_\tau, \lambda_\eta^t, \lambda_\eta^c\right) = \int_{\mathcal{B}} U + W, \tag{2.25}$$

integrated over the $2D$ reference configuration $\mathcal{B}$. It is a functional of the fundamental kinematical descriptors of the model, i.e. the placement

$$\chi\left(\boldsymbol{X}, t\right), \tag{2.26}$$

that is a function of position $\boldsymbol{X}$ and time t, and the 4 irreversible descriptors

$$D_\eta\left(\boldsymbol{X},\hat{c},t\right), D_\tau\left(\boldsymbol{X},\hat{c},t\right), \lambda_\eta^t\left(\boldsymbol{X},\hat{c},t\right), \lambda_\eta^c\left(\boldsymbol{X},\hat{c},t\right), \tag{2.27}$$

that are functions not only of position X and time t but also on the orientation $\hat{c}$.

Damage (D_η and D_τ) and plastic (λ_η^t and λ_η^c) variables are defined both by two variables that are non-decreasing in time. These inequality assumptions,

$$\frac{\partial D_\eta}{\partial t} \geq 0, \quad \frac{\partial D_\tau}{\partial t} \geq 0, \quad \frac{\partial \lambda_\eta^t}{\partial t} \geq 0, \quad \frac{\partial \lambda_\eta^c}{\partial t} \geq 0, \quad \forall \boldsymbol{X} \in \mathcal{B}, \quad \forall \hat{c} \in \mathcal{S}^1, \tag{2.28}$$

imply a generalization of standard variational principle into a so-called hemivariational principle.

2.4. The hemivariational inequality principle

Let us introduce a monotonously increasing time sequence $T_i \in \{T_i\}_{i=0,\dots,M}$ with $T_i \in \mathbb{R}$ and $M \in \mathbb{N}$ and give initial datum on each of the fundamental kinematic quantities for $i = 0$, i.e., for time T_0. A family of placements χ defines the motion for each time $t = T_0, T_1, \dots, T_M$. The set AM_t of kinematically admissible placements is defined for a given time t and the set AV_t is defined as the corresponding space of kinematically admissible variations, i.e., $\upsilon = \delta\chi \in AV_t$. Admissible variations β of the irreversible kinematic quantities $\left(D_\eta, D_\tau, \lambda_\eta^t, \lambda_\eta^c\right)$ must be positive, namely

$$\beta = \delta D_\eta, \delta D_\tau, \delta\lambda_\eta^t, \delta\lambda_\eta^c \in \mathbb{R}^+ \times \mathbb{R}^+ \times \mathbb{R}^+ \times \mathbb{R}^+. \tag{2.29}$$

By definition, the first variation $\delta\mathcal{E}$ of the energy functional (2.25) is calculated as

$$\delta\mathcal{E} = \mathcal{E}\left(\chi + \delta\chi, D_\eta + \delta D_\eta, D_\tau + \delta D_\tau, \lambda_\eta^t + \delta\lambda_\eta^t, \lambda_\eta^c + \delta\lambda_\eta^c\right) - \mathcal{E}\left(\chi, D_\eta, D_\tau, \lambda_\eta^t, \lambda_\eta^c\right). \tag{2.30}$$

Besides, the increment of (2.26-2.27), i.e. of the fundamental kinematic quantities, at $t = T_i$ is given by the difference between these quantities as evaluated at times $t = T_i$ and $t = T_{i-1}$, namely

$$\left(\Delta\chi, \Delta D_\eta, \Delta D_\tau, \Delta\lambda_\eta^t, \Delta\lambda_\eta^c\right)_{T_i} = \left(\chi, D_\eta, D_\tau, \lambda_\eta^t, \lambda_\eta^c\right)_{T_i} - \left(\chi, D_\eta, D_\tau, \lambda_\eta^t, \lambda_\eta^c\right)_{T_{i-1}}. \tag{2.31}$$

The same definition is utilized for the increment $\Delta\mathcal{E}$ of the energy functional

$$\Delta\mathcal{E} = \mathcal{E}\left(\chi + \Delta\chi, D_\eta + \Delta D_\eta, D_\tau + \Delta D_\tau, \lambda_\eta^t + \Delta\lambda_\eta^t, \lambda_\eta^c + \Delta\lambda_\eta^c\right) - \mathcal{E}\left(\chi, D_\eta, D_\tau, \lambda_\eta^t, \lambda_\eta^c\right). \tag{2.32}$$

Finally, as a matter of facts, the hemi-variational principle is formulated as follows

$$\Delta\mathcal{E} \leq \delta\mathcal{E} \qquad \forall \upsilon = \delta\chi \in AV_t, \qquad \forall \beta = \left(\delta D_\eta, \delta D_\tau, \delta\lambda_\eta^t, \delta\lambda_\eta^c\right) \in \mathbb{R}^+ \times \mathbb{R}^+ \times \mathbb{R}^+ \times \mathbb{R}^+. \tag{2.33}$$

It is worth to be noted here that introducing the three vectors

$$A = \left(\frac{\partial\mathcal{E}}{\partial\chi}, \frac{\partial\mathcal{E}}{\partial D_\eta}, \frac{\partial\mathcal{E}}{\partial D_\tau}, \frac{\partial\mathcal{E}}{\partial\lambda_\eta^t}, \frac{\partial\mathcal{E}}{\partial\lambda_\eta^c}\right), \quad B = \left(\Delta\chi, \Delta D_\eta, \Delta D_\tau, \Delta\lambda_\eta^t, \Delta\lambda_\eta^c\right), \quad C = (\upsilon, \beta), \tag{2.34}$$

where A is intended as the Frechet derivative of the energy functional, the first variation $\delta\mathcal{E}$ of the energy functional in (2.30) and its increment $\Delta\mathcal{E}$ in (2.32) are represented as linear functional of the variation C and the increment B as follows,

$$\delta\mathcal{E} = A \cdot C, \qquad \Delta\mathcal{E} = A \cdot B, \tag{2.35}$$

so that the hemi-variational principle (2.33) can be formulated

$$A \cdot B \leq A \cdot (\upsilon, \beta) \qquad \forall \upsilon \in AV_t, \qquad \forall \beta \in \mathbb{R}^+ \times \mathbb{R}^+ \times \mathbb{R}^+ \times \mathbb{R}^+. \tag{2.36}$$

As remarked in [36], the inequality (2.33) states that the actual energy release rate is not smaller than any possible one. Thus, it constitutes a kind of principle of maximum energy release rate.

2.5. The consequence of the hemivariational principle

First of all, the reversibility of the admissible placement variation $\upsilon = \delta\chi \in AV_t$ implies

$$\mathcal{E}\left(\chi + \delta\chi, D_\eta, D_\tau, \lambda_\eta^t, \lambda_\eta^c\right) - \mathcal{E}\left(\chi, D_\eta, D_\tau, \lambda_\eta^t, \lambda_\eta^c\right) = \frac{\partial \mathcal{E}}{\partial \chi}\delta\chi = 0, \qquad \forall \upsilon = \delta\chi \in AV_t, \tag{2.37}$$

that correspond to standard strain gradient elasticity equations for fixed values of irreversible kinematic quantities $\left(D_\eta, D_\tau, \lambda_\eta^t, \lambda_\eta^c\right)$. Equation (2.37) is derived simply evaluating the inequality (2.36) both for $\delta\chi = \Delta\chi + \hat{\delta}\chi$ and $\beta = \left(\Delta D_\eta, \Delta D_\tau, \Delta\lambda_\eta^t, \Delta\lambda_\eta^c\right)$ and for $\delta\chi = \Delta\chi - \hat{\delta}\chi$ and $\beta = \left(\Delta D_\eta, \Delta D_\tau, \Delta\lambda_\eta^t, \Delta\lambda_\eta^c\right)$, where $\hat{\delta}\chi$ is another arbitrary variation that in (2.37) takes the same symbol $\delta\chi$ just for the sake of simplicity. Secondly, following [47], the variational inequality (2.36) implies the following KKT conditions on the 4 irreversible kinematic descriptors $\left(D_\eta, D_\tau, \lambda_\eta^t, \lambda_\eta^c\right)$

$$\left\{D_\eta - \tilde{D}_\eta(u_\eta, \lambda_\eta^t, \lambda_\eta^c)\right\}\Delta D_\eta = 0 \tag{2.38}$$

$$\left\{D_\tau - \tilde{D}_\tau(u_\tau)\right\}\Delta D_\tau = 0 \tag{2.39}$$

$$\left\{\lambda_\eta^t - \tilde{\lambda}_\eta^t(u_\eta, \lambda_\eta^c, D_\eta, D_\tau)\right\}\Delta\lambda_\eta^t = 0 \tag{2.40}$$

$$\left\{\lambda_\eta^c - \tilde{\lambda}_\eta^c(u_\eta, \lambda_\eta^t, D_\eta, D_\tau)\right\}\Delta\lambda_\eta^c = 0, \tag{2.41}$$

where the derivation of (2.38) is done simply evaluating the inequality (2.36) both for $\delta\chi = \Delta\chi$ and $\beta = \left(2\Delta D_\eta, \Delta D_\tau, \Delta\lambda_\eta^t, \Delta\lambda_\eta^c\right)$ and for $\delta\chi = \Delta\chi$ and $\beta = \left(0, \Delta D_\tau, \Delta\lambda_\eta^t, \Delta\lambda_\eta^c\right)$, the derivation of (2.39) is done simply evaluating the inequality (2.36) both for $\delta\chi = \Delta\chi$ and $\beta = \left(\Delta D_\eta, 2\Delta D_\tau, \Delta\lambda_\eta^t, \Delta\lambda_\eta^c\right)$ and for $\delta\chi = \Delta\chi$ and $\beta = \left(\Delta D_\eta, 0, \Delta\lambda_\eta^t, \Delta\lambda_\eta^c\right)$, the derivation of (2.40) is done simply evaluating the inequality (2.36) both for $\delta\chi = \Delta\chi$ and $\beta = \left(\Delta D_\eta, \Delta D_\tau, 2\Delta\lambda_\eta^t, \Delta\lambda_\eta^c\right)$ and for $\delta\chi = \Delta\chi$ and $\beta = \left(\Delta D_\eta, \Delta D_\tau, 0, \Delta\lambda_\eta^c\right)$ and the derivation of (2.41) is done simply evaluating the inequality (2.36) both for $\delta\chi = \Delta\chi$ and $\beta = \left(\Delta D_\eta, \Delta D_\tau, \Delta\lambda_\eta^t, 2\Delta\lambda_\eta^c\right)$ and for $\delta\chi = \Delta\chi$ and $\beta = \left(\Delta D_\eta, \Delta D_\tau, \Delta\lambda_\eta^t, 0\right)$. In (2.38)–(2.41) the auxiliary threshold functions $\tilde{D}_\eta(u_\eta, \lambda_\eta^t, \lambda_\eta^c)$, $\tilde{D}_\tau(u_\tau)$, $\tilde{\lambda}_\eta^t(u_\eta, \lambda_\eta^c, D_\eta, D_\tau)$ and $\tilde{\lambda}_\eta^c(u_\eta, \lambda_\eta^t, D_\eta, D_\tau)$ have been defined as follows,

$$\tilde{D}_\eta(u_\eta, \lambda_\eta^t, \lambda_\eta^c) = \begin{cases} 1 - \exp\left(-\frac{u_\eta - \lambda_\eta^t + \lambda_\eta^c}{B_\eta^t}\right), & u_\eta^{el} = u_\eta - \lambda_\eta^t + \lambda_\eta^c > 0, \\ \frac{2}{\pi}\arctan\left(-\frac{u_\eta - \lambda_\eta^t + \lambda_\eta^c}{B_\eta^c}\right), & u_\eta^{el} = u_\eta - \lambda_\eta^t + \lambda_\eta^c < 0, \end{cases} \tag{2.42}$$

$$\tilde{D}_\tau(u_\tau) = 1 - \exp\left(-\frac{|u_\tau|}{B_\tau}\right), \tag{2.43}$$

$$\tilde{\lambda}_\eta^t(u_\eta, \lambda_\eta^c, D_\eta, D_\tau) = \lambda_\eta^c - \frac{\sigma_\eta^t}{k_\eta\left(1 - D_\eta\right)} + u_\eta + \frac{k_\tau B_\tau}{k_\eta\left(1 - D_\eta\right)}\frac{\partial \widetilde{B}_\tau}{\partial u_\eta^{el}}\left[\int_0^{D_\tau}\left[\log\left(1 - x\right)\right]^2 dx\right], \tag{2.44}$$

$$\tilde{\lambda}^c_\eta(u_\eta, \lambda^t_\eta, D_\eta, D_\tau) = \lambda^t_\eta - \frac{\sigma^c_\eta}{k_\eta\left(1-D_\eta\right)} - u_\eta - \frac{k_\tau B_\tau}{k_\eta\left(1-D_\eta\right)}\frac{\partial\widetilde{B}_\tau}{\partial u^{el}_\eta}\left[\int_0^{D_\tau}\left[\log\left(1-x\right)\right]^2 dx\right]. \quad (2.45)$$

From Eqs (2.42) and (2.43) the meaning of B^t_η, B^c_η and B_τ as characteristic displacements for the activation of the damage phenomena is evident at least for the loading case. Besides, we observe from (2.44) and (2.45) that with no damage, the meaning of the scalars σ^t_η and σ^c_η as those characteristic forces that dictate the yielding conditions in tension and compression, is also explained. However, the presence of the normal damage D_η makes higher such effective characteristic displacement that, in the failure case (with $D_\eta \to 1$), becomes infinite.

3. Implementation of the model

In this Section, the implementation of the model previously presented is divided in the following 5 steps.

1) Null initial, i.e., at time $t = 0$, conditions is assumed on the displacement field for all the points of the body

$$u\left(\boldsymbol{X}, t=0\right) = \boldsymbol{\chi}\left(\boldsymbol{X}, t=0\right) - \boldsymbol{X} = 0, \quad \forall \boldsymbol{X} \in \mathcal{B} \quad (3.1)$$

and and the same for damage and plastic irreversible descriptors both for all the points of the body and for all the directions,

$$\begin{cases} D_\eta = \breve{D}_\eta\left(\hat{c}, \boldsymbol{X}, t=0\right) = 0, & D_\tau = \breve{D}_\tau\left(\hat{c}, \boldsymbol{X}, t=0\right) = 0 \\ \lambda^t_\eta = \breve{\lambda}^t_\eta\left(\hat{c}, \boldsymbol{X}, t=0\right) = 0, & \lambda^c_\eta = \breve{\lambda}^c_\eta\left(\hat{c}, \boldsymbol{X}, t=0\right) = 0 \end{cases}, \qquad \forall \hat{c} \in \mathcal{S}^1 \quad \forall \boldsymbol{X} \in \mathcal{B} \quad (3.2)$$

2) Initial isotropy is assumed, that means that non-damaged stiffnesses k^c_η, k^t_η and k_τ are assumed to be initially constant $\forall \hat{c} \in \mathcal{S}^1$ and $\forall \boldsymbol{X} \in \mathcal{B}$

$$k^c_\eta = \tilde{k}^c_\eta\left(\hat{c}, \boldsymbol{X}, t=0\right) = \frac{\bar{k}^c_\eta}{2\pi}, \quad k^t_\eta = \tilde{k}^t_\eta\left(\hat{c}, \boldsymbol{X}, t=0\right) = \frac{\bar{k}^t_\eta}{2\pi}, \quad k_\tau = \tilde{k}_\tau\left(\hat{c}, \boldsymbol{X}, t=0\right) = \frac{\bar{k}_\tau}{2\pi}, \quad (3.3)$$

where $\bar{k}^c_\eta$, $\bar{k}^t_\eta$ and $\bar{k}_\tau$ are the averaged non-damaged initial stiffnesses.

3) Numerical values of the parameters of the model are assumed and here are reported in Tables 1 and 2.

4) The elastic stiffness tensors ($\mathbb{C}, \mathbb{M}, \mathbb{D}$), as well as the pre-stress and pre hyperstress tensors ($\mathbb{P}, \mathbb{Q}$) are calculated according to Eqs (2.13)–(2.17) at time $t = 0$ with the initial input (3.1)–(3.3). These ingredients with proper boundary conditions are the input for a standard variational principle in (2.37), where the dissipation energy becomes simply an additive constant that does not influence the minimization process. Such a minimization can be performed analytically (as in the homogeneous cases of Section 4) or, more generally, with the use of a Finite Element Method (FEM). Thus, we obtain the displacement field at $i = 1$,

$$u\left(\boldsymbol{X}, t = T_i\right), \quad \forall \boldsymbol{X} \in \mathcal{B}. \quad (3.4)$$

5) With (3.4) we compute the new irreversible descriptors $\left(D_\eta, D_\tau, \lambda_\eta^t, \lambda_\eta^c\right)$ via the KKT conditions (2.38)–(2.41) at $i = 1$,

$$\begin{cases} D_\eta = \breve{D}_\eta\left(\hat{c}, \boldsymbol{X}, t = T_i\right), & D_\tau = \breve{D}_\tau\left(\hat{c}, \boldsymbol{X}, t = T_i\right) \\ \lambda_\eta^t = \breve{\lambda}_\eta^t\left(\hat{c}, \boldsymbol{X}, t = T_i\right), & \lambda_\eta^c = \breve{\lambda}_\eta^c\left(\hat{c}, \boldsymbol{X}, t = T_i\right) \end{cases}, \qquad \forall \hat{c} \in \mathcal{S}^1 \quad \forall \boldsymbol{X} \in \mathcal{B} \tag{3.5}$$

Thus, we iterate the points 4 and 5 for all those time sequence $T_i \in \{T_i\}_{i=0,\dots,M}$ with $T_i \in \mathbb{R}$ and $M \in \mathbb{N}$ of the researched time history defined at the beginning of Subsection 2.4.

Table 1. Constitutive parameters values employed for homogeneous extension/compression tests.

L[m]	A[m]	$\bar{k}_\eta^c[\frac{Kg}{s^2m^2}]$	$\bar{k}_\eta^t[\frac{Kg}{s^2m^2}]$	$\bar{k}_\tau[\frac{Kg}{s^2m^2}]$	B_η^t[m]	B_η^c[m]
0.01	0.1	$2\pi\, 14\, 10^{14}$	$10\bar{k}_\eta^c$	$2\pi\, 10^{13}$	10^{-8}	10^{-7}
$B_{\tau 0}$[m]	α_1[1]	α_2[1]	$\sigma_\eta^t[J/m^3]$	$\sigma_\eta^c[J/m^3]$	.	.
$5 \cdot 10^{-8}$	10	14	$8.385 \cdot 10^6$	$8.912 \cdot 10^7$	.	.

Table 2. Parameters for external boundary conditions employed for the investigated homogeneous tests.

α_c	α_t
$2\ 10^{-6} m/s$	$10^{-7} m/s$

4. Homogeneous response

Constitutive parameters are depicted in Table 1. Thus, from [12, 59] we have an equivalent initial Young modulus in compression E_c or in tension E_t and Poisson ratio in compression ν_c or in tension ν_t, that yields in compression

$$E_c = L^2 k_\eta^c \frac{k_\eta^c + 4k_\tau}{3k_\eta^c + 4k_\tau} = 299GPa, \quad \nu_c = \frac{k_\eta^c - 4k_\tau}{3k_\eta^c + 4k_\tau} = 0.32 \tag{4.1}$$

or in tension

$$E_t = L^2 k_\eta^t \frac{k_\eta^t + 4k_\tau}{3k_\eta^t + 4k_\tau} = 34.4GPa, \quad \nu_c = \frac{k_\eta^t - 4k_\tau}{3k_\eta^t + 4k_\tau} = 0.22. \tag{4.2}$$

Let us solve the problem in Figure 1. The imposed displacement is

$$\delta(t) = \alpha t \tag{4.3}$$

and, consequently, the displacement is trivially deduced in all the body,

$$u_1 = \frac{\alpha}{A} t X_1, \quad u_2 = 0, \qquad \forall X \in \mathcal{B}. \tag{4.4}$$

Thus, the strain and strain gradient are

$$G_{11} = \frac{\alpha}{A}t + \frac{1}{2}\left(\frac{\alpha}{A}t\right)^2, \quad G_{12} = G_{22} = 0, \quad \nabla G = 0, \tag{4.5}$$

and the relative displacements from (2.3) and (2.4) are

$$u_\eta = LG_{11}\cos\theta = L\left[\frac{\alpha}{A}t + \frac{1}{2}\left(\frac{\alpha}{A}t\right)^2\right]\cos\theta, \tag{4.6}$$

$$u_\tau^2 = 4L^2G_{11}G_{11}\left(\cos^4\theta - \cos^2\theta\right) = \left(L\left[\frac{\alpha}{A}t + \frac{1}{2}\left(\frac{\alpha}{A}t\right)^2\right]\sin 2\theta\right)^2, \tag{4.7}$$

where a standard parameterization of the unit vector $\hat{c}$ has been used in terms of an angle θ, i.e.,

$$\hat{c}_1 = \cos\theta, \quad \hat{c}_2 = \sin\theta. \tag{4.8}$$

The stress response is given in terms of the components of the stress tensors in (2.18),

$$S_{11} = \mathbb{P}_{11} + \mathbb{C}_{1111}G_{11}, \tag{4.9}$$

$$S_{22} = \mathbb{P}_{22} + \mathbb{C}_{2211}G_{11}, \tag{4.10}$$

$$S_{12} = \mathbb{P}_{12} + \mathbb{C}_{1211}G_{11}, \tag{4.11}$$

$$T = 0 \tag{4.12}$$

that implies

$$\begin{aligned} S_{11} &= -L\int_0^{2\pi}\left[k_\eta\left(1-D_\eta\right)\left(\lambda_\eta^t - \lambda_\eta^c\right)\cos^2\theta\right]d\theta \\ &+ G_{11}L^2\int_0^{2\pi}\left[k_\eta\left(1-D_\eta\right)\cos^4\theta + k_\tau\left(1-D_\tau\right)\left(4\cos^2\theta - 4\cos^4\theta\right)\right]d\theta, \end{aligned} \tag{4.13}$$

$$\begin{aligned} S_{22} &= -L\int_0^{2\pi}\left[k_\eta\left(1-D_\eta\right)\left(\lambda_\eta^t - \lambda_\eta^c\right)\sin^2\theta\right]d\theta \\ &+ G_{11}L^2\int_0^{2\pi}\left[k_\eta\left(1-D_\eta\right)\sin^2\theta\cos^2\theta - 4k_\tau\left(1-D_\tau\right)\cos^4\theta\right]d\theta, \end{aligned} \tag{4.14}$$

$$S_{12} = 0, \qquad T = 0. \tag{4.15}$$

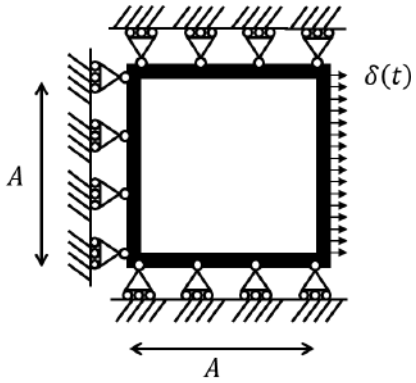

Figure 1. Schematic structure for the response to imposed displacement for tension ($\delta(t) > 0$) or compression ($\delta(t) < 0$) tests.

4.1. Strain tension control

In tension

$$\alpha = \alpha_t > 0 \tag{4.16}$$

the normal displacement $u_\eta \geq 0$ is positive in any direction (i.e., $\forall\theta \in [0, 2\pi]$) and therefore from (2.45) we have

$$\lambda_\eta^c = 0. \tag{4.17}$$

From (2.42) and (2.44) we have

$$\tilde{D}_\eta(u_\eta, \lambda_\eta^t, \lambda_\eta^c) = 1 - \exp\left(-\frac{u_\eta - \lambda_\eta^t}{B_\eta^t}\right), \quad \tilde{\lambda}_\eta^t(u_\eta, \lambda_\eta^c, D_\eta, D_\tau) = u_\eta - \frac{\sigma_\eta^t}{k_\eta\left(1 - D_\eta\right)}. \tag{4.18}$$

At the beginning of the time history (i.e., with $0 < u_\eta \ll L$ from (4.6)) we have from $(4.18)_2$ that $\tilde{\lambda}_\eta^t(u_\eta, \lambda_\eta^c, D_\eta, D_\tau) < 0$ that means an analytical solution for the accumulation in tension and for the normal damage,

$$\lambda_\eta^t = 0, \quad D_\eta = 1 - \exp\left(-\frac{u_\eta}{B_\eta^t}\right). \tag{4.19}$$

The solution (4.19) is valid only before the threshold condition (2.40) with (2.44)

$$\tilde{\lambda}_\eta^t(u_\eta, \lambda_\eta^c, D_\eta, D_\tau) = u_\eta - \frac{\sigma_\eta^t}{k_\eta\left(1 - D_\eta\right)} = 0 \tag{4.20}$$

is satisfied. Thus, by insertion of $(4.19)_2$ into (4.20) we have,

$$\left(1 - D_\eta\right) = \frac{\sigma_\eta^t}{k_\eta u_\eta} = \exp\left(-\frac{u_\eta}{B_\eta^t}\right). \tag{4.21}$$

The nonlinear algebraic equation (4.21) defines a Lambert function, does not have an analytical solution and can be solved only numerically or graphically, e.g., in Figure 2, from which it is clear, with the constitutive parameters that we have chosen in Table 1, that the condition (4.21) is satisfied for no values of the normal displacement u_η, that implies that $(4.19)_1$ is always valid in this investigated case and no plastic behavior takes place. Besides, a different choice of the normal damage characteristic displacement B_η^t would give a different result. From Figure 2 it is in fact also shown that by assigning a value of the normal damage characteristic displacement B_η^t equal to 20 times that assigned in Table 1, there exist a value for the normal displacement $u_\eta = \breve{u}_\eta$ that satisfies (4.21),

$$\frac{\sigma_\eta^t}{k_\eta u_\eta} = \exp\left(-\frac{u_\eta}{B_\eta^t}\right), \quad \Rightarrow \quad u_\eta = \breve{u}_\eta \tag{4.22}$$

that implies that $(4.19)_1$ is not valid and plasticity takes a role in this new investigated case. The new analytical solution comes from (4.18), from which we derive the nonlinear algebraic equation for normal damage

$$1 - D_\eta = \exp\left(-\frac{\sigma_\eta^t}{B_\eta^t k_\eta\left(1 - D_\eta\right)}\right), \quad \Rightarrow \quad D_\eta = \breve{D}_\eta, \quad u_\eta > \breve{u}_\eta \tag{4.23}$$

and for accumulation of tension

$$\lambda_\eta^t = u_\eta - \frac{\sigma_\eta^t}{k_\eta\left(1-\check{D}_\eta\right)}, \quad u_\eta > \check{u}_\eta \tag{4.24}$$

We observe from (4.23) that the normal damage $D_\eta = \check{D}_\eta$ at which the condition $u_\eta = \check{u}_\eta > 0$ holds is constant with respect to the normal displacement u_η and therefore with respect to time. This implies that the accumulation in tension in (4.24) evolves linearly with the normal displacement.

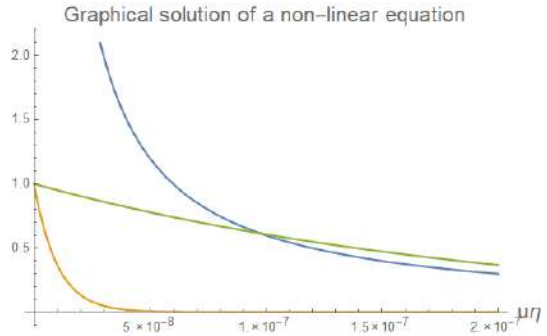

Figure 2. Numerical investigation of (4.21) with parameters assigned in Table 1 and with 20 times the value of normal damage characteristic displacement B_η^t. Blue curve is the left-hand side of (4.21), i.e., $\frac{\sigma_\eta^t}{k_\eta u_\eta}$. Orange line is the right-hand side of (4.21), i.e., $\exp\left(-\frac{u_\eta}{B_\eta^t}\right)$. Blue and orange lines do not intersect and therefore there is no solution $\check{u}$ of (4.22). Green line is the right-hand side of (4.21) with B_η^t being 20 times that represented in Table 1, i.e., $\exp\left(-\frac{u_\eta}{20B_\eta^t}\right)$. Blue and green lines do intersect and therefore there is a solution $\check{u}$ of (4.22) in this case.

The response is calculated by (4.13)–(4.15) and it is graphically represented in Figure 3. We observe (S_{11} in the left-hand side of Figure 3) that, after a first part where we have an increasing function of time, in a second part of the response the softening induced by damage is evident and a peak reaction is observed as well as a descending curve. A positive reaction is observed also in the orthogonal direction (S_{22} in the right-hand side of Figure 3). The behavior in the orthogonal direction is almost equivalent. However, a second hardening stage is observed because of a non trivial evolution of the equivalent (the response is not anymore isotropic) Poisson ratio.

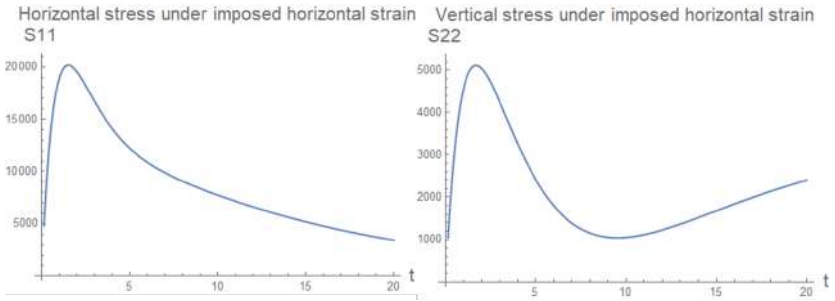

Figure 3. Stress response to imposed axial displacement in tension depicted in Figure 1.

The softening behavior is due the non homogeneous evolution of the damage variables with respect to the grain-pair orientation $\hat{c} \in \mathcal{S}^1$ or, equivalently, to the angle $\theta \in [0, 2\pi]$, as it is shown in Figure 4.

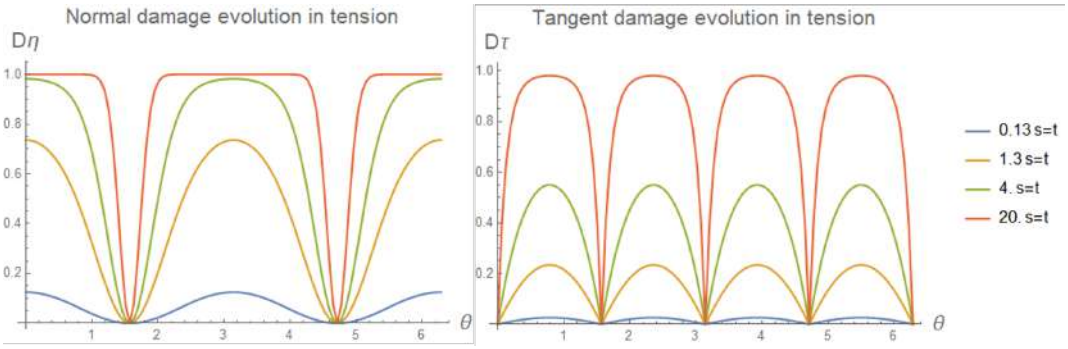

Figure 4. Evolution of normal and tangent damage for the case of axial displacement in tension imposed and depicted in Figure 1.

The anisotropic behavior is also explicated in the evolution of the ratio $\mathbb{C}_{2222}/\mathbb{C}_{1111}$ between the vertical and the horizontal stiffness in Figure 5.

In the left-hand side picture of Figure 4 normal damage evolution is shown and it is evident that the horizontal grain-pair orientation, i.e., around $\theta = k\pi$, with $k \in \mathbb{Z}$, are the most affected by the damage effect. In the right-hand side picture of Figure 4 tangential damage evolution is shown and it is evident that the oblique grain-pair orientation, i.e., around $\theta = \pi/4 + k\pi/2$, with $k \in \mathbb{Z}$, are the most affected by the damage effect. It is also observed that the velocity of the damage evolution is constitutively driven by the damage characteristic displacements B^t_η, B^c_η and B_τ. It is also worth to be noted from Figure 5 that the anisotropy between vertical and horizontal stiffness on the one hand in an elastic isotropic simulation should be maintained at 1 for the entire history of deformation. Here, on the other hand, it goes from 1 at $t = 0$ (i.e., initial isotropic behavior) to 60 at $t = 20s$ (i.e., we have anisotropic behavior induced by deformation).

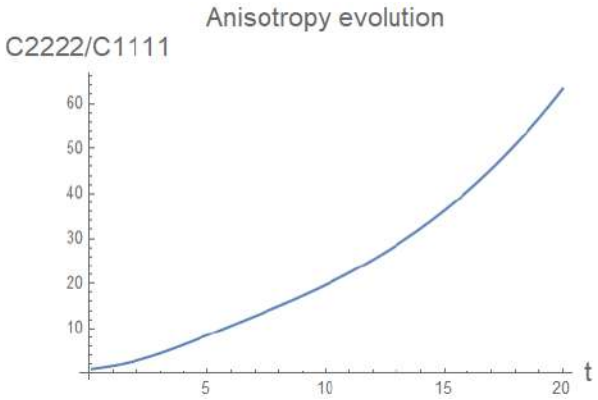

Figure 5. Evolution of the ratio $\mathbb{C}_{2222}/\mathbb{C}_{1111}$, that is the ratio between the vertical and the horizontal stiffness for the case of axial displacement in tension imposed depicted in Figure 1.

As it is shown in Figure 2 on the one hand no plastic behavior occurs in this case. On the other hand, increasing 20 times the normal damage characteristic displacement ($B^t_\eta \to 20B^t_\eta$), the response changes dramatically. In Figure 6 the stress response is shown in this second case and the softening behavior is very much attenuated.

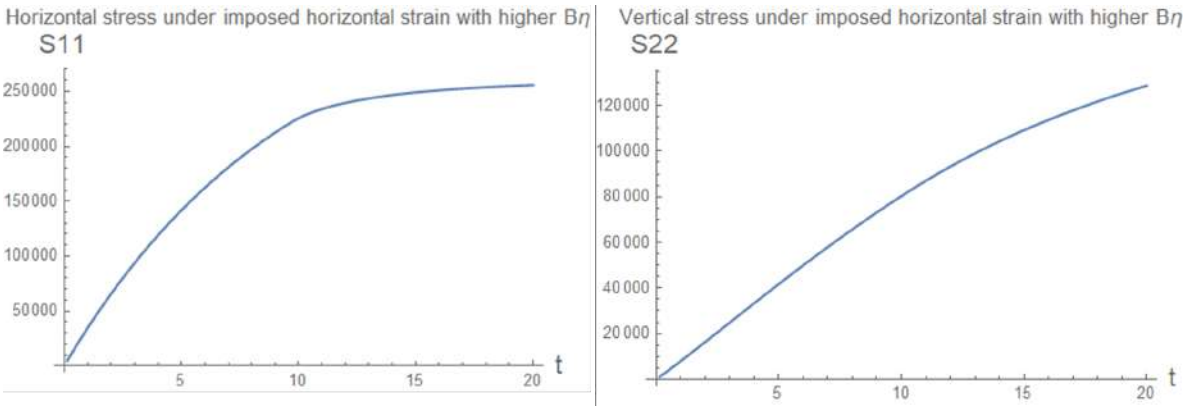

Figure 6. Stress response to imposed axial displacement in tension depicted in Figure 1 and higher normal damage characteristic displacement.

In Figure 7 normal and tangent damage evolution are also different. In fact, e.g., maximum normal damage is not any more equal to the admissible value $D_\eta \simeq 1$ but to the constant value $D_\eta = \check{D}_\eta \simeq 0.4$ that was analytically calculated in (4.23).

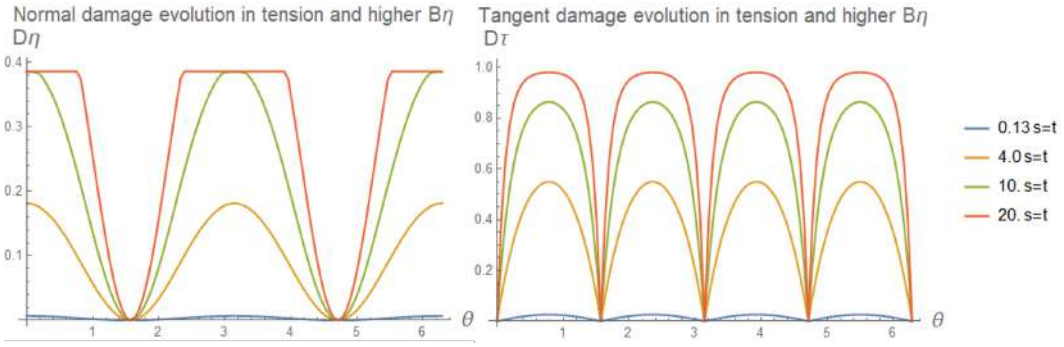

Figure 7. Evolution of normal and tangent damage for the case of axial displacement in tension imposed depicted in Figure 1 and higher normal damage characteristic displacement.

The non trivial plastic displacement evolution $u^{pl}_\eta = \lambda^t_\eta - \lambda^c_\eta$ is therefore shown in Figure 8. It is evident that the plastic displacement occurs only around the horizontal direction.

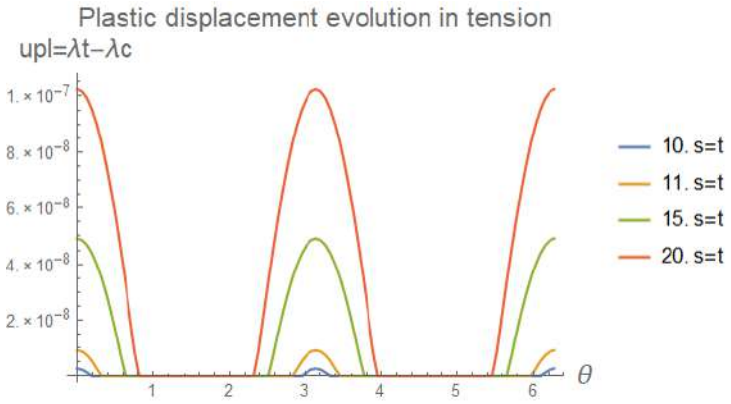

Figure 8. Evolution of plastic displacement $u_\eta^{pl} = \lambda_\eta^t - \lambda_\eta^c$ for the case of axial displacement in tension imposed depicted in Figure 1 and higher normal damage characteristic displacement.

4.2. Strain compression control

In compression

$$\alpha = -\alpha_c < 0. \tag{4.25}$$

the relative displacement $u_\eta \leq 0$ is negative in any direction (i.e., $\forall\theta \in [0, 2\pi]$) and therefore from (2.44) we have

$$\lambda_\eta^t = 0. \tag{4.26}$$

From (2.42) and (2.44) we have

$$\tilde{D}_\eta(u_\eta, \lambda_\eta^t, \lambda_\eta^c) = \frac{2}{\pi}\arctan\left(-\frac{u_\eta + \lambda_\eta^c}{B_\eta^c}\right), \quad \tilde{\lambda}_\eta^c(u_\eta, \lambda_\eta^c, D_\eta, D_\tau) = -u_\eta - \frac{\sigma_\eta^c}{k_\eta\left(1 - D_\eta\right)}. \tag{4.27}$$

At the beginning of the time history (i.e., with $0 \geq u_\eta \gg -L$ from (4.6)) we have from $(4.27)_2$ that $\tilde{\lambda}_\eta^c(u_\eta, \lambda_\eta^c, D_\eta, D_\tau) < 0$ that means an analytical solution for the accumulation in compression and for the normal damage as follows,

$$\lambda_\eta^c = 0, \quad D_\eta = \frac{2}{\pi}\arctan\left(-\frac{u_\eta}{B_\eta^c}\right). \tag{4.28}$$

The solution (4.28) is valid only before the threshold condition (2.41) with (2.45)

$$\tilde{\lambda}_\eta^c(u_\eta, \lambda_\eta^c, D_\eta, D_\tau) = -u_\eta - \frac{\sigma_\eta^c}{k_\eta\left(1 - D_\eta\right)} = 0 \tag{4.29}$$

is satisfied. Thus, by insertion of $(4.28)_2$ into (4.29) we have,

$$\left(1 - D_\eta\right) = \frac{-\sigma_\eta^c}{k_\eta u_\eta} = 1 - \frac{2}{\pi}\arctan\left(-\frac{u_\eta}{B_\eta^c}\right). \tag{4.30}$$

With the constitutive parameters that we have chosen in Table 1 this condition happens at $u_\eta = \bar{u}_\eta < 0$ and therefore we have (4.28) for $u_\eta < \bar{u}_\eta$

$$\lambda_\eta^c = -u_\eta - \frac{\sigma_\eta^c}{k_\eta\left(1 - D_\eta\right)}, \quad D_\eta = \frac{2}{\pi}\arctan\left(-\frac{u_\eta + \lambda_\eta^c}{B_\eta^c}\right). \tag{4.31}$$

By insertion of (4.31) into (4.30) we also obtain a nonlinear algebraic equation

$$D_\eta = \frac{2}{\pi}\arctan\left(\frac{\sigma_\eta^c}{k_\eta B_\eta^c\left(1 - D_\eta\right)}\right), \quad \Rightarrow \quad D_\eta = \bar{D}_\eta \tag{4.32}$$

the solution of which gives the normal damage $D_\eta = \bar{D}_\eta$ at which the condition $u_\eta = \bar{u}_\eta < 0$ holds and that is constant with respect to the normal displacement u_η and therefore with respect to time. This implies that the accumulation in compression evolves linearly with the normal displacement by insertion of (4.32) into $(4.31)_2$,

$$\lambda_\eta^c = -u_\eta - \frac{\sigma_\eta^c}{k_\eta\left(1 - \bar{D}_\eta\right)}, \quad u_\eta < \bar{u}_\eta < 0 \tag{4.33}$$

This response is calculated by (4.13)–(4.15) and it is graphically represented in Figure 9. We observe ($S_{11} < 0$ in the left-hand side of Figure 9) that, after a first part where we have an decreasing function of time, in a second part of the response the softening induced by damage is evident and a peak reaction is observed as well as a slightly increasing curve. A negative reaction is observed also in the orthogonal direction ($S_{22} < 0$ in the right-hand side of Figure 9). The behavior in the orthogonal direction is almost equivalent except for the slightly increasing part again because of a non trivial evolution of the equivalent (the response is not anymore isotropic) Poisson ratio.

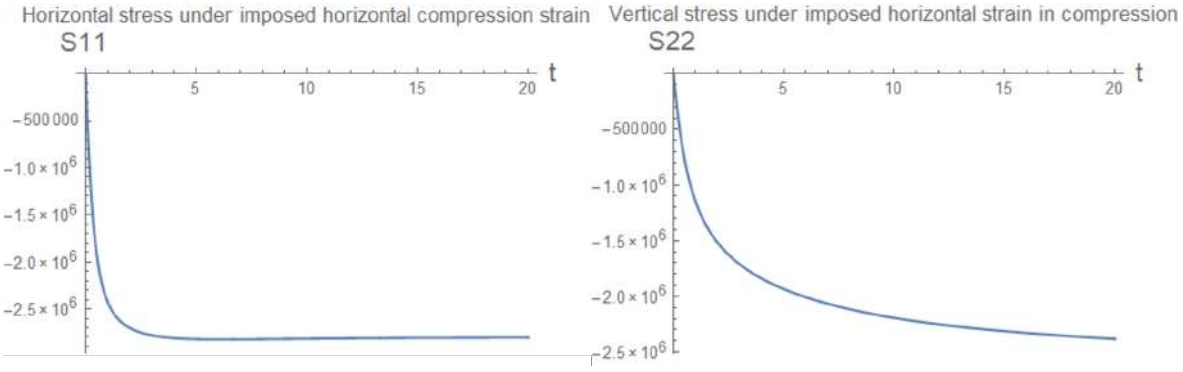

Figure 9. Stress response to imposed axial displacement in compression depicted in Figure 1.

The softening behavior is due the non homogeneous evolution of the damage variables with respect to the grain-pair orientation $\hat{c} \in \mathcal{S}^1$ or, equivalently, to the angle $\theta \in [0, 2\pi]$, as it is shown in Figure 10.

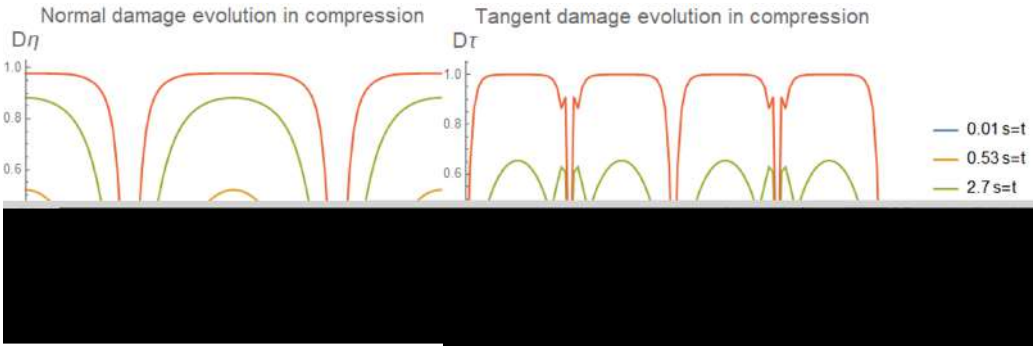

Figure 10. Evolution of normal and tangent damage for the case of axial displacement in compression imposed depicted in Figure 1.

The anisotropic behavior is also explicated in the evolution of the ratio $\mathbb{C}_{2222}/\mathbb{C}_{1111}$ between the vertical and the horizontal stiffness in Figure 11.

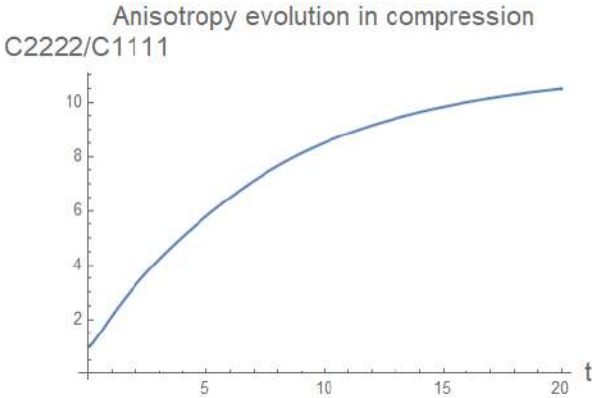

Figure 11. Evolution of the ratio $\mathbb{C}_{2222}/\mathbb{C}_{1111}$, that is the ratio between the vertical and the horizontal stiffness for the case of axial displacement in compression imposed depicted in Figure 1.

In the left-hand side picture of Figure 10 normal damage evolution is shown and it is evident that the horizontal grain-pair orientation, i.e., around $\theta = k\pi$, with $k \in \mathbb{Z}$, are the most affected by the damage effect. In the right-hand side picture of Figure 10 tangential damage evolution is shown and it is evident that the oblique grain-pair orientation, i.e., around $\theta = \pi/4 + k\pi/2$, with $k \in \mathbb{Z}$, are the most affected by the damage effect. This behavior is nevertheless obscured by the non constant dependence of the damage tangential characteristic displacement B_τ with respect to the normal displacement in compression that was made explicit in (2.23). We have that the higher is the compression the lower is the damage velocity evolution. Thus, the orientation that are more in compression, i.e., $\theta = k\pi$, with $k \in \mathbb{Z}$, have lower damage velocity evolution with respect to the orientation that are less in compression, i.e., $\theta = \pi/2 + k\pi$, with $k \in \mathbb{Z}$, where damage have new peaks.

It is also worth to be noted from Figure 11 that the anisotropy between vertical and horizontal stiffness on the one hand in an elastic isotropic simulation should be maintained at 1 for the entire

history of deformation. Here, on the other hand, it goes from 1 at $t = 0$ (i.e., initial isotropic behavior) to 13 at $t = 20s$ (i.e., anisotropic behavior induced by deformation).

The non trivial plastic displacement evolution $u_\eta^{pl} = \lambda_\eta^t - \lambda_\eta^c$ is therefore shown in Figure 12. It is evident that the plastic displacement occurs only around the horizontal direction.

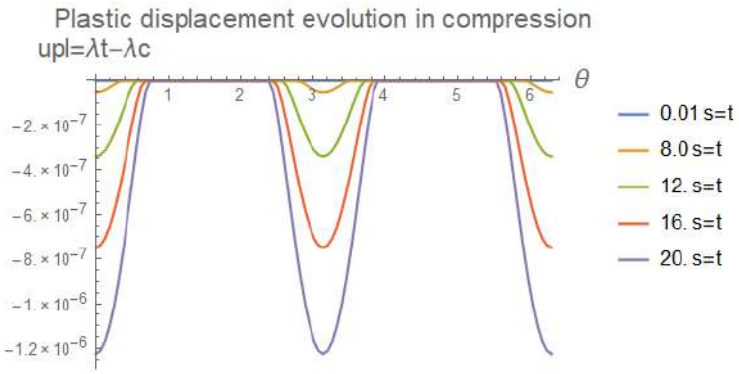

Figure 12. Evolution of plastic displacement for the case of axial displacement in compression imposed depicted in Figure 1 and higher normal damage characteristic displacement.

5. Conclusions

This paper recaps and updates a recently developed continuum model for granular materials in order to handle with those important dissipative phenomena as damage and plasticity. The novelty of such a recap is original. The reason is that here for the first time the dissipation energy and the variational inequality are defined directly integrated over the orientation space. This makes the Euler Lagrange equations related to the displacement field (i.e., the elastic Partial Differential Equations PDEs and Boundary Conditions BCs) already integrated over that space. The advantage is that we derive directly the equations that we use for the numerical integration and we do not need to make an artificial integration after their derivation. Its application to an analytical homogeneous case is considered. Plasticity is given by two separate kinematic descriptors (i.e., the accumulation in tension and the accumulation in compression), that are the two plastic multipliers, for every position, time, and grain pair orientation. A hemi-variational principle was adopted to derive the governing equations, from which we obtain Karush-Kuhn-Tucker (KKT)-kind conditions that specify the progression of damage and plasticity relating to each pair of grains interaction. For the case of homogeneous deformation, an analytical solution for the displacement field is assumed and damage and plastic evolution have been derived. It is worth to remark that for non homogeneous deformation, the computation of non homogeneous strain can be reached, e.g., with a Finite Element method according to the scheme developed in [47, 59], where the presence of strain gradient terms in the PDEs related to the elastic evolution guarantees the overlook of the problem of the mesh-dependence results. Different loading patterns are experienced by different grain-pairs that are oriented in different directions, resulting in complex anisotropic behavior due to damage and plastic evolution. Competition between damage and plasticity dissipative phenomena is demonstrated in these simulations. We show that, for specific parameters, the evolution of plasticity may stop the growth of

damage and vice versa. Besides, the presence of newly conceived constitutive parameters that are present in the dissipation energy functional, imposes a fundamental outlook related to their identification. In the presented model we have the inclusion of simple local plastic interactions that contribute to a complex plastic response of the material as a whole. Finally, no additional assumptions, out of the form of the dissipation energy and such as flow rules, are required to describe the plastic behavior and it is worth to point out that the plastic strain is compatible with the existence of a placement function.

Acknowledgments

This project has received funding from the European Union's Horizon 2020 research and innovation programme under the Marie Skłodowska-Curie grant agreement No 899546.

Conflict of interest

All authors declare no conflicts of interest in this paper

References

1. B. E. Abali, W. H. Müller, F. dell'Isola, Theory and computation of higher gradient elasticity theories based on action principles, *Arch. Appl. Mech.*, **87** (2017), 1495–1510. http://dx.doi.org/10.1007/s00419-017-1266-5
2. E. C. Aifantis, Pattern formation in plasticity, *Int. J. Eng. Sci.*, **33** (1995), 2161–2178. http://dx.doi.org/10.1016/0020-7225(95)00086-D
3. E. C. Aifantis, On the microstructural origin of certain inelastic models, *J. Eng. Mater. Technol.*, **106** (1984), 326–330. http://dx.doi.org/10.1115/1.3225725
4. E. C. Aifantis, The physics of plastic deformation, *Int. J. Plasticity*, **3** (1987), 211–247. http://dx.doi.org/10.1016/0749-6419(87)90021-0
5. J.-J. Alibert, A. Della Corte, I. Giorgio, A. Battista, Extensional Elastica in large deformation as\Gamma-limit of a discrete 1D mechanical system, *Z. Angew. Math. Phys.*, **68** (2017), 42. http://dx.doi.org/10.1007/s00033-017-0785-9
6. J. Altenbach, H. Altenbach, V. A. Eremeyev, On generalized cosserat-type theories of plates and shells: a short review and bibliography, *Arch. Appl. Mech.*, **80** (2010), 73–92. http://dx.doi.org/10.1007/s00419-009-0365-3
7. M. Ambati, T. Gerasimov, L. De Lorenzis, Phase-field modeling of ductile fracture, *Comput. Mech.*, **55** (2015), 1017–1040. http://dx.doi.org/10.1007/s00466-015-1151-4
8. M. Ambati, T. Gerasimov, L. De Lorenzis. A review on phase-field models of brittle fracture and a new fast hybrid formulation, *Comput. Mech.*, **55** (2015), 383–405. http://dx.doi.org/10.1007/s00466-014-1109-y

9. L. Ambrosio, A. Lemenant, G. Royer-Carfagni, A variational model for plastic slip and its regularization via Γ-convergence, *J. Elast.*, **110** (2013), 201–235. http://dx.doi.org/10.1007/s10659-012-9390-5

10. H. Amor, J.-J. Marigo, C. Maurini, Regularized formulation of the variational brittle fracture with unilateral contact: numerical experiments, *J. Mech. Phys. Solids*, **57** (2009), 1209–1229. http://dx.doi.org/10.1016/j.jmps.2009.04.011

11. N. Auffray, F. dell'Isola, V. Eremeyev, A. Madeo, G. Rosi, Analytical continuum mechanics à la Hamilton-Piola least action principle for second gradient continua and capillary fluids, *Math. Mech. Solids*, **20** (2015), 375–417. http://dx.doi.org/10.1177/1081286513497616

12. E. Barchiesi, A. Misra, L. Placidi, E. Turco, Granular micromechanics-based identification of isotropic strain gradient parameters for elastic geometrically nonlinear deformations, *Zeitschrift für Angewandte Mathematik und Mechanik*, **101** (2021), e202100059. http://dx.doi.org/10.1002/zamm.202100059

13. B. Bourdin, G. Francfort, J.-J. Marigo, Numerical experiments in revisited brittle fracture, *J. Mech. Phys. Solids*, **48** (2000), 797–826. http://dx.doi.org/10.1016/S0022-5096(99)00028-9

14. B. Bourdin, G. Francfort, J.-J. Marigo, The variational approach to fracture, *J. Eeast.*, **91** (2008), 5–148. http://dx.doi.org/10.1007/s10659-007-9107-3

15. L. Contrafatto, M. Cuomo, L. Greco, Meso-scale simulation of concrete multiaxial behaviour, *Eur. J. Environ. Civ. Eng.*, **21** (2017), 896–911. http://dx.doi.org/10.1080/19648189.2016.1182085

16. M. Cuomo, L. Contrafatto, L. Greco, A variational model based on isogeometric interpolation for the analysis of cracked bodies, *Int. J. Eng. Sci.*, **80** (2014), 173–188. http://dx.doi.org/10.1016/j.ijengsci.2014.02.017

17. M. Cuomo, A. Nicolosi, A poroplastic model for hygro-chemo-mechanical damage of concrete, *Computational modelling of concrete structures Conference*, Mayrhofen, Austria, 2006, 533–542.

18. F. D'Annibale, G. Rosi, A. Luongo, Linear stability of piezoelectric-controlled discrete mechanical systems under nonconservative positional forces, *Meccanica*, **50** (2015), 825–839. http://dx.doi.org/10.1007/s11012-014-0037-4

19. F. dell'Isola, A. D. Corte, I. Giorgio, Higher-gradient continua: The legacy of Piola, Mindlin, Sedov and Toupin and some future research perspectives, *Math. Mech. Solids*, **22** (2017), 852–872. http://dx.doi.org/10.1177/1081286515616034

20. F. dell'Isola, L. Placidi, Variational principles are a powerful tool also for formulating field theories, In: *Variational models and methods in solid and fluid mechanics*, Vienna: Springer, 2011, 1–15. http://dx.doi.org/10.1007/978-3-7091-0983-0_1

21. F. dell'Isola, M. Guarascio, K. Hutter, A variational approach for the deformation of a saturated porous solid. A second-gradient theory extending Terzaghi's effective stress principle, *Arch. Appl. Mech.*, **70** (2000), 323–337. http://dx.doi.org/10.1007/s004199900020

22. F. Freddi, G. Royer-Carfagni, Plastic flow as an energy minimization problem. Numerical experiments, *J. Elast.*, **116** (2014), 53–74. http://dx.doi.org/10.1007/s10659-013-9457-y

23. F. Freddi, G. Royer-Carfagni, Phase-field slip-line theory of plasticity, *J. Mech. Phys. Solids*, **94** (2016), 257–272. http://dx.doi.org/10.1016/j.jmps.2016.04.024

24. M. Froli, G. Royer-Carfagni, A mechanical model for the elastic–plastic behavior of metallic bars, *Int. J. Solids Struct.*, **37** (2000), 3901–3918. http://dx.doi.org/10.1016/S0020-7683(99)00069-4

25. I. Giorgio, Numerical identification procedure between a micro-Cauchy model and a macro-second gradient model for planar pantographic structures, *Z. Angew. Math. Phys.*, **67** (2016), 95. http://dx.doi.org/10.1007/s00033-016-0692-5

26. I. Giorgio, Lattice shells composed of two families of curved Kirchhoff rods: an archetypal example, topology optimization of a cycloidal metamaterial, *Continuum Mech. Thermodyn.*, **33** (2021), 1068–1082. http://dx.doi.org/10.1007/s00161-020-00955-4

27. I. Giorgio, A. Ciallella, D. Scerrato, A study about the impact of the topological arrangement of fibers on fiber-reinforced composites: some guidelines aiming at the development of new ultra-stiff and ultra-soft metamaterials, *Int. J. Solids Struct.*, **203** (2020), 73–83. http://dx.doi.org/10.1016/j.ijsolstr.2020.07.016

28. I. Giorgio, A. Culla, D. Del Vescovo, Multimode vibration control using several piezoelectric transducers shunted with a multiterminal network, *Arch. Appl. Mech.*, **79** (2009), 859. http://dx.doi.org/10.1007/s00419-008-0258-x

29. I. Giorgio, M. Spagnuolo, U. Andreaus, D. Scerrato, A. M. Bersani, In-depth gaze at the astonishing mechanical behavior of bone: A review for designing bio-inspired hierarchical metamaterials, *Math. Mech. Solids*, **26** (2020), 1074–1103. http://dx.doi.org/10.1177/1081286520978516

30. L. Greco, An iso-parametric G1-conforming finite element for the nonlinear analysis of Kirchhoff rod. Part I: the 2D case, *Continuum Mech. Thermodyn.*, **32** (2020), 1473–1496. http://dx.doi.org/10.1007/s00161-020-00861-9

31. P. Harrison, D. Anderson, M. F. Alvarez, E. Bali, Y. Mateos, Measuring and modelling the in-plane bending stiffness and wrinkling behaviour of engineering fabrics, *EUROMECH Colloquium 569: Multiscale Modeling of Fibrous and Textile Materials*, Chatenay-Malabry, France, 5–7 April 2016.

32. C. J. Larsen, A new variational principle for cohesive fracture and elastoplasticity, *Mech. Res. Commun.*, **58** (2014), 133–138. http://dx.doi.org/10.1016/j.mechrescom.2013.10.025

33. T. Y. Li, J.-J. Marigo, D. Guilbaud, S. Potapov, Variational approach to dynamic brittle fracture via gradient damage models, *Applied Mechanics and Materials*, **784** (2015), 334–341. http://dx.doi.org/10.4028/www.scientific.net/AMM.784.334

34. M. Malikan, V. A. Eremeyev, H. M. Sedighi, Buckling analysis of a non-concentric double-walled carbon nanotube, *Acta Mech.*, **231** (2020), 5007–5020. http://dx.doi.org/10.1007/s00707-020-02784-7

35. J.-J. Marigo, C. Maurini, K. Pham, An overview of the modelling of fracture by gradient damage models, *Meccanica*, **51** (2016), 3107–3128. http://dx.doi.org/10.1007/s11012-016-0538-4

36. J.-J. Marigo, Constitutive relations in plasticity, damage and fracture mechanics based on a work property, *Nucl. Eng. Des.*, **114** (1989), 249–272. http://dx.doi.org/10.1016/0029-5493(89)90105-2

37. C. Miehe, M. Hofacker, F. Welschinger, A phase field model for rate-independent crack propagation: Robust algorithmic implementation based on operator splits, *Comput. Method. Appl. Mech. Eng.*, **199** (2010), 2765–2778. http://dx.doi.org/10.1016/j.cma.2010.04.011

38. A. Misra, Effect of asperity damage on shear behavior of single fracture, *Eng. Fract. Mech.*, **69** (2002), 1997–2014. http://dx.doi.org/10.1016/S0013-7944(02)00073-5

39. A. Misra, P. Poorsolhjouy, Granular micromechanics model for damage and plasticity of cementitious materials based upon thermomechanics, *Math. Mech. Solids*, **25** (2020), 1778–1803. http://dx.doi.org/10.1177/1081286515576821

40. A. Misra, V. Singh, Thermomechanics-based nonlinear rate-dependent coupled damage-plasticity granular micromechanics model, *Continuum Mech. Thermodyn.*, **27** (2015), 787–817. http://dx.doi.org/10.1007/s00161-014-0360-y

41. A. Misra, L. Placidi, F. dell'Isola, E. Barchiesi, Identification of a geometrically nonlinear micromorphic continuum via granular micromechanics, *Z. Angew. Math. Phys.*, **72** (2021), 157. http://dx.doi.org/10.1007/s00033-021-01587-7

42. K. Naumenko, V. A. Eremeyev, A layer-wise theory of shallow shells with thin soft core for laminated glass and photovoltaic applications, *Compos. Struct.*, **178** (2017), 434–446. http://dx.doi.org/10.1016/j.compstruct.2017.07.007

43. L. Placidi, A variational approach for a nonlinear 1-dimensional second gradient continuum damage model, *Continuum Mech. Thermodyn.*, **27** (2015), 623–638. http://dx.doi.org/10.1007/s00161-014-0338-9

44. L. Placidi, A variational approach for a nonlinear one-dimensional damage-elasto-plastic second-gradient continuum model, *Continuum Mech. Thermodyn.*, **28** (2016), 119–137. http://dx.doi.org/10.1007/s00161-014-0405-2

45. L. Placidi, E. Barchiesi, Energy approach to brittle fracture in strain-gradient modelling, *Proc. R. Soc. A*, **474** (2018), 20170878. http://dx.doi.org/10.1098/rspa.2017.0878

46. L. Placidi, E. Barchiesi, A. Misra, A strain gradient variational approach to damage: a comparison with damage gradient models and numerical results, *Math. Mech. Complex Syst.*, **6** (2018), 77–100. http://dx.doi.org/10.2140/memocs.2018.6.77

47. L. Placidi, E. Barchiesi, A. Misra, D. Timofeev, Micromechanics-based elasto-plastic–damage energy formulation for strain gradient solids with granular microstructure, *Continuum Mech. Thermodyn.*, **33** (2021), 2213–2241. http://dx.doi.org/10.1007/s00161-021-01023-1

48. P. Poorsolhjouy, A. Misra, Effect of intermediate principal stress and loading-path on failure of cementitious materials using granular micromechanics, *Int. J. Solids Struct.*, **108** (2017), 139–152. http://dx.doi.org/10.1016/j.ijsolstr.2016.12.005

49. B. Reddy, The role of dissipation and defect energy in variational formulations of problems in strain-gradient plasticity. Part 1: polycrystalline plasticity, *Continuum Mech. Thermodyn.*, **23** (2011), 527–549. http://dx.doi.org/10.1007/s00161-011-0194-9

50. B. Reddy, The role of dissipation and defect energy in variational formulations of problems in strain-gradient plasticity. Part 2: Single-crystal plasticity, *Continuum Mech. Thermodyn.*, **23** (2011), 551. http://dx.doi.org/10.1007/s00161-011-0195-8

51. J. C. Reiher, I. Giorgio, A. Bertram, Finite-element analysis of polyhedra under point and line forces in second-strain gradient elasticity, *J. Eng. Mech.*, **143** (2017), 04016112. http://dx.doi.org/10.1061/(ASCE)EM.1943-7889.0001184

52. D. Scerrato, I. Giorgio, A. Della Corte, A. Madeo, N. Dowling, F. Darve, Towards the design of an enriched concrete with enhanced dissipation performances, *Cement Concrete Res.*, **84** (2016), 48–61. http://dx.doi.org/10.1016/j.cemconres.2016.03.002

53. D. Scerrato, I. Giorgio, A. Della Corte, A. Madeo, A. Limam, A micro-structural model for dissipation phenomena in the concrete, *Int. J. Numer. Anal. Meth. Geomech.*, **39** (2015), 2037–2052. http://dx.doi.org/10.1002/nag.2394

54. D. Scerrato, I. Giorgio, A. Madeo, A. Limam, F. Darve, A simple non-linear model for internal friction in modified concrete, *Int. J. Eng. Sci.*, **80** (2014), 136–152. http://dx.doi.org/10.1016/j.ijengsci.2014.02.021

55. P. Sicsic, J.-J. Marigo, From gradient damage laws to Griffith's theory of crack propagation, *J. Elast.*, **113** (2013), 55–74. http://dx.doi.org/10.1007/s10659-012-9410-5

56. M. Spagnuolo, U. Andreaus, A targeted review on large deformations of planar elastic beams: extensibility, distributed loads, buckling and post-buckling, *Math. Mech. Solids*, **24** (2019), 258–280. http://dx.doi.org/10.1177/1081286517737000

57. M. Spagnuolo, A. M. Cazzani, Contact interactions in complex fibrous metamaterials, *Continuum Mech. Thermodyn.*, **33** (2021), 1873–1889. http://dx.doi.org/10.1007/s00161-021-01018-y

58. M. Spagnuolo, M. E. Yildizdag, X. Pinelli, A. Cazzani, F. Hild, Out-of-plane deformation reduction via inelastic hinges in fibrous metamaterials and simplified damage approach, *Math. Mech. Solids*, 2021, in press. http://dx.doi.org/10.1177/10812865211052670

59. D. Timofeev, E. Barchiesi, A. Misra, L. Placidi, Hemivariational continuum approach for granular solids with damage-induced anisotropy evolution, *Math. Mech. Solids*, **26** (2021), 738–770. http://dx.doi.org/10.1177/1081286520968149

60. E. Turco, M. Golaszewski, A. Cazzani, N. L. Rizzi, Large deformations induced in planar pantographic sheets by loads applied on fibers: experimental validation of a discrete Lagrangian model, *Mech. Res. Commun.*, **76** (2016), 51–56. http://dx.doi.org/10.1016/j.mechrescom.2016.07.001

61. E. Turco, M. Golaszewski, I. Giorgio, F. D'Annibale, Pantographic lattices with non-orthogonal fibres: Experiments and their numerical simulations, *Compos. Part B: Eng.*, **118** (2017), 1–14. http://dx.doi.org/10.1016/j.compositesb.2017.02.039

62. Y. Yang, A. Misra, Micromechanics based second gradient continuum theory for shear band modeling in cohesive granular materials following damage elasticity, *Int. J. Solids Struct.*, **49** (2012), 2500–2514. http://dx.doi.org/10.1016/j.ijsolstr.2012.05.024

AIMS Press

Chapter 3

Two-Dimensional Analysis of Size Effects in Strain-Gradient Granular Solids with Damage-Induced Anisotropy Evolution

ASCE

Two-Dimensional Analysis of Size Effects in Strain-Gradient Granular Solids with Damage-Induced Anisotropy Evolution

Valerii Maksimov[1]; Emilio Barchiesi[2]; Anil Misra, F.ASCE[3]; Luca Placidi[4]; and Dmitry Timofeev[5]

Abstract: We analyze in two dimensions the mechanical behavior of materials with granular microstructures modeled by means of a variationally formulated strain-gradient continuum approach based on micromechanics and show that it can capture microstructural-size-dependent effects. Tension-compression asymmetry of grain-assembly interactions, as well as microscale damage, is taken into account and the continuum scale is linked to the grain-scale mechanisms. Numerical results are provided for finite deformations and substantiate previous research. As expected, results show interesting size-dependent effects that are typical of strain-gradient modeling. **DOI: 10.1061/(ASCE)EM.1943-7889.0002010.**

Author keywords: Damage mechanics; Granular microstructures; Karush-Kuhn-Tucker conditions; Strain gradient; Anisotropy evolution; 2D continua.

Introduction

In this paper, we employ a model where strain gradient mechanics (macroscale) is coupled with damage granular micromechanics, being the whole formulation, i.e., both at macroscale and microscale, expressed in terms of variational statements (Abali et al. 2017; Alibert et al. 2003; Auffray et al. 2015a; dell'Isola and Placidi 2011). While the utilization of a variational formulation could be regarded as a secondary aspect compared to the analysis reported within this contribution, from the methodological point of view this aspect should not be neglected and, on the contrary, it deserves to be highlighted. Indeed, it is a merit of the approach. It is well known that not all theories formulated without a variational postulate can be turned into a variational form and for those which can—or those which are directly formulated in variational form—it is easier to assess the mathematical and physical well-posedness through properties of the energy functional like coerciveness, convexity, positive definiteness, invariance under transformation (to model anisotropy, transformations being the elements of the material symmetry group; for material symmetry groups for micromorphic media with applications to granular materials; see Eremeyev 2018), and so forth. This is especially useful when developing new or relatively unexplored theories, like second gradient ones (Cuomo et al. 2016, 2017; dell'Isola et al. 2015; Steigmann and dell'Isola 2015; Andreaus et al. 2016), as blind numerical simulations could dangerously hide many shortcomings of the modeling or, more simply, give no reasonable result. It is also worth to mention that a variational formulation is particularly convenient when dealing with the homogenization of a refined description (dell'Isola et al. 2016; Rahali et al. 2015; Carcaterra et al. 2015). Indeed, being energy a scalar quantity, computations are less cumbersome and, once the kinematics is fixed, only two postulates must be done, namely, the form of the energy functionals and the variational principle. No reasoning is required in terms of forces, neither at micro- nor at macroscales, which is usually based on physical intuition that is easily fooled and ad hoc assumptions that may give contradictory consequences or ill-posed problems (dell'Isola et al. 2015). A previously developed procedure is able to link the microscale to a properly chosen target continuum model (Simone et al. 2003; Yang and Misra 2012; Turco et al. 2016). The following points highlight the main aspects of the modeling used throughout this paper:

- derivation of objective kinematic descriptors for grain–grain relative displacement in granular materials undergoing finite deformations (Timofeev et al. 2021);
- use of Karush-Kuhn-Tucker (KKT) type conditions for grain–grain damage evolution derived as generalized Euler-Lagrange equations associated with a nonstandard variational principle (which will be henceforth termed as hemivariational; Bourdin et al. 2008; Del Piero et al. 2007; dell'Isola et al. 2009; dell'Isola and Placidi 2011; Misra et al. 2020a; Placidi 2015, 2016; Placidi et al. 2020; Auffray et al. 2015a); and
- utilization of grain–grain energy and dissipation functionals exploiting the tension-compression asymmetry as a characteristic feature of materials with granular microstructures (Poorsolhjouy and Misra 2017; Yang and Misra 2010, 2012).

[1]Ph.D. Student, Faculty of Engineering, International Telematic Univ. UNINETTUNO, Corso Vittorio Emanuele II 39, Roma 00186, Italy. ORCID: https://orcid.org/0000-0001-5985-9037

[2]Research Fellow, Universidad de Lima, Instituto de Investigación Científica, Av. Javier Prado Este 4600, Santiago de Surco 15023, Perù; Postdoctoral Fellow, École Nationale d' Ingénieurs de Brest, ENIB, UMR CNRS 6027, IRDL, 945 Avenue du Technopôle, Plouzané 29280, France (corresponding author). ORCID: https://orcid.org/0000-0002-7296-0671. Email: emilio.barchiesi@enib.fr

[3]Full Professor, Dept. of Civil, Environmental and Architectural Engineering, Univ. of Kansas, 1530 W. 15th St., Lawrence, KS 66045-7609. ORCID: https://orcid.org/0000-0002-9761-2358

[4]Associate Professor, Faculty of Engineering, International Telematic Univ. UNINETTUNO, Corso Vittorio Emanuele II 39, Roma 00186, Italy. ORCID: https://orcid.org/0000-0002-1461-3997

[5]Ph.D. Student, International Research Center on Mathematics and Mechanics of Complex Systems (M&MoCS), Università degli Studi dell' Aquila, Via Giovanni Gronchi 18—Zona industriale di Pile, L'Aquila 67100, Italy.

Note. This manuscript was submitted on February 25, 2021; approved on July 23, 2021; published online on September 10, 2021. Discussion period open until February 10, 2022; separate discussions must be submitted for individual papers. This paper is part of the ***Journal of Engineering Mechanics***, © ASCE, ISSN 0733-9399.

The following points highlight the main findings of the paper:

- grain–grain connections oriented in different directions experience different loading histories, and therefore, different normal and tangent damage evolution are observed for different grain–grain connections leading to damage-induced anisotropic response of the equivalent macroscale continuum (Placidi et al. 2010; Seddik et al. 2008; Misra and Singh 2013; Misra and Poorsolhjouy 2020; Misra and Singh 2015; Nejadsadeghi and Misra 2020; Placidi et al. 2018a, b, 2019; Poorsolhjouy and Misra 2017; Yang and Misra 2010, 2012);
- for nonhomogeneous deformations, every material point of the continuum evolves differently, both kinematically and constitutively (Carcaterra et al. 2015);
- owing to the tension-compression asymmetric behavior of grain–grain interactions and to the influence of strain-gradient effects, initially isotropic and nonchiral granular materials transform into anisotropic materials with chirality (Misra et al. 2020b; Auffray et al. 2015b); and
- strain-gradient effects in the continuum model do not only regularize the elastic results and allow for a richer account of anisotropy, but are strictly necessary to correctly describe the damage-induced evolution of the characteristic length scale as well as the damage-induced emergence of material chirality (Auffray et al. 2015b).

Model Recap

The model consists in a two-dimensional (2D) continuum moving in plane. Strain energy per unit area is assumed to read in compact form as (indices range in the set $\{1,2\}$)

$$U=\frac{1}{2}\mathbb{C}_{IJAB}G_{IJ}G_{AB}+\mathbb{M}_{IJABC}G_{IJ}G_{AB,C}+\frac{1}{2}\mathbb{D}_{IJHABC}G_{IJ,H}G_{AB,C} \tag{1}$$

where the elastic stiffnesses $\mathbb{C}$, $\mathbb{M}$, and $\mathbb{D}$ are identified from Timofeev et al. (2021) as

$$\mathbb{C}_{IJAB}=L^2\int_{\mathcal{S}^1}k_\eta(1-D_\eta)\hat{c}_I\hat{c}_J\hat{c}_A\hat{c}_B+L^2\int_{\mathcal{S}^1}k_\tau(1-D_\tau)((\delta_{IA}\hat{c}_J\hat{c}_B+\delta_{IB}\hat{c}_J\hat{c}_A+\delta_{JA}\hat{c}_I\hat{c}_B+\delta_{JB}\hat{c}_I\hat{c}_A)-4\hat{c}_I\hat{c}_J\hat{c}_A\hat{c}_B) \tag{2}$$

$$\mathbb{M}_{IJABC}=\frac{1}{4}L^3\int_{\mathcal{S}^1}k_\eta(1-D_\eta)\hat{c}_I\hat{c}_J\hat{c}_A\hat{c}_B\hat{c}_C+\frac{1}{4}L^3\int_{\mathcal{S}^1}k_\tau(1-D_\tau)((\delta_{IA}\hat{c}_J\hat{c}_B+\delta_{IB}\hat{c}_J\hat{c}_A+\delta_{JA}\hat{c}_I\hat{c}_B+\delta_{JB}\hat{c}_I\hat{c}_A)\hat{c}_C-4\hat{c}_I\hat{c}_J\hat{c}_A\hat{c}_B\hat{c}_C) \tag{3}$$

$$\mathbb{D}_{IJHABC}=\frac{1}{16}L^4\int_{\mathcal{S}^1}k_\eta(1-D_\eta)\hat{c}_I\hat{c}_J\hat{c}_H\hat{c}_A\hat{c}_B\hat{c}_C+\frac{1}{16}L^4\int_{\mathcal{S}^1}k_\tau(1-D_\tau)((\delta_{IA}\hat{c}_J\hat{c}_B+\delta_{IB}\hat{c}_J\hat{c}_A+\delta_{JA}\hat{c}_I\hat{c}_B+\delta_{JB}\hat{c}_I\hat{c}_A)\hat{c}_H\hat{c}_C-4\hat{c}_I\hat{c}_J\hat{c}_H\hat{c}_A\hat{c}_B\hat{c}_C) \tag{4}$$

where G = strain tensor; F = deformation gradient; and χ = placement function, which are respectively defined for every point X of the domain $\mathcal{B}\subseteq\mathbb{R}^2$ as

$$G=\frac{1}{2}(F^TF-I),\quad F=\nabla\chi,\quad \forall X\in\mathcal{B} \tag{5}$$

where quantity $\hat{c}$ = unit vector

$$\hat{c}=(\cos\theta,\sin\theta)$$

corresponding to a given grain–grain orientation parameterized by the angle θ and indices after a comma in the subscripts indicate the derivative with respect to the homonym component of the position X. Integrations in Eqs. (2–4) are all performed over grain–grain orientations spanning the unit circle $S^1=[0,2\pi]$. The length L is the average grain–grain distance, and k_η and k_τ are the nondamaged normal and tangent stiffnesses associated to each grain–grain. Aimed at capturing the tension-compression asymmetry, we construct the expression for k_η using the Heaviside function H as

$$k_\eta=k_\eta^tH(u_\eta)+k_\eta^cH(-u_\eta) \tag{6}$$

where u_η = normal displacement, i.e., the half-projection of the objective grain–grain relative displacement u^{np}. In formulas, we have

$$u^{np}=2G\hat{c}L+\frac{1}{2}(\nabla G\hat{c})\hat{c}L^2,\qquad u_\eta=\frac{1}{2}u^{np}\cdot\hat{c},$$
$$u_\tau=u^{np}-(u^{np}\cdot\hat{c})\hat{c} \tag{7}$$

where u_τ = so-called tangent displacement. The tangent displacement is a vector quantity. It is worth mentioning that the Heaviside function H in Eq. (6) introduces an artificial discontinuity that will be regularized in Eq. (17).

Damage is modeled by two variables, i.e., the normal damage D_η and the tangent damage D_τ, which are both functions of the position X, the grain–grain orientation $\hat{c}$, and time t. Consistently with the postulation of a dissipation energy function which reads as

$$W=\frac{1}{2}k_\eta^c(B_\eta^c)^2H(-u_\eta)\left[-D_\eta+\frac{2}{\pi}\tan\left(\frac{\pi}{2}D_\eta\right)\right]+\frac{1}{2}k_\eta^t(B_\eta^t)^2H(u_\eta)$$
$$\times[2+(D_\eta-1)(2-2\log(1-D_\eta)+(\log(1-D_\eta))^2)]$$
$$+\frac{1}{2}k_\tau[\tilde{B}_\tau(u_\eta)]^2[2+(D_\tau-1)(2-2\log(1-D_\tau)$$
$$+(\log(1-D_\tau))^2)] \tag{8}$$

two generalized Euler-Lagrange equations in the form of KKT conditions are obtained for the damage variables D_η and D_τ (Timofeev et al. 2021)

J. Eng. Mech., 2021, 147(11): 04021098

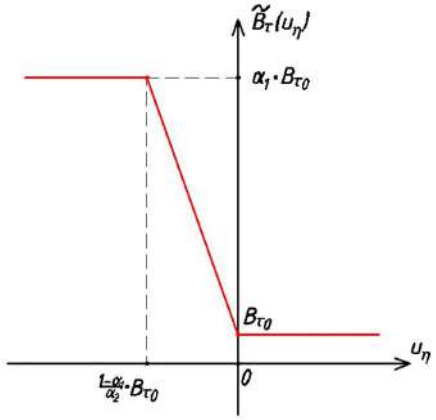

Fig. 1. Plot of the function $\widetilde{B}_\tau(u_\eta)$ defined in Eq. (11).

$$\left[u_\eta^2 - (B_\eta^t)^2 H(u_\eta)(\log(1-D_\eta))^2 - (B_\eta^c)^2 H(-u_\eta)\left[\tan\left(\frac{\pi}{2}D_\eta\right)\right]^2\right]\Delta D_\eta = 0, \quad \Delta D_\eta \geq 0 \tag{9}$$

$$[u_\tau^2 - B_\tau^2(\log(1-D_\tau))^2]\Delta D_\tau = 0, \quad \Delta D_\tau \geq 0 \tag{10}$$

where B_η^t, B_η^c, and B_τ = tension, compression, and shear damage characteristic lengths, respectively. The shear damage characteristic length B_τ is a function of the normal displacement (Fig. 1) and reads as

$$B_\tau = \tilde{B}_\tau(u_\eta) = \begin{cases} B_{\tau 0}, & u_\eta \geq 0, \\ B_{\tau 0} - \alpha_2 u_\eta, & \dfrac{1-\alpha_1}{\alpha_2} B_{\tau 0} \leq u_\eta < 0 \\ \alpha_1 B_{\tau 0}, & u_\eta < B_{\tau 0}\dfrac{1-\alpha_1}{\alpha_2} \end{cases} \tag{11}$$

where $B_{\tau 0}$ = shear damage characteristic length in tension; and α_1 and α_2 = two nondimensional parameters that characterize the shear damage characteristic length in compression. Irreversibility is encoded within the modeling by requiring the damage increments ΔD_η and ΔD_τ in Eqs. (9) and (10) to be positive.

Timofeev et al. (Timofeev et al. 2021) recently demonstrated that the strain energy per unit area in Eq. (1) is simply obtained as the integration over the unit circle $\mathcal{S}^1$ of a purely quadratic form of the aforementioned grain–grain relative displacement components

$$U = \int_{\mathcal{S}^1} \frac{1}{2} k_\eta (1-D_\eta) u_\eta^2 + \frac{1}{2} k_\tau (1-D_\tau) \|u_\tau\|^2 \tag{12}$$

where the definitions in Eq. (7) have been taken into account. The stiffnesses k_η^c, k_η^t, and k_τ are here given as input material parameters. From Eqs. (12) and (6), it is seen that these stiffnesses correspond to initial (nondamaged) grain–grain stiffnesses associated to, respectively, relative normal compression, normal tension, and shear displacements. Such stiffnesses are assumed to be initially independent of the grain–grain orientation $\hat{c}$, which is equivalent to assuming an initially isotropic behavior with null initial damage. Notwithstanding these initial conditions, anisotropy changes as the evolution of damage variables, as it is seen from Eqs. (9) and (10) and accordingly in solution algorithm described in Eq. (3), is not the same for all grain–grain orientations.

Numerical Results

Description of the Nonhomogeneous Tension Test

We investigate size-dependent properties of the model presented in Timofeev et al. (2021) via some numerical experiments. In particular, we analyze three square specimens with a circular flaw (hole) in 2D. The quantity S is the size of the sample and R_h is the hole's radius. The first sample has size $S = 10$ (cm) and $R_h = 0.12 \cdot S$, the second sample has the same size $S = 10$ (cm) but a larger radius $R_h = 0.24 \cdot S$ and the third sample has a larger size $S = 20$ (cm) and a radius $R_h = 0.12 \cdot S$ (Fig. 2). All three samples are subjected to extension tests, as drawn in Fig. 2, and the quantity $\bar{u}$ in Fig. 2 ranges monotonically from 0 to $\bar{u}_{\max}$.

Description of the Numerical Algorithm

At this point, we discuss the solution procedure that has been employed to calculate the results for the aforementioned test cases. The proprietary software COMSOL version 5.5 Multiphysics has been used to solve each of the elastic continuum simulations, which are required at the macroscale, being the strain energy per unit area that in Eq. (1). The proprietary software MATLAB has

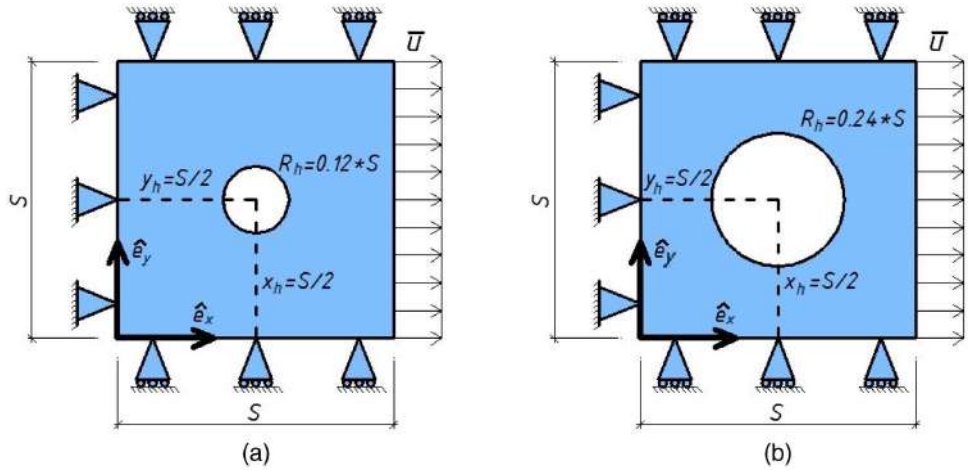

Fig. 2. Schematics of analyzed domains and considered boundary conditions. Analyzed hole radii: (a) $R_h = 0.12 \cdot S$; and (b) $R_h = 0.24 \cdot S$.

J. Eng. Mech., 2021, 147(11): 04021098

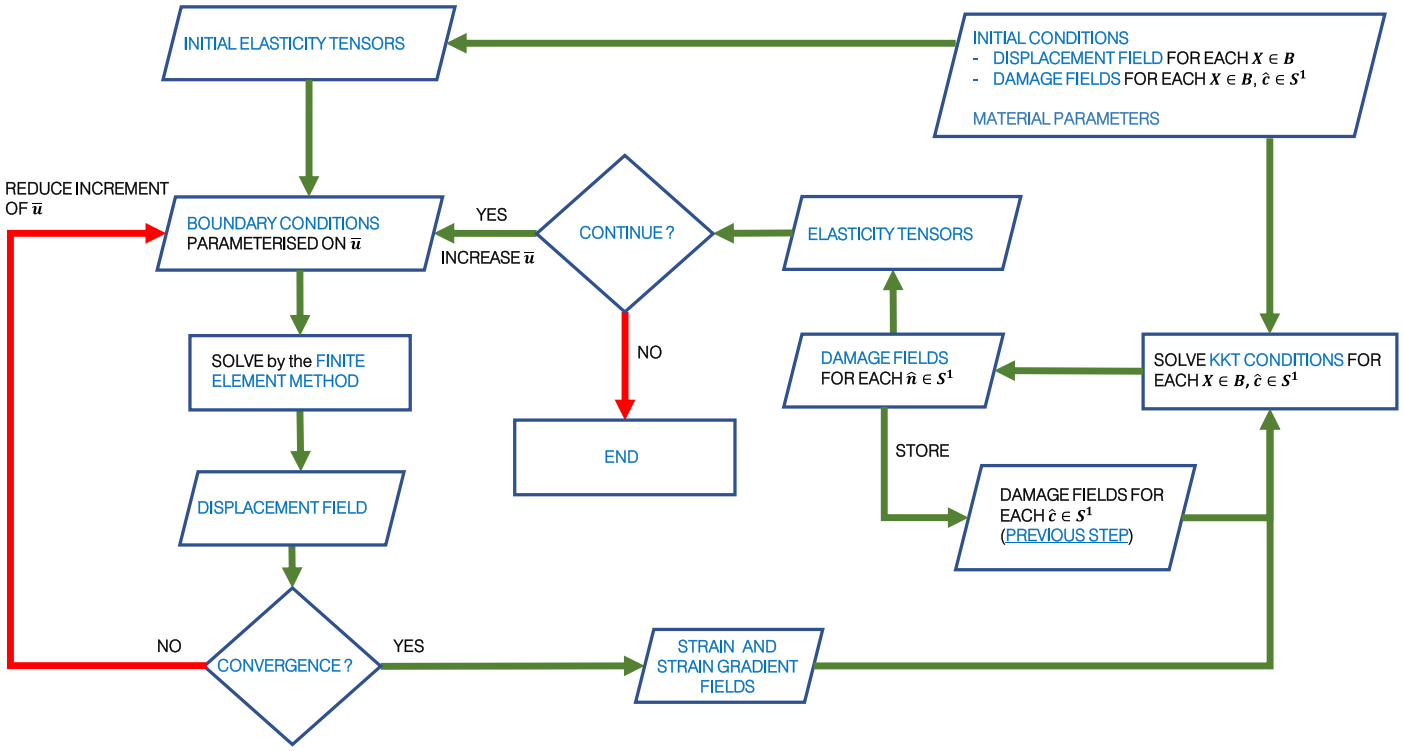

Fig. 3. Flowchart of the numerical iterative procedure used to solve the mathematical formulation.

Table 1. Values of parameters used in numerical tests

L (m)	k_η^c (J/m^4)	k_η^t (J/m^4)	k_τ (J/m^4)	B_η^c (m)	B_η^t (m)	$B_{\tau 0}$ (m)	α_1 (1)	α_2 (1)	α (1)
0.01	14×10^{14}	14×10^{13}	3×10^{13}	1.5×10^{-7}	3.5×10^{-8}	5×10^{-8}	10	14	2.5×10^{-8}

Note: Different values for L are used in the sequel for sensitivity analyses. From time to time, they are reported in the corresponding plots.

been utilized to implement the iterative procedure illustrated in the flowchart in Fig. 3—where it is clear that COMSOL Multiphysics has been indeed used only to execute the sub-routine solving the elastic equilibrium problem at macroscale—and to evaluate the KKT equations in Eqs. (9) and (10).

The iterative procedure illustrated in Fig. 3 can be summarized as follows:

1. The displacement fields u_η and u_τ, as well as the damage fields D_η and D_τ, are set to zero at the beginning of the simulation and the material parameters L, k_η^c, k_η^t, k_τ, B_η^c, B_η^t, $B_{\tau 0}$, α_1, and α_2 are given a value. The values of these parameters that were chosen to compute the results shown in this paper are reported in Table 1.
2. The elastic tensors $\mathbb{C}$, $\mathbb{M}$, and $\mathbb{D}$—which are respectively fourth-rank, fifth-rank, and sixth-rank tensors—are calculated making use of Eqs. (2)–(4). After having computed them, the tensors $\mathbb{C}$, $\mathbb{M}$, and $\mathbb{D}$ are inserted as input into the subroutine—based on COMSOL Multiphysics—for the finite element solution of the macroscale elastic equilibrium problem with chosen boundary conditions. Specifically, the weak form package of the proprietary software COMSOL Multiphysics has been used where, as shape functions, quintic Argyris polynomials were chosen to ensure C^1 continuity across elements along the normal to element boundaries. The mesh was chosen to be triangular with a Delaunay tessellation. The output obtained at the end of this subroutine is the displacement field $u = \chi - X$. Note that, to test mesh independence, various mesh sizes were considered in this study.
3. Tolerance is used to specify a simple convergence criterion that is based on comparing node-wise the tolerance with the increment of the displacement field u with respect to the previous time step. When the convergence criterion is not fulfilled, then the increment of the displacement parameter $\bar{u}$ is reduced and the subroutine based on COMSOL Multiphysics is reinitialized with the updated value of the parameter $\bar{u}$.
4. If the chosen tolerance is instead greater, for each node, than the computed increment of the displacement field with respect to the previous step, then the strain and strain-gradient fields, G and ∇G, respectively, are retrieved from the placement field χ by using Eq. (5). The normal and tangent displacements u_η and u_τ are then computed by plugging in Eq. (7) in these fields. Note that both the normal and tangent displacements u_η and u_τ are actual fields—that is, they depend on the position in space—and, additionally, they depend also on the grain-pair orientation $\hat{c}$. Finally, KKT [Eqs. (9) and (10)] are evaluated to retrieve the damage fields D_η and D_τ according to the following formulas

$$D_\eta^t = \max\{\breve{D}_\eta, D_\eta^{t-1}\}, \qquad D_\tau^t = \max\{\breve{D}_\tau, D_\tau^{t-1}\} \tag{13}$$

where the index t is employed to indicate the time loading steps and the quantities $\breve{D}_\eta$ and $\breve{D}_\tau$ are calculated by means of Eqs. (9) and (10). In formulas, we have

$$\breve{D}_\eta = 1 - \exp\left(-\frac{u_\eta}{B_\eta^t}\right), \quad u_\eta \geq 0 \tag{14}$$

$$\breve{D}_\eta = \frac{2}{\pi}\arctan\left(\frac{u_\eta}{B_\eta^c}\right), \quad u_\eta < 0 \tag{15}$$

$$\breve{D}_\tau = 1 - \exp\left(-\frac{u_\tau}{B_\tau}\right) \tag{16}$$

5. The quantity $\bar{u}$, which parameterizes the external boundary conditions, is increased.

Until a stopping condition is not reached, the aforementioned steps (except step 1) are repeated iteratively. As we anticipated at the beginning of this section, in our study the algorithm was stopped as soon as the load parameter $\bar{u}$ reached the maximum desired value $\bar{u}_{\max}$. Note also that in our numerical studies the Heaviside function $H(x)$ was replaced by the smooth—contrarily to the constitutive assumption in Eq. (6)—function (Wang and Qian 2018)

$$\frac{1}{2} + \frac{1}{\pi}\arctan\left(\frac{x}{\alpha}\right) \tag{17}$$

implying that also the nondamaged normal stiffness was retrieved as a smooth function of the normal displacement. In formulas

$$k_\eta = \frac{1}{2}(k_\eta^t + k_\eta^c) + \frac{1}{\pi}(k_\eta^t - k_\eta^c)\arctan\left(\frac{u_\eta}{\alpha}\right) \tag{18}$$

that in turns implies that the damaged normal stiffness is computed as

$$k_{\eta,D} = \frac{1}{2}(k_\eta^t + k_\eta^c)(1 - D_\eta) + \frac{1}{\pi}(k_\eta^t - k_\eta^c)\arctan\left(\frac{u_\eta}{\alpha}\right)(1 - D_\eta) \tag{19}$$

The parameter α can be used to tune the extent of the regularization. Indeed, when large values of α are used, the convergence of the algorithm is enhanced. In our study we have chosen α (see Table 1) in such a way to find a satisfying trade-off between getting a sufficiently smooth and nonstiff problem and avoiding the detrimental effect of large values of α onto the congruence of Eqs. (6). Indeed, too large values of α could imply it to acquire a physical meaning, instead of being merely a quantity related to the numerical analysis of the problem.

Convergence Analysis for the Homogeneous Tension Test

Before proceeding with the investigation of the tension test introduced in Fig. 2, for which only a numerical solution can be obtained because of the strain nonhomogeneity due to the presence of the central hole, the hole in Fig. 2 has been removed. In such a case, boundary conditions entail a homogeneous (known) strain. Therefore, a closed-form solution, which is useful to check the validity of the numerical scheme, can be obtained.

In a homogeneous deformation, strain-gradient terms in the deformation energy Eq. (1) are null, because $\nabla G = 0$ by definition. Let us define the displacement function $\boldsymbol{u}(X) \coloneqq \chi(X) - X$. Within the unit orthonormal basis $(\hat{\mathrm{e}}_x, \hat{\mathrm{e}}_y)$ in Fig. 4, analytical expressions for displacement can be given as

$$u(X_1, X_2) = \left(-\frac{\bar{u}}{S}X_1, 0\right), \quad \forall X_1 \in [0, S], \quad \forall X_2 \in [0, S] \tag{20}$$

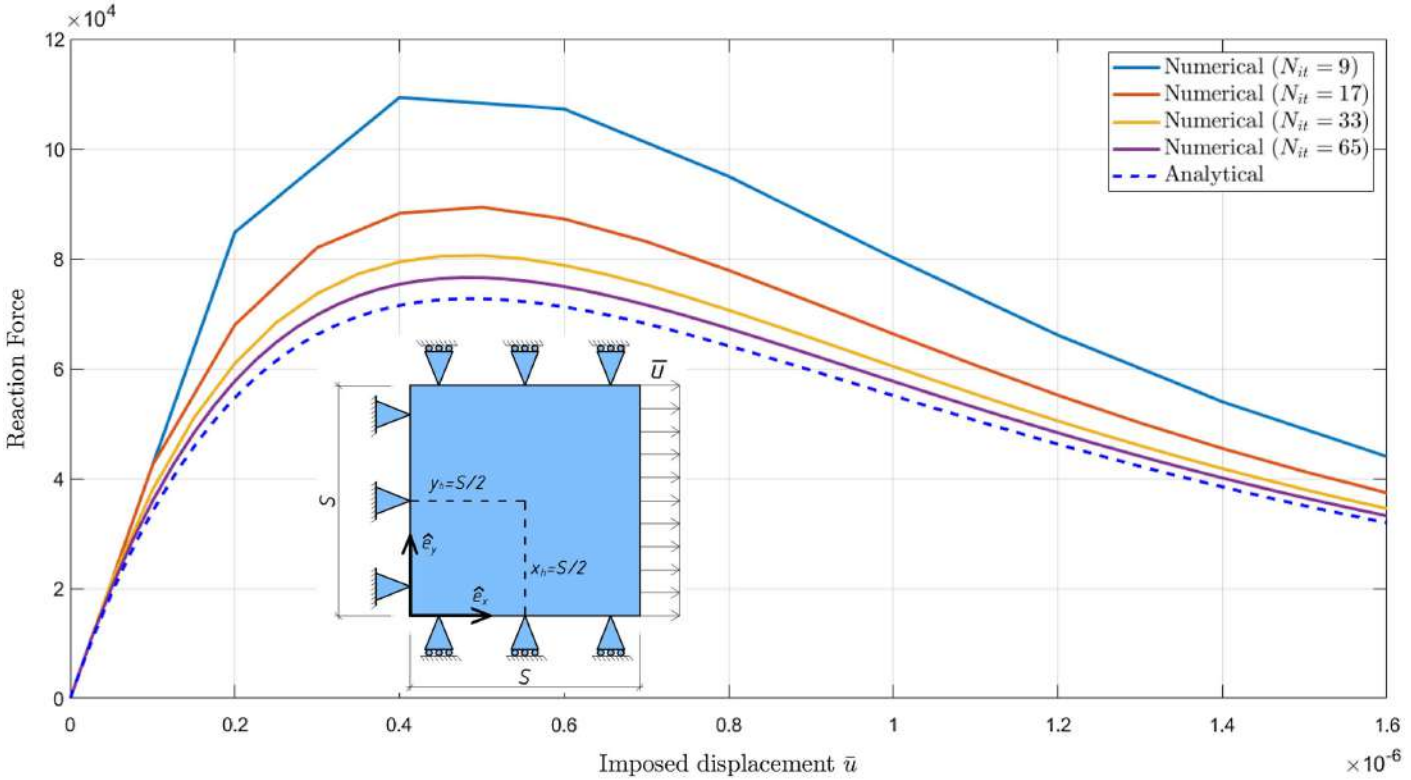

Fig. 4. Convergence analysis with respect to the number of load steps N_{it} in case of the homogeneous tension test. Global elastic response, i.e., total reaction force versus imposed displacement, diagrams for different numbers of steps compared with the analytical result along with the schematics of the analyzed domain and considered boundary conditions.

J. Eng. Mech., 2021, 147(11): 04021098

Table 2. Numerical values used in numerical simulations for nonhomogeneous tests

	S = 0.1 m			S = 0.2 m		
N_θ	N_{iter}	$\Delta\bar{u}$ (m)	$\bar{u}_{\max}$(m)	N_{iter}	$\Delta\bar{u}$ (m)	$\bar{u}_{\max}$(m)
120	25	2.5×10^{-8}	62.5×10^{-8}	25	5×10^{-8}	$12,5 \times 10^{-7}$

Note: $\bar{u}_{\max}/S$ is the same.

Eq. (20) defines the Green-Saint-Venant strain tensor which, upon integration, allows to obtain normal and tangetial objective relative displacements as

$$G = \begin{pmatrix} \frac{\bar{u}}{S}\left(-1+\frac{\bar{u}}{2S}\right) & 0 \\ 0 & 0 \end{pmatrix}$$
$$\Rightarrow \begin{cases} u_\eta = 2\bar{u}L\left(-1+\frac{\bar{u}}{2S}\right)\cos^2(\theta), \\ u_\tau^2 = \left[2\bar{u}L\left(-1+\frac{\bar{u}}{2S}\right)\cos(\theta)\sin(\theta)\right]^2 \end{cases} \tag{21}$$

Fig. 4 reports a convergence analysis to the exact solution of the numerical algorithm with respect to the chosen number of iterations N_{it} along with the schematics of the analyzed domain and the considered boundary conditions for the plain square domain. It is clearly seen that, as expected, the higher is the number of steps chosen for the pseudo-time discretization, the better is the numerical outcome as compared to the analytical solution, which indicates convergence of the numerical scheme to the exact solution.

Numerical Results for the Nonhomogeneous Tension Test

The grain–grain orientation has been parameterized with the angle θ, which is discretized in a number N_θ of knots. Besides, the loading parameter $\bar{u}$ is considered as ranging monotonically (this is the reason why within this contribution it can be considered as a pseudo-time) in the interval $[0, \bar{u}_{\max}]$, being such an interval discretized, according to the iterative procedure illustrated in the section "Description of the Numerical Algorithm," in a number N_{it} of time steps. Hence, the loading increment $\Delta\bar{u}$ changes with N_{it}. For all the performed calculations, we keep the same set of constitutive parameters per Table 1. Moreover, the sample in Fig. 2(a) has been investigated for $S = 0.1$ (m) and $\Delta\bar{u} = 2.5 \times 10^{-8}$ (m), while the sample in Fig. 2(b) has been analyzed for $S = 0.2$ (m) and $\Delta\bar{u} = 12.5 \times 10^{-7}$ (m). Numerical values of parameters that have been used to obtain the results presented in this section are provided in Table 2.

It is clear that the presence of the circular hole in Fig. 2 leads to nonhomogeneous deformations and strain-localization is expected. Such localization, since damage is accounted for in the modeling, results eventually in material failure when damage parameters reach or, actually, are close to unity.

Fig. 5 shows contour plots of the elastic energy at different time steps.

From this figure we observe that larger hole's radii imply small sample areas and this, in turn implies, that the maximum value of the elastic energy density, that is, 2 J/m^2, which is the same for all the considered data sets, is reached in less steps.

Fig. 6 shows the contour plots of dissipation energy at different time steps. Here it is possible to conclude that the thickness of the

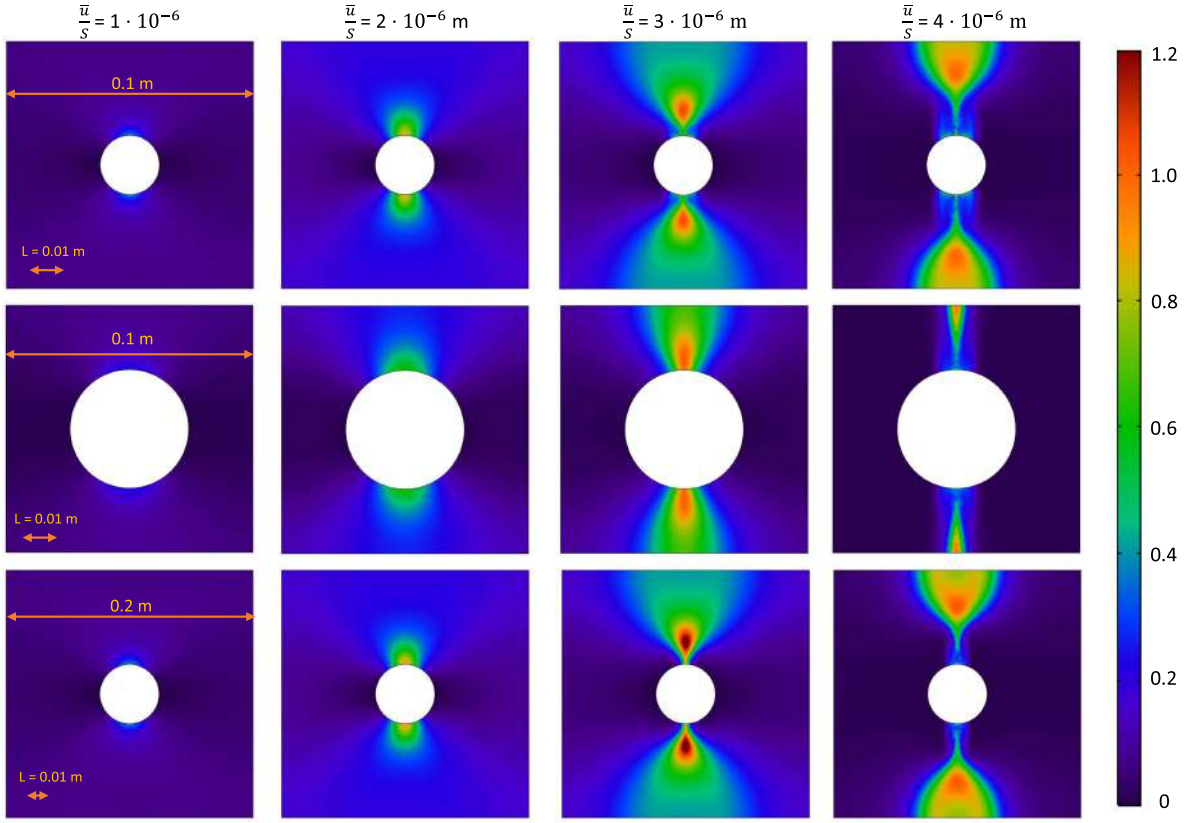

Fig. 5. Comparison of contour plots of elastic energy density evolution for different samples: in the first line $S = 0.1$ m and $R_h = 0.012$ m, in the second line $S = 0.1$ m and $R_h = 0.024$ m, and in the third line $S = 0.2$ m and $R_h = 0.024$. All quantities are expressed in J/m^2.

J. Eng. Mech., 2021, 147(11): 04021098

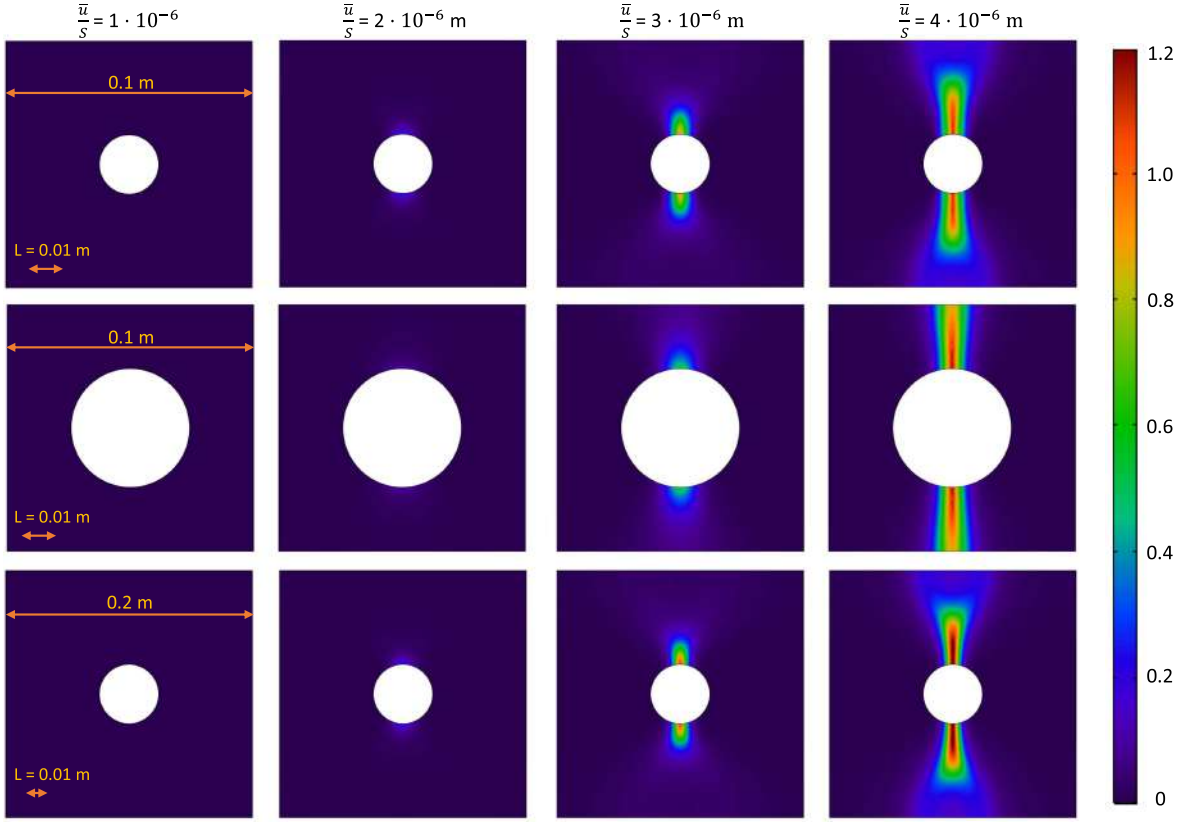

Fig. 6. Comparison of contour plots of dissipation energy density evolution for increasing loading steps for different samples: in the first line $S = 0.1$ m and $R_h = 0.012$ m, in the second line $S = 0.1$ m and $R_h = 0.024$ m, and in the third line $S = 0.2$ m and $R_h = 0.024$ m. All quantities are expressed in $\mathrm{J/m^2}$.

region where the dissipation energy attains its maximum value is the same for all the considered data sets.

In this regard, it is worth to notice that Fig. 7, which shows contour plots of dissipation energy density for $\bar{u}/S = 4 \times 10^{-6}$ and samples with different side size (in the same scale), suggests that such a thickness depends on the constitutive parameter L, while it and does not depend on the geometry of the sample.

Figs. 8 and 9 show the polar plots of damage descriptors D_η and D_τ at different representative points of the samples. Polar plots are symmetric with respect to the central axes of the sample,

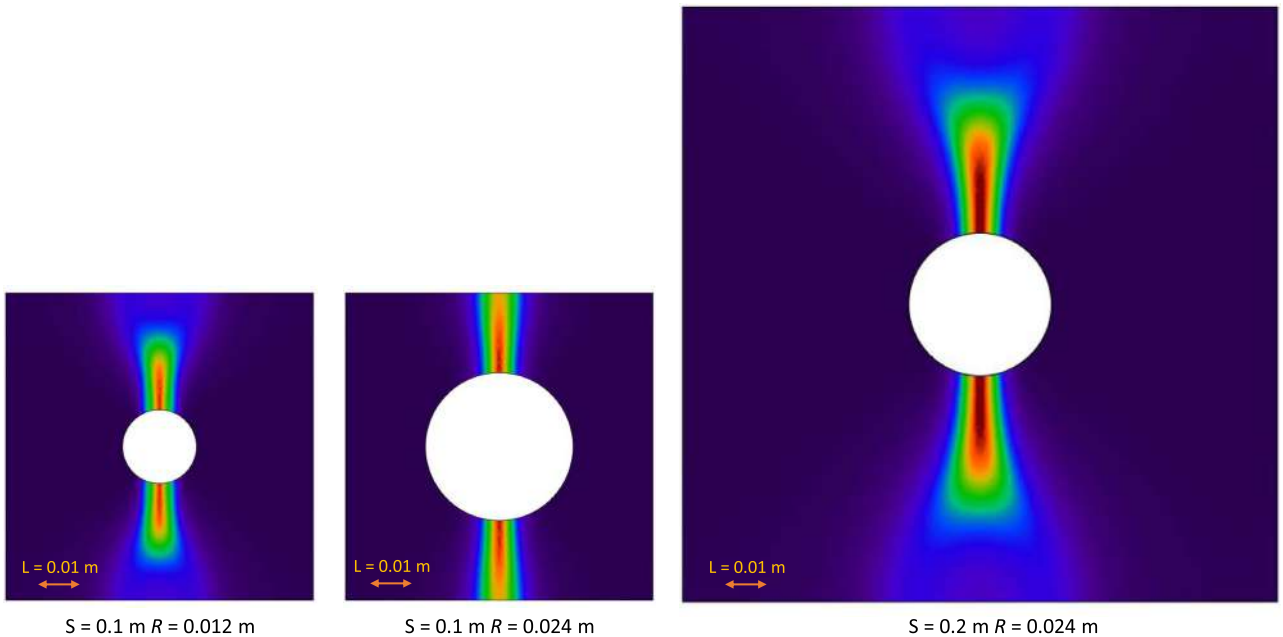

Fig. 7. Contour plots of dissipation energy densities for $\bar{u}/S = 4 \times 10^{-6}$ and for different samples.

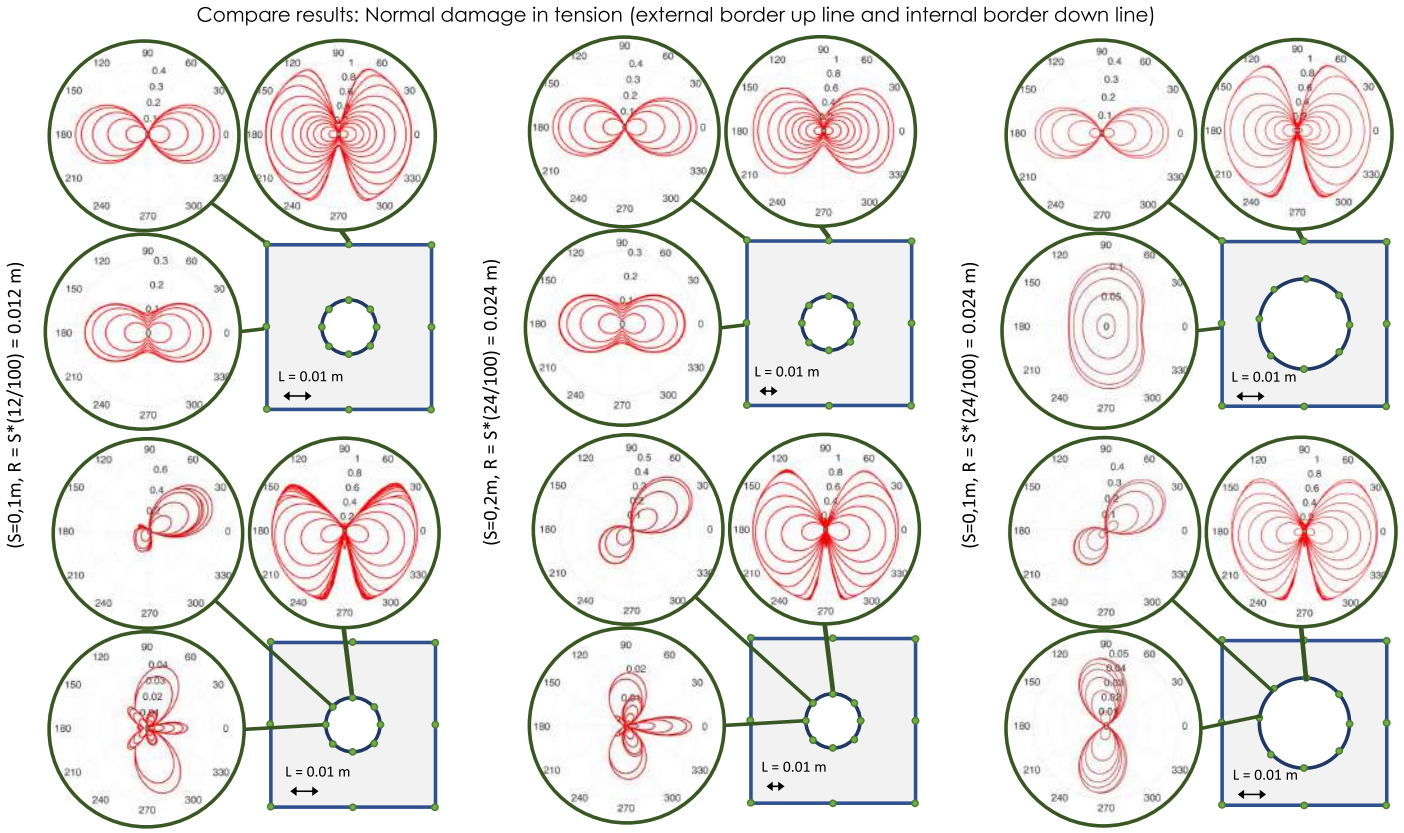

Fig. 8. Evolution of $D_\eta(\theta)$ at selected boundary points for different samples.

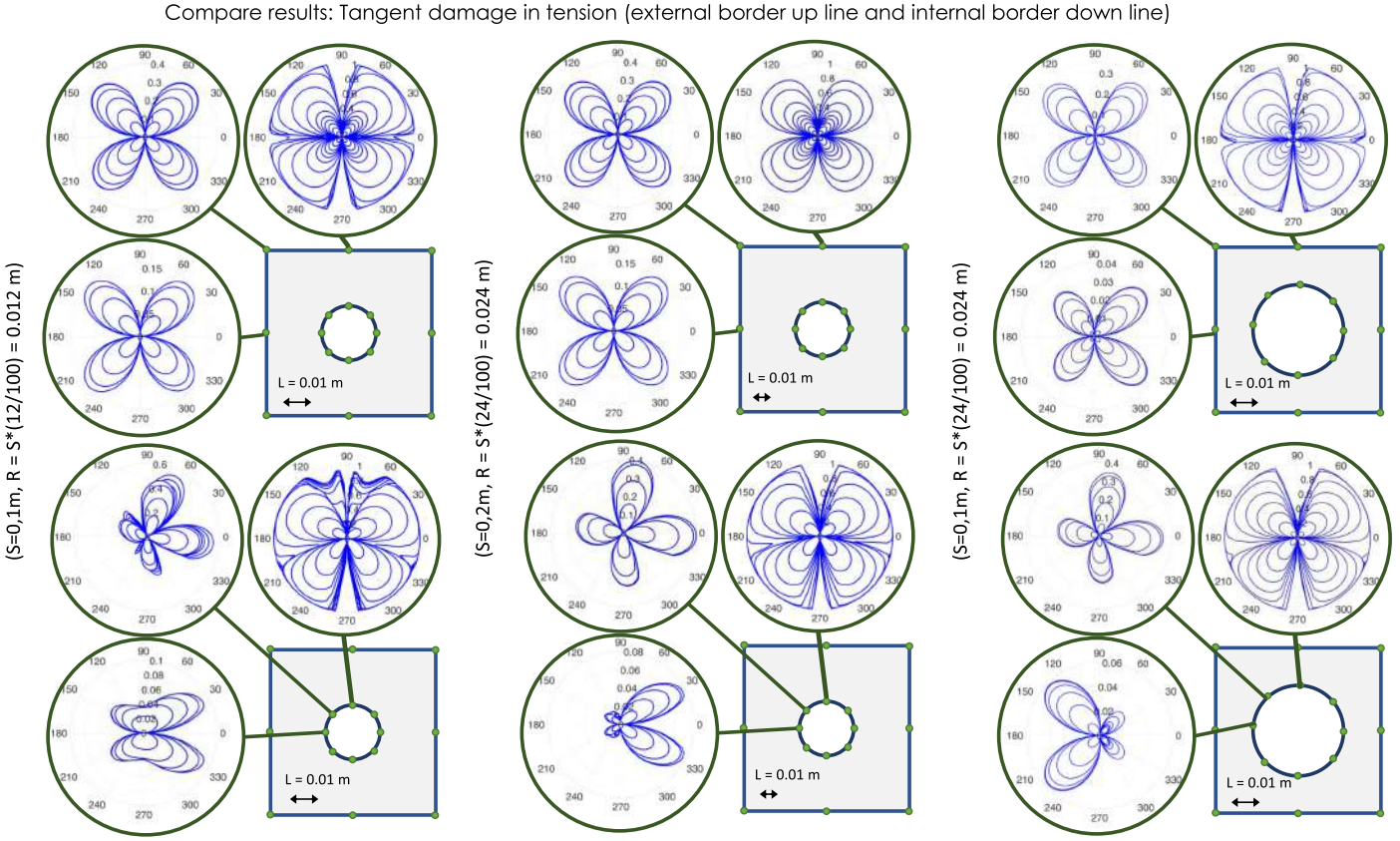

Fig. 9. Evolution of $D_\tau(\theta)$ at selected boundary points for different samples.

hence for each sample only those in the upper-left quadrant are reported.

At the hole's boundary, the strain-gradient was higher, and this led to a higher magnitude of the chiral stiffness matrix [Eq. (3)]. Indeed, the damage evolution became noncentro-symmetric.

Concluding Remarks

In this contribution, we have assessed quantitatively the influence of the hole's size with respect to the side size on the evolution of the elastic and dissipation energies for a centrally holed square sample made up of granular material within the context of a recently introduced strain-gradient continuum theory based on micromechanics. We found that the higher the hole's radius, the higher is the maximum value of the elastic energy reached for the same prescribed displacement. The higher the radius, the faster is the propagation of both the dissipation and the elastic energies from the hole's to the external square's boundaries. In standard damage models there is no size dependency of the results. Moreover, standard numerical approaches are highly mesh dependent. Here, by introducing second gradient effects, we overcome this limitation. The obtained numerical results show that the size of the area subjected to damage has the same order of magnitude of the intergranular distance, i.e., the constitutive parameter L, which is much larger than a single finite element. Furthermore, the utilized model can capture increasing the size of damaged area with the increase in the size of the sample (Fig. 7). For two different size of the sample different results were obtained for the dissipation energy: the larger the damaged area, the more energy is dissipated.

Fig. 7 shows that the thickness of the region where the maximum value of the dissipation energy density is attained is the same for all the numerical experiments. This allows to conclude that such a thickness depends on the constitutive parameter L, while it does not depend on the geometric dimensions of the sample.

Data Availability Statement

All data, models, or code that support the findings of this study are available from the corresponding author upon reasonable request.

Acknowledgments

AM is partially supported by the United States National Science Foundation grant CMMI-1727433. LP is partially supported by the RESBA project (from Politecnico di Torino).

References

Abali, B., W. Müller, and F. dell'Isola. 2017. "Theory and computation of higher gradient elasticity theories based on action principles." *Arch. Appl. Mech.* 87 (9): 1495–1510. https://doi.org/10.1007/s00419-017-1266-5.

Alibert, J.-J., P. Seppecher, and F. dell'Isola. 2003. "Truss modular beams with deformation energy depending on higher displacement gradients." *Math. Mech. Solids* 8 (1): 51–73. https://doi.org/10.1177/1081286503008001658.

Andreaus, U., F. dell'Isola, I. Giorgio, L. Placidi, T. Lekszycki, and N. Rizzi. 2016. "Numerical simulations of classical problems in two-dimensional (non) linear second gradient elasticity." *Int. J. Eng. Sci.* 108 (Nov): 34–50. https://doi.org/10.1016/j.ijengsci.2016.08.003.

Auffray, N., F. dell'Isola, V. Eremeyev, A. Madeo, and G. Rosi. 2015a. "Analytical continuum mechanics à la Hamilton–Piola least action principle for second gradient continua and capillary fluids." *Math. Mech. Solids* 20 (4): 375–417. https://doi.org/10.1177/1081286513497616.

Auffray, N., J. Dirrenberger, and G. Rosi. 2015b. "A complete description of bi-dimensional anisotropic strain-gradient elasticity." *Int. J. Solids Struct.* 69–70 (Sep): 195–206. https://doi.org/10.1016/j.ijsolstr.2015.04.036.

Bourdin, B., G. Francfort, and J.-J. Marigo. 2008. "The variational approach to fracture." *J. Elast.* 91 (1): 5–148. https://doi.org/10.1007/s10659-007-9107-3.

Carcaterra, A., F. dell'Isola, R. Esposito, and M. Pulvirenti. 2015. "Macroscopic description of microscopically strongly inhomogeneous systems: A mathematical basis for the synthesis of higher gradients metamaterials." *Arch. Ration. Mech. Anal.* 218 (3): 1239–1262. https://doi.org/10.1007/s00205-015-0879-5.

Cuomo, M., F. dell'Isola, and L. Greco. 2016. "Simplified analysis of a generalized bias test for fabrics with two families of inextensible fibres." *Zeitschrift für angewandte Mathematik und Physik* 67 (3): 61. https://doi.org/10.1007/s00033-016-0653-z.

Cuomo, M., F. dell'Isola, L. Greco, and N. Rizzi. 2017. "First versus second gradient energies for planar sheets with two families of inextensible fibres: Investigation on deformation boundary layers, discontinuities and geometrical instabilities." *Composites, Part B* 115 (Apr): 423–448. https://doi.org/10.1016/j.compositesb.2016.08.043.

dell'Isola, F., I. Giorgio, M. Pawlikowski, and N. L. Rizzi. 2016. "Large deformations of planar extensible beams and pantographic lattices: Heuristic homogenization, experimental and numerical examples of equilibrium." *Proc. R. Soc. London, Ser. A: Math. Phys. Eng. Sci.* 472 (2185): 20150790. https://doi.org/10.1098/rspa.2015.0790.

dell'Isola, F., A. Madeo, and P. Seppecher. 2009. "Boundary conditions at fluid-permeable interfaces in porous media: A variational approach." *Int. J. Solids Struct.* 46 (17): 3150–3164. https://doi.org/10.1016/j.ijsolstr.2009.04.008.

dell'Isola, F., and L. Placidi. 2011. "Variational principles are a powerful tool also for formulating field theories." In *Variational models and methods in solid and fluid mechanics*, 1–15. Vienna, Austria: Springer.

dell'Isola, F., P. Seppecher, and A. Della Corte. 2015. "The postulations á la D'Alembert and á la Cauchy for higher gradient continuum theories are equivalent: A review of existing results." *Proc. R. Soc. London, Ser. A* 471 (2183): 20150415. https://doi.org/10.1098/rspa.2015.0415.

Del Piero, G., G. Lancioni, and R. March. 2007. "A variational model for fracture mechanics: Numerical experiments." *J. Mech. Phys. Solids* 55 (12): 2513–2537. https://doi.org/10.1016/j.jmps.2007.04.011.

Eremeyev, V. A. 2018. "On the material symmetry group for micromorphic media with applications to granular materials." *Mech. Res. Commun.* 94 (Dec): 8–12. https://doi.org/10.1016/j.mechrescom.2018.08.017.

Misra, A., P. Luca, and E. Turco. 2020a. "Variational methods for discrete models of granular materials." In *Encylopedia of continuum mechanics*. Berlin: Springer.

Misra, A., N. Nejadsadeghi, M. De Angelo, and L. Placidi. 2020b. "Chiral metamaterial predicted by granular micromechanics: Verified with 1D example synthesized using additive manufacturing." *Continuum Mech. Thermodyn.* 32 (5): 1497–1513. https://doi.org/10.1007/s00161-020-00862-8.

Misra, A., and P. Poorsolhjouy. 2020. "Granular micromechanics model for damage and plasticity of cementitious materials based upon thermomechanics." *Math. Mech. Solids* 25 (10): 1778–1803. https://doi.org/10.1177/1081286515576821.

Misra, A., and V. Singh. 2013. "Micromechanical model for viscoelastic materials undergoing damage." *Continuum Mech. Thermodyn.* 25 (2): 343–358. https://doi.org/10.1007/s00161-012-0262-9.

Misra, A., and V. Singh. 2015b. "Thermomechanics-based nonlinear rate-dependent coupled damage-plasticity granular micromechanics model." *Contin. Mech. Thermodyn.* 27 (4–5): 787. https://doi.org/10.1007/s00161-014-0360-y.

Nejadsadeghi, N., and A. Misra. 2020. "Extended granular micromechanics approach: A micromorphic theory of degree n." *Math. Mech. Solids* 25 (2): 407–429. https://doi.org/10.1177/1081286519879479.

Placidi, L. 2015. "A variational approach for a nonlinear 1-dimensional second gradient continuum damage model." *Continuum Mech. Thermodyn.* 27 (4–5): 623. https://doi.org/10.1007/s00161-014-0338-9.

Placidi, L. 2016. "A variational approach for a nonlinear one-dimensional damage-elasto-plastic second-gradient continuum model." *Continuum Mech. Thermodyn.* 28 (1–2): 119–137. https://doi.org/10.1007/s00161-014-0405-2.

Placidi, L., E. Barchiesi, and A. Misra. 2018a. "A strain gradient variational approach to damage: A comparison with damage gradient models and numerical results." *Math. Mech. Complex Syst.* 6 (2): 77–100. https://doi.org/10.2140/memocs.2018.6.77.

Placidi, L., E. Barchiesi, A. Misra, and U. Andreaus. 2020. "Variational methods in continuum damage and fracture mechanics." In *Encylopedia of continuum mechanics*. Berlin: Springer.

Placidi, L., R. Greve, H. Seddik, and S. Faria. 2010. "Continuum-mechanical, anisotropic flow model for polar ice masses, based on an anisotropic flow enhancement factor." *Continuum Mech. Thermodyn.* 22 (3): 221–237. https://doi.org/10.1007/s00161-009-0126-0.

Placidi, L., A. Misra, and E. Barchiesi. 2018b. "Two-dimensional strain gradient damage modeling: A variational approach." *Zeitschrift für angewandte Mathematik und Physik* 69 (3): 56. https://doi.org/10.1007/s00033-018-0947-4.

Placidi, L., A. Misra, and E. Barchiesi. 2019. "Simulation results for damage with evolving microstructure and growing strain gradient moduli." *Continuum Mech. Thermodyn.* 31 (4): 1143–1163. https://doi.org/10.1007/s00161-018-0693-z.

Poorsolhjouy, P., and A. Misra. 2017. "Effect of intermediate principal stress and loading-path on failure of cementitious materials using granular micromechanics." *Int. J. Solids Struct.* 108 (Mar): 139–152. https://doi.org/10.1016/j.ijsolstr.2016.12.005.

Rahali, Y., I. Giorgio, J. Ganghoffer, and F. dell'Isola. 2015. "Homogenization à la Piola produces second gradient continuum models for linear pantographic lattices." *Int. J. Eng. Sci.* 97 (Dec): 148–172. https://doi.org/10.1016/j.ijengsci.2015.10.003.

Seddik, H., R. Greve, L. Placidi, I. Hamann, and O. Gagliardini. 2008. "Application of a continuum-mechanical model for the flow of anisotropic polar ice to the EDML core, Antarctica." *J. Glaciol.* 54 (187): 631–642. https://doi.org/10.3189/002214308786570755.

Simone, A., G. Wells, and L. Sluys. 2003. "From continuous to discontinuous failure in a gradient-enhanced continuum damage model." *Comput. Methods Appl. Mech. Eng.* 192 (41): 4581–4607. https://doi.org/10.1016/S0045-7825(03)00428-6.

Steigmann, D., and F. dell'Isola. 2015. "Mechanical response of fabric sheets to three-dimensional bending, twisting, and stretching." *Acta Mech. Sin.* 31 (3): 373–382. https://doi.org/10.1007/s10409-015-0413-x.

Timofeev, D., E. Barchiesi, A. Misra, and L. Placidi. 2021. "Hemivariational continuum approach for granular solids with damage-induced anisotropy evolution." *Math. Mech. Solids* 26 (5): 738–770. https://doi.org/10.1177/1081286520968149.

Turco, E., F. dell'Isola, A. Cazzani, and N. Rizzi. 2016. "Hencky-type discrete model for pantographic structures: Numerical comparison with second gradient continuum models." *Z. Angew. Math. Phys.* 67 (85): 1–28. https://doi.org/10.1007/s00033-016-0681-8.

Wang, C., and X. Qian. 2018. "Heaviside projection based aggregation in stress constrained topology optimization." *Int. J. Numer. Methods Eng.* 115 (7): 849–871. https://doi.org/10.1002/nme.5828.

Yang, Y., and A. Misra. 2010. "Higher-order stress-strain theory for damage modeling implemented in an element-free Galerkin formulation." *Comput. Model. Eng. Sci.* 64 (1): 1–36. https://doi.org/10.3970/cmes.2010.064.001.

Yang, Y., and A. Misra. 2012. "Micromechanics based second gradient continuum theory for shear band modeling in cohesive granular materials following damage elasticity." *Int. J. Solids Struct.* 49 (18): 2500–2514. https://doi.org/10.1016/j.ijsolstr.2012.05.024.

Chapter 4

Micro-mechano-morphology-informed continuum damage modeling with intrinsic 2nd gradient (pantographic) grain–grain interactions

Contents lists available at ScienceDirect

International Journal of Solids and Structures

journal homepage: www.elsevier.com/locate/ijsolstr

Micro-mechano-morphology-informed continuum damage modeling with intrinsic 2nd gradient (pantographic) grain–grain interactions

Luca Placidi [a], Dmitry Timofeev [b], Valerii Maksimov [a,*], Emilio Barchiesi [c,d], Alessandro Ciallella [b], Anil Misra [e], Francesco dell'Isola [b]

[a] Faculty of Engineering, International Telematic University UNINETTUNO, Rome, Italy
[b] International Research Center on Mathematics and Mechanics of Complex Systems (M&MoCS), Università degli Studi dell'Aquila, L'Aquila, Italy
[c] École Nationale d'Ingénieurs de Brest, ENIB, UMR CNRS 6027, IRDL, F-29200 Brest, France
[d] Université de Bretagne Sud, IRDL-UBS - UMR CNRS 6027, Centre de Recherche, Rue de Saint Maudé - BP 92116 56321, Lorient, Cedex, France
[e] Civil, Environmental and Architectural Engineering Department, The University of Kansas, Kansas City, KS, USA

ARTICLE INFO

Keywords:
Damage mechanics
Granular microstructures
Karush–Kuhn–Tucker conditions
Strain gradient
2D continua

ABSTRACT

In a previous work, we have shown that a granular micromechanics approach can lead to load path dependent continuum models. In the present work, we generalize such a micromechanical approach introducing an intrinsic 2nd gradient energy storage mechanism (resembling pantographic micromechanism), in the grain–grain interaction. Such a mechanism, represents long-range effects but could also be thought as deriving from the utilization of an actual pantographic connection between two grains in a granular metamaterial. Taking advantage of the homogenization approach developed in previous works, we determine the mechanical behavior of the macro-scale continuum and carry out parametric analyses with respect to the averaged intergranular distance and with respect to the stiffness associated to the pantographic term. We show that with the inclusion of the pantographic term mentioned above, the desired thickness of the localization zone can be modeled and finely tuned successfully. We also show that the complex mechanics of load-path dependency can be predicated by the micromechanical effects and the introduced pantographic term.

1. Introduction

Damage and fracture can significantly impair the safety and operational capacity of many engineering devices and structures. Occurrence of damage often represents the extreme load scenario that drives the design. Therefore, resilience of modern engineering architectures with respect to damage, especially in critical applications like aeronautics, civil engineering and mechanical engineering, is often one of the main cost-driving factors.

Since it is often difficult and economically nonviable to validate (Oberkampf et al., 2004; Schwer, 2007; Babuska and Oden, 2004; TMS, 2019) by experimental means the real damage tolerance of a new architecture apart from scaled-down trials, with the design load cases often remaining untested, there is an increasing need for reliable modeling and related numerical protocols helping towards the objective above. One of the main challenges in damage mechanics is that loss of stiffness and failure of mechanical systems are often accompanied by localization of deformation (Placidi et al., 2018a,b). It is well known that numerical simulation of such problems utilizing methods such as classical fracture mechanics or classical damage mechanics presents serious shortcomings. For example, classical linear elastic fracture mechanics is unable to predict weakening or nucleation of defects at locations away from existing cracks, such as from boundaries that could appear, among others, due to material damage or weakness and related localization of deformation (Tokaji et al., 1987; Pook, 2000). Similarly, classical damage mechanics suffers from instabilities associated with loss of ellipticity, which typically requires certain regularization, particularly for simulating coalescence of microfractures into concentrated zones and for producing results that are independent of mesh size and shape used in numerical simulations (Kumar et al., 2020; Tanné et al., 2018; Fang et al., 2020; Carrara et al., 2020; Brach et al., 2019).

In recent years, phase-field models that include regularization have been proposed to address some of the above-mentioned shortcomings (Molnár et al., 2020; Miehe et al., 2016). However, further developments are needed, as many of these existing methods, including phase field methods, do not treat the effect of load paths and pre-loading upon the fracture paths and their evolution (Nguyen et al., 2020; Ouali et al., 2021). Moreover, localization zones (or shear bands) and boundary layers observed in many experiments are of finite spatial dimension and

* Corresponding author.
E-mail address: v.maksimov@students.uninettunouniversity.net (V. Maksimov).

https://doi.org/10.1016/j.ijsolstr.2022.111880
Received 7 December 2021; Received in revised form 15 June 2022; Accepted 14 July 2022

they exist irrespective of the size of the domain (size of the structure). Regularization approaches proposed within the above mentioned classical and phase field approaches do not address the question of size of the localization zone, particularly from a micro-mechano-morphological viewpoint. In addition, in many past micro-macro identification, the 2nd gradient energy derived from lattice or discrete models depends upon the 1st gradient energy, and the 2nd gradient stiffnesses are proportional to 1st gradient ones and to the square of the RVE or to the lattice size (Askes and Metrikine, 2005; Askes and Aifantis, 2011; Chang and Gao, 1995; Maranganti and Sharma, 2007; Triantafyllidis and Bardenhagen, 1993). In these cases, and in the limit of such a size going to zero, the 2nd gradient constants vanish. Such schemes, therefore, cannot ex in that limit (i) a finite localization zone, that is in fact independent on grain sizes, and (ii) the fact that similar grain sizes lead to different shear band thickness (Jia et al., 2003; Polyzos and Fotiadis, 2012), an observation that can be attributed to correct micro-macro identification of kinematical features, including the effect of grain-rotation and other long-range effects. It is also noteworthy that strain localization could be accompanied by band broadening (Joshi and Ramesh, 2008) due to the evolution of micro-mechano-morphological effects an aspect that conventional fracture mechanics or shear band modeling largely overlooks (Placidi et al., 2019). To develop an approach in which we can incorporate the dependence upon the load-path and be able to regulate the localization zone thickness we utilize the micro-macro identification formalism based upon granular micromechanics (Misra et al., 2021; Placidi et al., 2021), in which it is considered that the elastic strain energy is stored and/or energy is dissipated in the deformation mechanisms representing interaction of grain-pairs. Such a deformation is modeled by relative motions of grain bary-centers, regardless of the location of the actual deformation within the grains.

It should be noted that, owing to recent advances in versatile manufacturing techniques as additive manufacturing allowing for their rapid production (Seppecher et al., 2019; Golaszewski et al., 2019; Spagnuolo et al., 2019; Trippel et al., 2020), architected materials, also known as metamaterials (Carcaterra et al., 2015; Del Vescovo and Giorgio, 2014; dell'Isola et al., 2016a), have become widespread in several fields of engineering. Indeed, properly designed architected materials can exhibit extremely favorable mechanical performances like low weight-to-stiffness ratios (Zheng et al., 2014; Giorgio et al., 2020a), high element-failure tolerance (Turco et al., 2016; Turco and Rizzi, 2016), and high energy-absorption capability (Mohsenizadeh et al., 2018). This has further urged theoretical mechanicians to take into account the significance of micro-scale mechanisms in influencing macro-scale material behaviors. Indeed, the main idea underlying the development of so-called metamaterials is the production of materials with artificially-controlled architecture conferring desired properties to the material (Yildizdag et al., 2019). Recently, the homogenization of different pantographic motifs (dell'Isola et al., 2016b; Rahali et al., 2015; Coutris et al., 2020; Boutin et al., 2017; dell'Isola et al., 2019), i.e. a mechanism which is well known from everyday life (pantographic mirrors, expanding fences, scissor lifts, etc.), which is characterized by a zero-energy accordion-like homogeneous extension/compression deformation mode, has been addressed for this reason. The studies on the homogenization of the above-mentioned pantographic motifs has concluded that, at macro-scale, they behave as second gradient continua. More particularly, the deformation energy of pantographic beams (Turco, 2019, 2021; Turco et al., 2021), i.e. slender pantographic structures, in contrast to the Elastica for which the deformation energy depends on the projection of the second gradient to the normal vector of the placement function, i.e. the material curvature, does also depend on the projection onto the tangent vector, introduced as the stretch gradient. Thus, the deformation energy takes into account the complete second gradient of the placement function. In such a model, non-standard boundary conditions and more generalized forces such as double forces do appear (Barchiesi et al., 2019, 2018). In other words, pantographic beams exhibit second gradient effects, i.e. non-locality or second-neighbor interactions, also in extension/compression and not only in bending, as standard beam models.

In previous works, we have proved that a granular micromechanics approach can lead to load path dependent outcomes (Placidi et al., 2021; Timofeev et al., 2020). Here, we generalize the grain-pair interaction by introducing an additional pantographic energy storage mechanism that depends upon strain gradient, and therefore, represents long-range (beyond nearest neighbor) effects that characterize all discrete systems and that need to be accounted for continuum models to be representative. More specifically, a spring is introduced at the micro-scale accumulating energy upon the gradient of its stretch, which can be regarded at a lower scale as a pantographic beam with fixed stretch at boundaries, deforming mainly along the axial direction, e.g. with low slenderness. Such a pantographic term generalizing the grain-pair interaction could be regarded not just as accounting generically for long-range interactions, but as a term deriving from the modeling of an actual pantographic sub-structure embedded within grain–grain interactions, that could be realized by 3D printing in the context of an actual granular metamaterial (Giorgio et al., 2020b; Misra et al., 2020; De Angelo et al., 2020; Nejadsadeghi et al., 2019).

In this paper, we show through numerical examples that with the inclusion of the pantographic term mentioned above, a micro-mechanical effects on the macro damage model is that the desired thickness of the localization zone can be modeled and finely tuned successfully. Moreover, the damaged state of the body subjected to complex loading paths can also described in a systematic way. In particular, the paper is organized as follows. In Section 2, the discrete micro-mechanical model for granular systems is introduced. The target continuum is introduced as well. Then, Piola's ansatz is employed to relate the discrete with the continuum and the objective relative grain–grain displacement is defined. Exploiting Piola's ansatz, continuum deformation measures are derived from the previously-introduced objective relative grain–grain displacement. Subsequently, stiffnesses and effective damaged stiffnesses are defined following the introduction of the kinematic damage descriptors for the state of degradation of each grain–grain interaction. In Section 3 the elastic strain energy associated to each grain–grain interaction is defined. Successively, in Section 4, the dissipation, external, and total energy functionals are introduced. After that, governing equations for the damage descriptors associated to each grain–grain interaction are derived from a variational deduction procedure based on a hemi-variational principle. Section 5 reports on the numerical results obtained by making use of the presented model. Particularly, parametric analyses are carried out with respect to the averaged intergranular distance and with respect to the stiffness associated to the pantographic term by re-scaling in micromechanical parameters with the averaged intergranular distance so to keep unchanged the continuum stiffness and damage characteristics.

2. Discrete and continuous descriptions of systems with grain–grain interactions

2.1. Identification à la piola

Within the discrete description, the reference configuration of the considered set of N grains is given by positions of their centroids

$$\boldsymbol{X}_i \in E^2, \text{ with } i = 1, \dots, N,$$

where E^2 is the Euclidean two-dimensional space. The position in the present (or current) configuration $\boldsymbol{x}_i \in E^2$, at time t, is obtained through the placement function $\chi_i(t)$ as follows

$$\boldsymbol{x}_i = \chi_i(t) = \boldsymbol{X}_i + \boldsymbol{u}_i(t), \qquad i = 1, \dots, N \tag{1}$$

where $\boldsymbol{u}_i(t)$ is the displacement function of the ith grain.

Within the continuum description, a continuous body $\mathcal{B} \subset E^2$, constituted by infinitely many particles, is considered in the reference

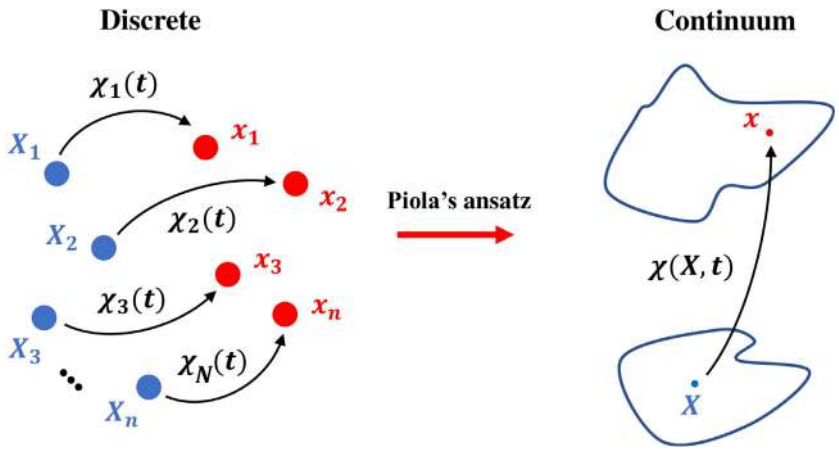

Fig. 1. Graphical representation of Piola's Ansatz in Eq. (3). Discrete kinematic descriptors introduced in Eq. (1), on the left, and continuous kinematic descriptor introduced in Eq. (2), on the right.

configuration. A generic particle occupies the position $\boldsymbol{X}$ in the reference configuration, i.e. $\boldsymbol{X} \in \mathcal{B}$. Such a particle is placed, in the present configuration at time t, into the position $\boldsymbol{x}$ through the placement function

$$\boldsymbol{x} = \chi(\boldsymbol{X}, t) = \boldsymbol{X} + \boldsymbol{u}(\boldsymbol{X}, t), \tag{2}$$

where $\boldsymbol{u}(\boldsymbol{X}, t)$ is the displacement function of the continuous body $\mathcal{B}$.

In the continuum-discrete identification, the following relationship (Piola's Ansatz, see Fig. 1) will be assumed

$$\chi(\boldsymbol{X}_i, t) = \chi_i(t), \qquad i = 1, \dots, N, \tag{3}$$

which means that the placements $\chi_i(t)$ of the N grains correspond to the placement $\chi(\boldsymbol{X}, t)$ of the continuous body $\mathcal{B}$ evaluated at those positions $\boldsymbol{X} = \boldsymbol{X}_i$, with $i = 1, \dots, N$, where the grains are located in the reference configuration.

2.2. Objective relative grain–grain displacement and continuum deformation measures

Let us now consider just a pair of grains denoted as n and p with their centroids positioned at $\boldsymbol{X}_n$ and $\boldsymbol{X}_p$, respectively. Let us also assume that the distance between them is equal to L, that is assumed to be the averaged intergranular distance. Furthermore, the unit vector$\hat{\boldsymbol{c}}$ can be defined as follows

$$\boldsymbol{X}_n - \boldsymbol{X}_p = \hat{\boldsymbol{c}} L. \tag{4}$$

Therefore, the vector quantity $\hat{\boldsymbol{c}} L$ in Eq. (4) is nothing but the arrow in the reference configuration that, once applied to the position $\boldsymbol{X}_n$, touches and points towards the position $\boldsymbol{X}_p$. In the current configuration, at time t, the positions occupied by the two grain centroids at positions $\boldsymbol{X}_n$ and $\boldsymbol{X}_p$ in the reference configuration are, respectively, $\boldsymbol{x}_n = \chi(\boldsymbol{X}_n, t)$ and $\boldsymbol{x}_p = \chi(\boldsymbol{X}_p, t)$. Analogously, the vector in Eq. (4) is transformed in the present configuration, at time t, into

$$\boldsymbol{x}_n - \boldsymbol{x}_p = \chi(\boldsymbol{X}_n, t) - \chi(\boldsymbol{X}_p, t). \tag{5}$$

Following (Timofeev et al., 2020), an objective relative displacement is defined as

$$\boldsymbol{u}^{np} = \boldsymbol{F}^T (\boldsymbol{x}_n - \boldsymbol{x}_p) - (\boldsymbol{X}_n - \boldsymbol{X}_p), \tag{6}$$

where $\boldsymbol{F} = \nabla\chi$ is the deformation gradient. Here and after ∇ means the gradient operator with respect to the position X in the reference configuration.

Let us now assume that the two grains n and p are neighboring ones. Thus, the Taylor's series expansion of the function $\chi(\boldsymbol{X}_n, t)$ centered at $\boldsymbol{X} = \boldsymbol{X}_p$ yields

$$\boldsymbol{x}_n = \chi(\boldsymbol{X}_n, t) \cong \boldsymbol{x}_p + L\boldsymbol{F}_p\hat{\boldsymbol{c}} + \frac{L^2}{2}\left[\nabla_p \boldsymbol{F}\hat{\boldsymbol{c}}\right]\cdot\hat{\boldsymbol{c}}, \tag{7}$$

where the following second and third order tensors evaluated at $\boldsymbol{X} = \boldsymbol{X}_p$ have been defined

$$\boldsymbol{F}_p = (\nabla\chi)_{\boldsymbol{X}=\boldsymbol{X}_p}, \qquad \nabla_p \boldsymbol{F} = [\nabla(\nabla\chi)]_{\boldsymbol{X}=\boldsymbol{X}_p}.$$

Let us also introduce the Green-Saint-Venant tensor $\boldsymbol{G}$ and its gradient, which are, respectively, a second and third order tensor

$$\boldsymbol{G} = \frac{1}{2}\left(\boldsymbol{F}^T\boldsymbol{F} - \boldsymbol{I}\right), \quad \nabla\boldsymbol{G} = \boldsymbol{F}^T\nabla\boldsymbol{F}. \tag{8}$$

Eqs. (7) and (8), in index notation, where superscripts denote the position at which the corresponding quantity is evaluated, read as

$$x_i^n = x_i^p + F_{ij}^p\hat{c}_j L + \frac{L^2}{2}F_{ij,h}^p\hat{c}_j\hat{c}_h, \quad G_{ij}^p = \frac{1}{2}\left(F_{ai}^p F_{aj}^p - \delta_{ij}\right), \quad G_{ij,h}^p = F_{ai}^p F_{aj,h}^p. \tag{9}$$

Thus, making use of the index notation and taking into account Eqs. (4) and (9), the objective relative displacement in Eq. (6) can be re-written as

$$u_i^{np} = 2G_{ij}^p\hat{c}_j L + \frac{L^2}{2}G_{ij,h}^p\hat{c}_j\hat{c}_h. \tag{10}$$

We remark that, owing to Eq. (10), the objective relative displacement $\boldsymbol{u}^{np}$ for a given grain–grain orientation $\hat{\boldsymbol{c}}$ is not additive inverse of that computed for the opposite grain–grain orientation, i.e. $-\hat{\boldsymbol{c}}$, when the strain gradient is non-vanishing, i.e. $\nabla\boldsymbol{G} \neq 0$, because it is not an odd function of $\hat{\boldsymbol{c}}$. This means that the strain gradient breaks the symmetry with respect to the inversion of the grain–grain orientation. Such a feature enables strain-gradient-triggered chiral effects.

The half-projection of the objective relative displacement on the unit vector $\hat{\boldsymbol{c}}$ is the so-called normal displacement u_η (a scalar quantity), while its projection on the unit vector orthogonal to $\hat{\boldsymbol{c}}$ is the so-called tangent displacement vector

$$u_\eta = \frac{1}{2}\boldsymbol{u}^{np}\cdot\hat{\boldsymbol{c}}, \quad \boldsymbol{u}_\tau = \boldsymbol{u}^{np} - (\boldsymbol{u}^{np}\cdot\hat{\boldsymbol{c}})\hat{\boldsymbol{c}}. \tag{11}$$

Such a definition for u_η have been chosen in order to have non-confusing interpretation of stiffness parameters defined in the next subsection. For the detailed justification one can see Placidi et al. (2021). Insertion of (10) into (11) yields the normal displacement, its square and the squared tangent displacements, in terms of the strain $\boldsymbol{G}$, the strain gradient $\nabla\boldsymbol{G}$, the grain–grain distance L and its orientation $\hat{\boldsymbol{c}}$

$$u_\eta = LG_{ij}\hat{c}_i\hat{c}_j + \frac{L^2}{4}G_{ij,h}\hat{c}_i\hat{c}_j\hat{c}_h, \tag{12}$$

$$u_\eta^2 = L^2\hat{c}_i\hat{c}_j\hat{c}_a\hat{c}_b G_{ij}G_{ab} + \frac{1}{2}L^3\hat{c}_i\hat{c}_j\hat{c}_a\hat{c}_b\hat{c}_c G_{ij}G_{ab,c} + \frac{1}{16}L^4\hat{c}_i\hat{c}_j\hat{c}_h\hat{c}_a\hat{c}_b\hat{c}_c G_{ij,h}G_{ab,c}, \tag{13}$$

$$u_\tau^2 = 4L^2 G_{ij} G_{ab} \left(\delta_{ia}\hat{c}_j\hat{c}_b - \hat{c}_i\hat{c}_j\hat{c}_a\hat{c}_b\right) + 2L^3 G_{ij} G_{ab,c} \left(\delta_{ia}\hat{c}_j\hat{c}_b\hat{c}_c - \hat{c}_i\hat{c}_j\hat{c}_a\hat{c}_b\hat{c}_c\right) + \frac{L^4}{4} G_{ij,h} G_{am,n} \left(\delta_{ia}\hat{c}_j\hat{c}_h\hat{c}_m\hat{c}_n - \hat{c}_i\hat{c}_j\hat{c}_h\hat{c}_a\hat{c}_b\hat{c}_c\right), \tag{14}$$

where the superscript p has been omitted to simplify the notation.

2.3. Damage descriptors and effective stiffnesses

Following the same notation employed in Timofeev et al. (2020), the damaged tangent stiffness is denoted with $k_{\tau,D}$ and the damaged normal stiffness is denoted with $k_{\eta,D}$

$$k_{\eta,D} = k_{\eta,D}^t \Theta\left(u_\eta\right) + k_{\eta,D}^c \Theta\left(-u_\eta\right), \tag{15}$$

where $k_{\eta,D}^t$ is the stiffness in tension and $k_{\eta,D}^c \gg k_{\eta,D}^t$ is the stiffness in compression. Remark that, usually, for cementitious granular materials the stiffness in compression is much higher than the stiffness in tension. Here, tension and compression are discriminated through the sign of the objective normal displacement u_η and, for this reason, we make use of the Heaviside function Θ. Damage is modeled with two variables, i.e. the normal damage D_η, and the tangent damage D_τ. The damage variables D_η and D_τ reduce linearly, respectively, the tension and compression normal damaged stiffness $k_{\eta,D}$(15) and the tangent damaged stiffness $k_{\tau,D}$. In formulas, we have

$$k_{\eta,D}^t = k_\eta^t\left(1 - D_\eta\right), \qquad k_{\eta,D}^c = k_\eta^c\left(1 - D_\eta\right), \qquad k_{\tau,D} = k_\tau\left(1 - D_\tau\right), \tag{16}$$

which means that the tangent damaged stiffness $k_{\tau,D}$ and the normal damaged stiffness $k_{\eta,D}$ are defined, respectively, through the non-damaged tangent stiffness k_τ and the non-damaged normal stiffness k_η. For the latter case, in formulas, we have $k_{\eta,D} = k_\eta\left(1 - D_\eta\right)$, where the non-damaged normal stiffness k_η has been defined in terms of the non-damaged tension normal stiffness k_η^t and the non-damaged compression normal stiffness k_η^c as

$$k_\eta = k_\eta^t \Theta\left(u_\eta\right) + k_\eta^c \Theta\left(-u_\eta\right). \tag{17}$$

We hence obtain the following synthetic expression for the damaged normal stiffness

$$k_{\eta,D} = k_\eta\left(1 - D_\eta\right) = k_\eta^t\left(1 - D_\eta\right)\Theta\left(u_\eta\right) + k_\eta^c\left(1 - D_\eta\right)\Theta\left(-u_\eta\right). \tag{18}$$

In order to smooth the constitutive assumption in Eq. (17), the Heaviside function $\Theta(x)$ is replaced in the numerical scheme by the following smooth function (see Fig. 2) (Wang and Qian, 2018)

$$\frac{1}{2} + \frac{1}{\pi}\arctan\left(\frac{x}{\alpha}\right) \tag{19}$$

so that the non-damaged normal stiffness is defined as a smooth function of the normal relative displacement

$$k_\eta = \frac{1}{2}\left(k_\eta^t + k_\eta^c\right) + \frac{1}{\pi}\left(k_\eta^t - k_\eta^c\right)\arctan\left(\frac{u_\eta}{\alpha}\right), \tag{20}$$

that in turns gives the damaged normal stiffness as a smooth function of the normal relative displacement

$$k_{\eta,D} = \frac{1}{2}\left(k_\eta^t + k_\eta^c\right)\left(1 - D_\eta\right) + \frac{1}{\pi}\left(k_\eta^t - k_\eta^c\right)\arctan\left(\frac{u_\eta}{\alpha}\right)\left(1 - D_\eta\right). \tag{21}$$

The quantity α can be tuned to modulate the regularization. Large values of α enhance the convergence of the algorithm. A value for α is considered, see Table 1, as to give a sufficiently smooth and non-stiff problem while not being detrimental to the congruence of Eqs. (17), (20) and (18), (21), so that the physical meaning of α can be overlooked.

3. Elastic strain energy

The elastic energy density per unit area is derived starting from the elastic energy associated to a single grain–grain interaction, say the couple $n - p$ considered in Section 2.2, within the discrete description. It is chosen to be additively decomposed in two parts

$$U^{tot} = U_u + U_P,$$

where the first contribution U_u follows the modeling assumption of Timofeev et al. (2020)

$$U_u = \frac{1}{2}k_{\eta,D}u_\eta^2 + \frac{1}{2}k_{\tau,D}u_\tau^2, \tag{22}$$

having intergranular interaction described by means of normal and tangential springs. It is worth to be noted that the damaged elastic stiffnesses in Eqs. $(16)_3$ and (18), which are related to those springs, can be defined as the coefficients of a quadratic form of the objective normal and tangential displacements in Eq. (22).

The second term U_P reads as

$$U_P = \frac{1}{2}K_P\left[\left(\nabla u_\eta\right)\cdot\hat{\boldsymbol{c}}\right]^2 \tag{23}$$

and it is introduced as an additional energy storage mechanism that represents long-range (beyond nearest neighbor) effects, and therefore, upon gradients of relative displacement. The normal gradient of the objective normal displacement is, neglecting second gradient of strain terms,

$$\left(\nabla u_\eta\right)\cdot\hat{\boldsymbol{c}} = LG_{ij,h}^p\hat{c}_i\hat{c}_j\hat{c}_h$$

and it leads us to the U_P formulation in terms of strain gradient components

$$U_P = \frac{1}{2}K_P\left[\left(\nabla u_\eta\right)\cdot\hat{\boldsymbol{c}}\right]^2 = \frac{1}{2}K_pL^2G_{ij,h}^pG_{ab,c}^p\hat{c}_i\hat{c}_j\hat{c}_h\hat{c}_a\hat{c}_b\hat{c}_c. \tag{24}$$

The grain–grain interaction is, therefore, no longer represented by two (normal and tangential) springs. The introduction of the term U_P allows us to account, for instance, for a non-null strain energy when the objective relative displacement $\boldsymbol{u}^{np}$ is zero for both normal u_η and tangential u_τ components. It can be seen from Fig. 3 that such a behavior resembles that of a pantograph. Thus, the introduction of U_P implies a kind of pantographic interaction mechanism and the coefficient K_P will be further referred to as the coefficient of pantographic interaction (or the pantographic coefficient).

In the discrete description, the total energy U^{tot} associated to the interaction of a given grain, whose centroid occupies the position $\boldsymbol{X}_p$ in the reference configuration, with neighboring grains is given by the summation of the energy in Eq. (22) for all the $N - 1$ possible interactions

$$U^{tot} = \sum_{i=1}^{N-1} U_i = \sum_{i=1}^{N-1}\left(U_{u,i} + U_{P,i}\right) = \sum_{i=1}^{N-1}\left(\frac{1}{2}k_{\eta,D,i}u_{\eta,i}^2 + \frac{1}{2}k_{\tau,D,i}u_{\tau,i}^2 + \frac{1}{2}K_{P,i}\left[\left(\nabla u_{\eta,i}\right)\cdot\hat{\boldsymbol{c}}_i\right]^2\right), \tag{25}$$

where the subscript i refers to a generic couple $n{-}p$ of grains. In Eq. (25) it is therefore intended that $k_{\eta,D,i}$ and $k_{\tau,D,i}$ are the damaged stiffnesses, respectively normal and tangent, associated to the interaction of the ith couple of grains, while $u_{\eta,i}^2$ and $u_{\tau,i}^2$ are the squared elastic relative displacements, respectively normal and tangent, of the ith couple of grains. By $\left[\left(\nabla u_{\eta,i}\right)\cdot\hat{\boldsymbol{c}}_i\right]^2$ we denoted the squared normal gradient of objective normal displacement of the ith couple of grains.

It is worth to mention here that the pantographic coefficients $K_{P,i}$ are not affected by damage growth, in contrast to other stiffnesses in Eq. (25), so the term U_P remains finite during the evolution of the system.

Continualization of Eq. (25) is performed by using the following homogenization rule (see Fig. 4). Let a be a generic quantity defined within the discrete description, such that a_i refers to the grain–grain

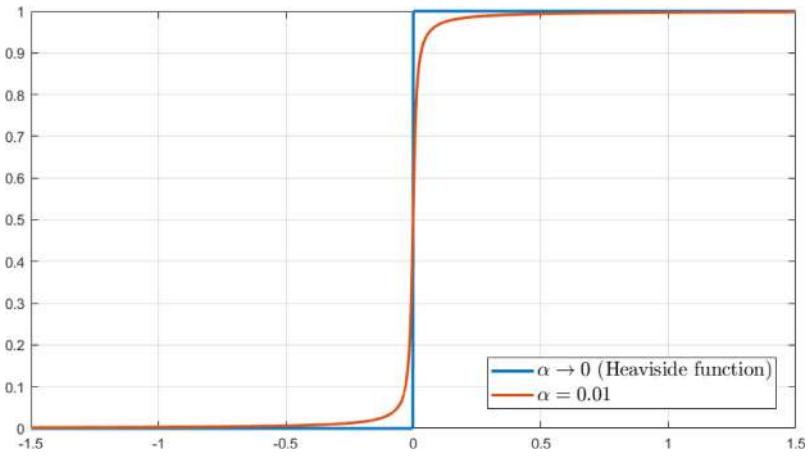

Fig. 2. Plot for Eq. (19). In the limit of α going to zero the smooth function in (19) goes to the Heaviside function.

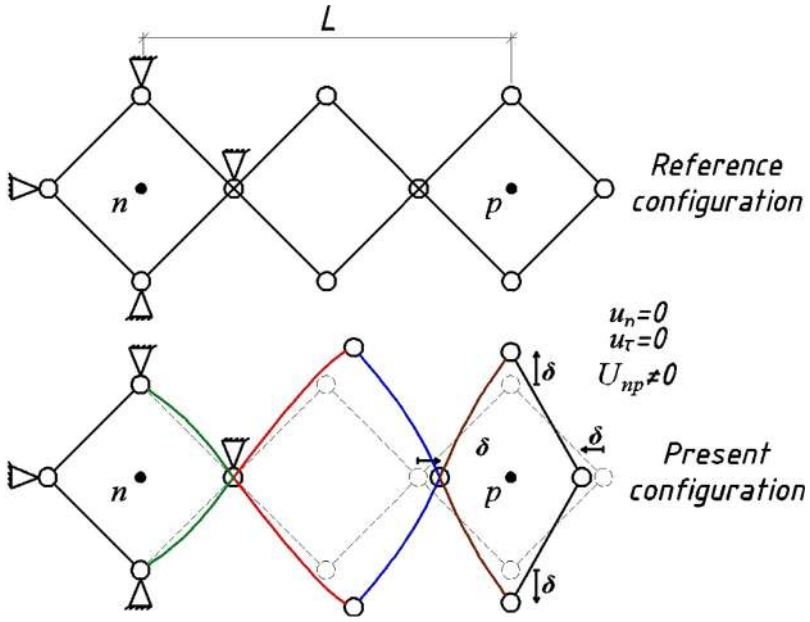

Fig. 3. Representation of the pantographic mechanism.

interaction, identified with the index i, between a generic grain n and a generic grain p. Let $a(\theta)$ be the continuous distribution of the quantity a over the orientation θ of the grain-pair formed by grain n and its neighboring grains. We have that, when the number N of grains within the discrete system tends to infinite, the following limit holds

$$\sum_{i=1}^{N}\left[a_i\right] \quad \longrightarrow \quad \int_{S^1} a(\theta), \tag{26}$$

where $S^1=[0,2\pi]$ is the unit circle, namely the domain of the function $a(\theta)$, i.e. the set of all orientations. Remark that $a_i = a\left(\theta_i\right)$, where θ_i is the orientation of the grain-pair formed by grain n and grain p, namely the orientation of the unit vector $\hat{c}$. The application of the homogenization rule in Eq. (26) to the total energy U^{tot} in Eq. (25) gives

$$\begin{aligned} U^{tot} \quad \longrightarrow \quad U &= \int_{S^1} \frac{1}{2}k_\eta\left(1-D_\eta\right)u_\eta^2+\frac{1}{2}k_\tau\left(1-D_\tau\right)u_\tau^2, \\ &+\frac{1}{2}K_P\left[\left(\nabla u_\eta\right)\cdot\hat{c}\right]^2, \end{aligned} \tag{27}$$

where $k_\eta=\widetilde{k}_\eta(\theta)$, $k_\tau=\widetilde{k}_\tau(\theta)$, $K_P=\widetilde{K}_P(\theta)$, $D_\eta=\widetilde{D}_\eta(\theta)$, and $D_\tau=\widetilde{D}_\tau(\theta)$ replace, respectively, $k_{\eta,i}$, $k_{\tau,i}$, $K_{P,i}$, $D_{\eta,i}$, and $D_{\tau,i}$. Remark that these quantities are all functions of the orientation $\theta\in[0,2\pi]$ of the generic grain-pair formed by grain n and its neighboring grains, namely

$$k_{\eta,i}\to\widetilde{k}_\eta(\theta), \quad k_{\tau,i}\to\widetilde{k}_\tau(\theta), \quad K_{p,i}\to\widetilde{K}_p(\theta) \quad D_{\eta,i}\to\widetilde{D}_\eta(\theta), \quad D_{\tau,i}\to\widetilde{D}_\tau(\theta).$$

From Eqs. (13) and (14) the continuum elastic strain energy density per unit area in Eq. (27) reads as

$$\begin{aligned} U = &\int_{S^1}\frac{1}{2}k_\eta\left(1-D_\eta\right)\left(L^2\hat{c}_i\hat{c}_j\hat{c}_a\hat{c}_bG_{ij}G_{ab}+\frac{1}{2}L^3\hat{c}_i\hat{c}_j\hat{c}_a\hat{c}_b\hat{c}_cG_{ij}G_{ab,c}\right) \\ &+\int_{S^1}\frac{1}{2}k_\eta\left(1-D_\eta\right)\left(\frac{1}{16}L^4\hat{c}_i\hat{c}_j\hat{c}_h\hat{c}_a\hat{c}_b\hat{c}_cG_{ij,h}G_{ab,c}\right) \\ &+\int_{S^1}\frac{1}{2}k_\tau\left(1-D_\tau\right)\left(4L^2G_{ij}G_{ab}\left(\delta_{ia}\hat{c}_j\hat{c}_b-\hat{c}_i\hat{c}_j\hat{c}_a\hat{c}_b\right)\right. \\ &\left.+2L^3G_{ij}G_{ab,c}\left(\delta_{ia}\hat{c}_j\hat{c}_b\hat{c}_c-\hat{c}_i\hat{c}_j\hat{c}_a\hat{c}_b\hat{c}_c\right)\right) \\ &+\int_{S^1}\frac{1}{2}k_\tau\left(1-D_\tau\right)\left(\frac{1}{4}L^4G_{ij,h}G_{am,n}\left(\delta_{ia}\hat{c}_j\hat{c}_h\hat{c}_m\hat{c}_n-\hat{c}_i\hat{c}_j\hat{c}_h\hat{c}_a\hat{c}_b\hat{c}_c\right)\right) \\ &+\int_{S^1}\frac{1}{2}K_PL^2G_{ij,h}G_{ab,c}\hat{c}_i\hat{c}_j\hat{c}_h\hat{c}_a\hat{c}_b\hat{c}_c. \end{aligned} \tag{28}$$

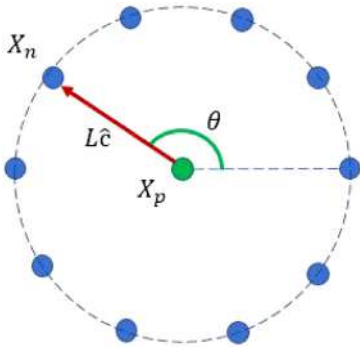

Fig. 4. Graphic representation of the homogenization rule.

The previous expression can be re-written in a more compact form as

$$U = \frac{1}{2}\mathbb{C}_{ijab}G_{ij}G_{ab} + \mathbb{M}_{ijabc}G_{ij}G_{ab,c} + \frac{1}{2}\mathbb{D}_{ijhabc}G_{ij,h}G_{ab,c}, \tag{29}$$

where, accounting for the symmetrization induced by the symmetry of the strain tensor $\boldsymbol{G}$, the elastic stiffnesses $\mathbb{C}$, $\mathbb{M}$, $\mathbb{D}$ are identified as follows

$$\mathbb{C}_{ijab} = L^2\int_{S^1} k_\eta\left(1-D_\eta\right)\hat{c}_i\hat{c}_j\hat{c}_a\hat{c}_b \tag{30}$$
$$+L^2\int_{S^1} k_\tau\left(1-D_\tau\right)\left(\left(\delta_{ia}\hat{c}_j\hat{c}_b+\delta_{ib}\hat{c}_j\hat{c}_a+\delta_{ja}\hat{c}_i\hat{c}_b+\delta_{jb}\hat{c}_i\hat{c}_a\right)-4\hat{c}_i\hat{c}_j\hat{c}_a\hat{c}_b\right)$$

$$\mathbb{M}_{ijabc} = \frac{1}{4}L^3\int_{S^1} k_\eta\left(1-D_\eta\right)\hat{c}_i\hat{c}_j\hat{c}_a\hat{c}_b\hat{c}_c \tag{31}$$
$$\frac{1}{4}L^3\int_{S^1} k_\tau\left(1-D_\tau\right)\left(\left(\delta_{ia}\hat{c}_j\hat{c}_b+\delta_{ib}\hat{c}_j\hat{c}_a+\delta_{ja}\hat{c}_i\hat{c}_b+\delta_{jb}\hat{c}_i\hat{c}_a\right)\hat{c}_c - 4\hat{c}_i\hat{c}_j\hat{c}_a\hat{c}_b\hat{c}_c\right)$$

$$\mathbb{D}_{ijhabc} = \frac{1}{16}L^4\int_{S^1} k_\eta\left(1-D_\eta\right)\hat{c}_i\hat{c}_j\hat{c}_h\hat{c}_a\hat{c}_b\hat{c}_c \tag{32}$$
$$+\frac{1}{16}L^4\int_{S^1} k_\tau\left(1-D_\tau\right)\left(\left(\delta_{ia}\hat{c}_j\hat{c}_b+\delta_{ib}\hat{c}_j\hat{c}_a+\delta_{ja}\hat{c}_i\hat{c}_b+\delta_{jb}\hat{c}_i\hat{c}_a\right)\hat{c}_h\hat{c}_c - 4\hat{c}_i\hat{c}_j\hat{c}_h\hat{c}_a\hat{c}_b\hat{c}_c\right)$$
$$+L^2K_P\int_{S^1}\hat{c}_i\hat{c}_j\hat{c}_h\hat{c}_a\hat{c}_b\hat{c}_c$$

From Eqs. (30)–(32) one can see the presence of the pantographic coefficient K_P only in the expression for the six-rank elastic stiffness tensor $\mathbb{D}$. Therefore, since neither D_η nor D_τ affects K_P, we can notice that all of the components of the elastic tensors $\mathbb{C}$ and $\mathbb{M}$ tend to zero because of damage growth, but for the elastic tensor $\mathbb{D}$ it is not true. Hence, there is always some portion of elastic energy stored at every material point of the continuum even if we assume the damage variables reaching their maximum values.

Let us finally remark that, from the nontrivial expression in Eq. (31) for the stiffness $\mathbb{M}$, it is not odd with respect to grain-pair's orientation. Thus, it is deduced that the occurrence of damage, induce the emergence of chiral effects. Note that, indeed, in the integral (31), the unit vector $\hat{c}$ appears an odd number of times, while the domain is symmetric with respect to zero. Thus, while initially we have $\mathbb{M} = \mathbf{0}$ the evolution of damage variables D_η and D_τ, induces the emergence of chiral effects characterized by the conditions $\mathbb{M} \neq \mathbf{0}$.

4. Evolution of damage descriptors

4.1. Definition of the fundamental kinematical quantities

We evaluate the evolution of damage variables via an hemi-variational derivation of the grain interaction, that is considered for a given orientation. To do this, we start by the definition of the following 4 (3 scalar and one vector) fundamental kinematical quantities

$$u_\eta, \boldsymbol{u}_\tau, D_\eta, D_\tau, \tag{33}$$

where u_η, $\boldsymbol{u}_\tau$, D_η and D_τ have been already defined in Eqs. (11) and (16).

4.2. Definition of the dissipation, external and total energy functionals

The dissipation energy W_D is the energy dissipated because of irreversible phenomena, which is damage in our case. It can be additively decomposed into normal, i.e. W_D^η, and tangent, i.e. W_D^τ, parts

$$W_D = W_D^\eta + W_D^\tau. \tag{34}$$

The normal contribution W_D^η to the damage dissipation energy is defined as follows

$$W_D^\eta = \frac{1}{2}k_\eta^c\left(B_\eta^c\right)^2\Theta\left(-u_\eta\right)\left[-D_\eta+\frac{2}{\pi}\tan\left(\frac{\pi}{2}D_\eta\right)\right]+ \tag{35}$$
$$\frac{1}{2}k_\eta^t\left(B_\eta^t\right)^2\Theta\left(u_\eta\right)\left[2+\left(D_\eta-1\right)\left(2-2\log\left(1-D_\eta\right)+\left(\log\left(1-D_\eta\right)\right)^2\right)\right],$$

where B_η^c and B_η^t are two characteristic lengths associated to normal damage dissipation in compression and in tension, respectively. We observe that usually, for cementitious materials, we have $B_\eta^t \ll B_\eta^c$. Indeed, a much smaller amount of elastic relative displacement is needed in tension to activate damage mechanisms. The tangent contribution W_D^τ to the damage dissipation energy is defined as follows

$$W_D^\tau = \frac{1}{2}k_\tau\left[\widetilde{B}_\tau\left(u_\eta\right)\right]^2\left[2+\left(D_\tau-1\right)\left(2-2\log\left(1-D_\tau\right)+\left(\log\left(1-D_\tau\right)\right)^2\right)\right], \tag{36}$$

where $B_\tau = \widetilde{B}_\tau\left(u_\eta\right)$ is the characteristic length associated to tangent damage dissipation. Such a characteristic length is assumed to depend the normal relative grain–grain displacement, as in Misra and Poorsolhjouy (2015) and Misra and Singh (2015). Additionally, differently from Misra and Poorsolhjouy (2015) and Misra and Singh (2015) and for the sake of simplicity, the effect of the mean stress has been neglected. Following said references, the functional dependence $\widetilde{B}_\tau\left(u_\eta\right)$ has been chosen as follows

$$B_\tau = \widetilde{B}_\tau\left(u_\eta\right) = \begin{cases} B_{\tau 0} & \text{if } u_\eta \geq 0 \\ B_{\tau 0} - \alpha_2 u_\eta & \text{if } \frac{1-\alpha_1}{\alpha_2}B_{\tau 0} \leq u_\eta < 0 \\ \alpha_1 B_{\tau 0} & \text{if } u_\eta < B_{\tau 0}\frac{1-\alpha_1}{\alpha_2}, \end{cases} \tag{37}$$

where $B_{\tau 0}$ (B_{w0} in Misra and Poorsolhjouy (2015) and Misra and Singh (2015)), α_1 and α_2 are further constitutive parameters needed to express the functional dependence $\widetilde{B}_\tau\left(u_\eta^{el}\right)$. Such a functional dependence couples the two addends W_D^η and W_D^τ of the decomposition (34).

In conclusion, because of Eqs. (34), (35), (36), the dissipation energy functional (34) reads as

$$W = W_D^\eta + W_D^\tau \tag{38}$$
$$= \frac{1}{2}k_\eta^c\Theta\left(-u_\eta^{el}\right)B_c^2\left[-D_\eta+\tan\left(D_\eta\right)\right]$$
$$+\frac{1}{2}k_\eta^t\Theta\left(u_\eta^{el}\right)B_t^2\left[2+\left(D_\eta-1\right)\left(2-2\log\left(1-D_\eta\right)+\left(\log\left(1-D_\eta\right)\right)^2\right)\right]$$
$$+\frac{1}{2}k_\tau B_\tau^2\left[2+\left(D_\tau-1\right)\left(2-2\log\left(1-D_\tau\right)+\left(\log\left(1-D_\tau\right)\right)^2\right)\right]$$

Within the considered approach, the external world can exert forces expending power both on the scalar normal objective relative displacement u_η and on the vector tangent objective relative displacement $\boldsymbol{u}_\tau$, so that the external energy functional is

$$U^{ext} = F_\eta^{ext}u_\eta + F_\tau^{ext}\cdot\boldsymbol{u}_\tau, \tag{39}$$

where F_η^{ext} and F_τ^{ext} are, respectively, the external normal and tangent forces. Since we are neglecting kinetic energy and considering quasi-static evolution, the energy functional $\mathcal{E}$ reads as

$$\mathcal{E} = U + W - U^{ext}. \tag{40}$$

Remark that it is a functional of the fundamental kinematical quantities (33), namely

$$\mathcal{E} = \mathcal{E}\left(u_\eta, \boldsymbol{u}_\tau, D_\eta, D_\tau\right). \tag{41}$$

4.3. Formulation of the hemi-variational principle

The variational inequality principle can be here applied similarly to what has been done in Timofeev et al. (2020). We introduce a monotonously increasing time sequence $T_i \in \{T_i\}_{i=0,\dots,M}$ with $T_i \in \mathbb{R}$ and $M \in \mathbb{N}$. An initial datum on each of the fundamental kinematic quantities must be given for $i = 0$, i.e. for time T_0. A motion is defined as a family of displacements $\zeta = \left(u_\eta, \boldsymbol{u}_\tau\right)$ defined for each time $t = T_0, T_1, \dots, T_M$. The set AM_t is defined as the set of kinematically admissible displacements for a given time t — we require $\left(u_\eta, \boldsymbol{u}_\tau\right) \in AM_t$ — and the set AV_t is defined as the corresponding space of kinematically admissible variations — i.e. $\upsilon = \left(\delta u_\eta, \delta \boldsymbol{u}_\tau\right) \in AV_t$. Admissible variations β of the irreversible kinematic quantities $\left(D_\eta, D_\tau\right)$ must be positive, namely

$$\beta = \delta D_\eta, \delta D_\tau \in \mathbb{R}^+ \times \mathbb{R}^+. \tag{42}$$

The first variation $\delta\mathcal{E}$ of the energy functional (41) is defined as

$$\delta\mathcal{E} = \mathcal{E}\left(u_\eta + \delta u_\eta, \boldsymbol{u}_\tau + \delta \boldsymbol{u}_\tau, D_\eta + \delta D_\eta, D_\tau + \delta D_\tau\right) - \mathcal{E}\left(u_\eta, \boldsymbol{u}_\tau, D_\eta, D_\tau\right). \tag{43}$$

The increment of the fundamental kinematic quantities (33) at $t = T_i$ is given by the difference between these quantities as evaluated at times $t = T_i$ and $t = T_{i-1}$, namely

$$\left(\Delta u_\eta, \Delta \boldsymbol{u}_\tau, \Delta D_\eta, \Delta D_\tau\right)_{T_i} = \left(u_\eta, \boldsymbol{u}_\tau, D_\eta, D_\tau\right)_{T_i} - \left(u_\eta, \boldsymbol{u}_\tau, D_\eta, D_\tau\right)_{T_{i-1}}.$$

The same definition is utilized for the increment $\Delta\mathcal{E}$ of the energy functional

$$\Delta\mathcal{E} = \mathcal{E}\left(u_\eta + \Delta u_\eta, \boldsymbol{u}_\tau + \Delta \boldsymbol{u}_\tau, D_\eta + \Delta D_\eta, D_\tau + \Delta D_\tau\right) - \mathcal{E}\left(u_\eta, \boldsymbol{u}_\tau, D_\eta, D_\tau\right). \tag{44}$$

Finally, the hemi-variational principle is formulated as follows

$$\Delta\mathcal{E} \le \delta\mathcal{E} \quad \forall \upsilon = \left(\delta u_\eta, \delta \boldsymbol{u}_\tau\right) \in AV_t, \qquad \forall \beta = \left(\delta D_\eta, \delta D_\tau\right) \in \mathbb{R}^+ \times \mathbb{R}^+. \tag{45}$$

4.4. Derivation of the Euler–Lagrange equations

The variational inequality (45) must be exploited following the same procedure described in Timofeev et al. (2020), which will thus be omitted here. The results of such a procedure are the following two Euler–Lagrange equations,

$$\left\{-k_\eta\left(1 - D_\eta\right) u_\eta - k_\tau B_\tau \frac{\partial \widetilde{B}_\tau}{\partial u_\eta} \int_0^{D_\tau} \left[\log\left(1 - x\right)\right]^2 dx + F_\eta^{ext} + K_p\left\{\left[\nabla\left(\nabla u_\eta\right)\right] \hat{\boldsymbol{c}} \cdot \hat{\boldsymbol{c}}\right\}\right\}\left(\delta u_\eta\right) = 0$$

$$\left\{-k_\tau\left(1 - D_\tau\right) \boldsymbol{u}_\tau + F_\tau^{ext}\right\}\left(\delta \boldsymbol{u}_\tau\right) = 0$$

where x is an internal integration variable that is used only to avoid to write the analytical form of the integral, together with the two Karush–Kuhn–Tucker (KKT) conditions for damage variables (already derived in Timofeev et al. (2020))

$$\left[\left(u_\eta\right)^2 - \Theta\left(u_\eta\right) B_t^2 \left(\log\left(1 - D_\eta\right)\right)^2 - \Theta\left(-u_\eta\right) B_c^2 \left[\tan\left(D_\eta\right)\right]^2\right]\Delta D_\eta = 0, \tag{46}$$

$$\left[\left(\boldsymbol{u}_\tau\right)^2 - \left[B_\tau\right]^2 \left(\log\left(1 - D_\tau\right)\right)^2\right] \Delta D_\tau = 0, \tag{47}$$

The two KKT conditions (46), (47) for irreversible descriptors can be arranged in a more compact form a

$$\left\{D_\eta - \tilde{D}_\eta(u_\eta)\right\} \Delta D_\eta = 0 \tag{48}$$

$$\left\{D_\tau - \tilde{D}_\tau(\boldsymbol{u}_\tau)\right\} \Delta D_\tau = 0 \tag{49}$$

where the auxiliary threshold functions $\tilde{D}_\eta(u_\eta)$ and $\tilde{D}_\tau(\boldsymbol{u}_\tau)$ have been defined as follows

$$\tilde{D}_\eta(u_\eta) = \begin{cases} 1 - \exp\left(-\frac{u_\eta}{B_\eta^t}\right), & u_\eta > 0, \\ \frac{2}{\pi} \arctan\left(-\frac{u_\eta}{B_\eta^c}\right), & u_\eta < 0, \end{cases} \tag{50}$$

$$\tilde{D}_\tau(\boldsymbol{u}_\tau) = 1 - \exp\left(-\frac{\left|\boldsymbol{u}_\tau\right|}{B_\tau}\right), \tag{51}$$

5. Numerical results

5.1. Description of the numerical experiments

In the current section, we present numerical simulations to show the capabilities of the derived model to describe initiation and growth of damage localization zones. Following Timofeev et al. (2020) we consider 2D square specimen with a circular flaw (hole). Here $S = 10$ cm is the size of the sample and $R_h = 0.12 \cdot S$ is the hole's radius. In this work, two types of numerical experiments are employed:

1. In type 1, the specimen is subjected to tensile loading to demonstrate the effects of pantographic mechanism on the evolution and thickness of damage localization from the circular flaw. Fig. 5 (left) illustrates this loading type where we have imposed displacement $\bar{u}$ which is increasing monotonically during the tests within the range $[0, \bar{u}_{max}]$on the right-hand vertical boundary. Two cases of simulations are performed. One in which the averaged intergranular distance L is kept unchanged while the pantographic coefficient K_P is changed resulting in a change in the overall stiffness/strength of the specimen. And the second, in which the inter-granular stiffness are re-scaled for different averaged intergranular distance L, such that the overall stiffness/strength of the specimen remains unchanged while both the averaged intergranular distance L and the pantographic coefficient K_P are varied.
2. In type 2, the specimen is subjected to a more complex loading path by sequentially applying tensile and shear loading, as it is sketched in Fig. 5 (right), to demonstrate the effects of loading-path on the evolution and thickness of damage localization from the circular flaw. For all of the four boundaries of the specimen we apply two conditions, i.e.

$$\begin{cases} u_1 &= \tilde{u}_1(x, y) = \bar{u}_1 \cdot (x/S) \\ u_2 &= \tilde{u}_2(x, y) = \bar{u}_2 \cdot (x/S) \end{cases} \quad \forall (x, y) \in [0, S] \times [0, S] \tag{52}$$

where u_1 and u_2 are horizontal and vertical components of the displacement field $\boldsymbol{u}$. Eq. (52) implies that the left-hand side of the sample is blocked both for horizontal u_1 and for vertical u_2 displacements

$$u_1 = \tilde{u}_1(0, y) = 0$$
$$u_2 = \tilde{u}_2(0, y) = 0$$

since $x = 0$ in this case, whereas on the right-hand side we have imposed displacements

$$u_1 = \tilde{u}_1(S, y) = \bar{u}_1$$
$$u_2 = \tilde{u}_2(S, y) = \bar{u}_2.$$

At the top as well as at the bottom imposed displacement for each point of the boundary increases with horizontal coordinate $x \in [0, S]$. Both horizontal and vertical imposed displacements are monotonically increasing within the ranges $[0, \bar{u}_1^{max}]$ and $[0, \bar{u}_2^{max}]$ respectively. We consider two cases of simulations to describe path-dependency of the system evolution for the derived model. One case in which the simulation starts with tensile

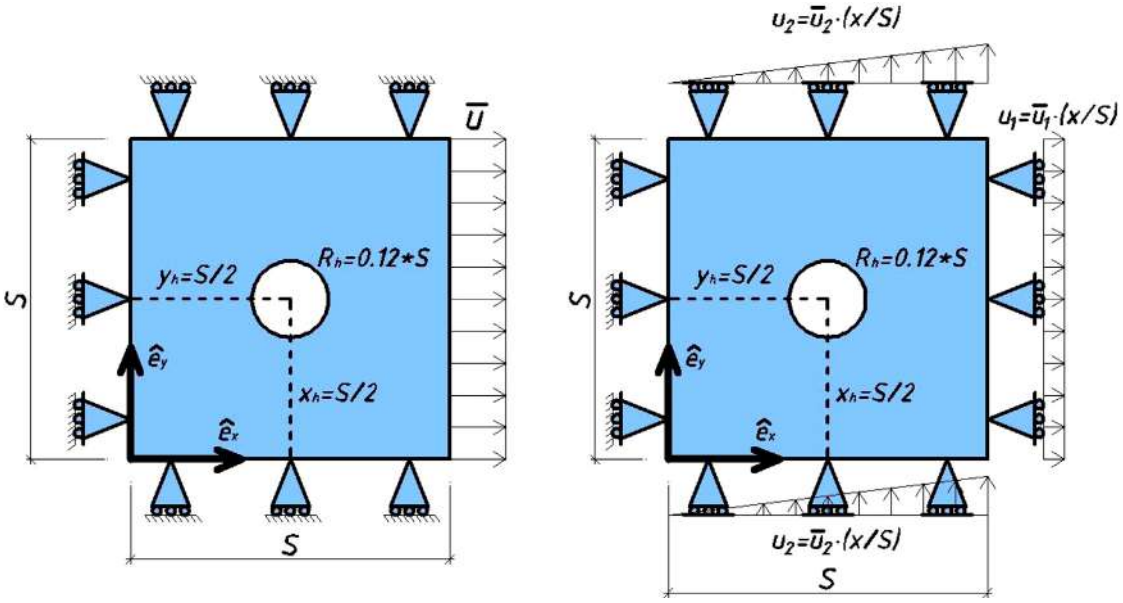

Fig. 5. Schematics of analyzed domains and considered boundary conditions.

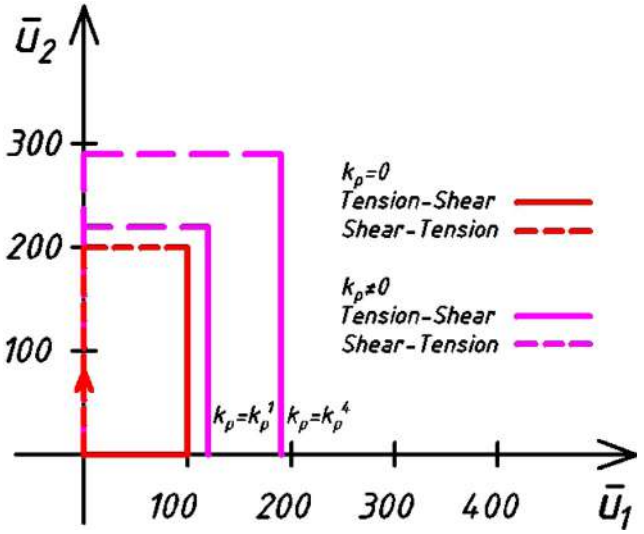

Fig. 6. Graphic representation of the loading path with respect to number of loading steps.

loading, increasing $\bar{u}_1$ while keeping $\bar{u}_2$ null, and then switch to shear loading, increasing $\bar{u}_2$ keeping $\bar{u}_1$ unchanged, such that the specimen in first subjected to tensile loading followed by shear loading. In the second case, we first apply shear loading and then switch to tensile loading, such that the final deformed external shape of the specimen remains the same. For both of these cases, we keep the averaged intergranular distance L unchanged while the pantographic coefficient K_P is changed resulting in a change in the overall stiffness/strength of the specimen. The loading paths for the two cases are represented graphically in Fig. 6 for pantographic coefficient $K_P = 0$, $K_P = K_P^1$ and $K_P = K_P^4$. In Fig. 6, the axis refer to the number of loading steps highlighted later in the Table 4.

5.2. Re-scaling with the averaged intergranular distance

In this Sub-section we consider a class of materials with the same stiffness and damage characteristics but different averaged intergranular distance L. To do this, we introduce a re-scaling parameter $\gamma \in \mathbb{R}^+$ for changing the averaged intergranular distance from L to L^* as follows:

$$L^* = \frac{L}{\gamma}. \tag{53}$$

Such re-scaling should therefore correspond to materials with similar elastic and damage behavior. Thus, in particular the consequence is (i) an identical 4th rank elasticity tensor $\mathbb{C}^*$, i.e.,

$$\mathbb{C}^* = \mathbb{C}$$

and from Eq. (30) we deduce the following re-scaling rule for intergranular stiffness,

$$\begin{cases} \left(k_\eta^t\right)^* (L^*)^2 = k_\eta^t L^2 \\ \left(k_\eta^c\right)^* (L^*)^2 = k_\eta^c L^2 \\ \left(k_\tau\right)^* (L^*)^2 = k_\tau L^2, \end{cases} \quad \rightarrow \quad \begin{cases} \left(k_\eta^t\right)^* = \gamma^2 k_\eta^t \\ \left(k_\eta^c\right)^* = \gamma^2 k_\eta^c \\ k_\tau^* = \gamma^2 k_\tau, \end{cases} \tag{54}$$

and (ii) similar damage characteristic lengths. To do this we recall the expressions of the auxiliary threshold functions in Eqs. (50), (51) and consider

$$\begin{cases} \frac{u_\eta^*}{(B_\eta^c)^*} = \frac{u_\eta}{B_\eta^c} \\ \frac{u_\eta^*}{(B_\eta^t)^*} = \frac{u_\eta}{B_\eta^t} \\ \frac{|u_\tau^*|}{B_\tau^*} = \frac{|u_\tau|}{B_\tau}, \end{cases} \quad \rightarrow \quad \begin{cases} \left(B_\eta^t\right)^* = \frac{B_\eta^t}{\gamma} \\ \left(B_\eta^c\right)^* = \frac{B_\eta^c}{\gamma} \\ B_{\tau 0}^* = \frac{B_{\tau 0}}{\gamma}, \end{cases} \tag{55}$$

where the definitions (12) and (14) of normal and tangent displacement have been used to deduce the following approximations for their order of magnitudes,

$$u_A^* \cong \frac{L^*}{L} u_A = \frac{u_A}{\gamma}, \quad A = \eta, \tau. \tag{56}$$

For the same reason and taking into account Eq. (20), the regularizing parameter α, the one used to smooth the constitutive assumption on

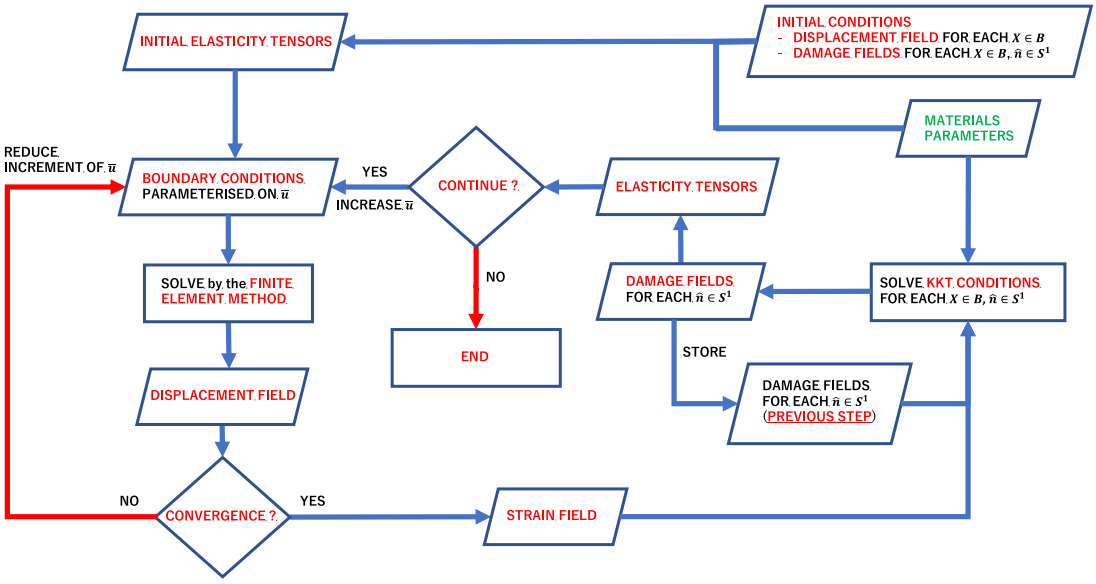

Fig. 7. Flowchart of the numerical iterative procedure used to solve the mathematical formulation.

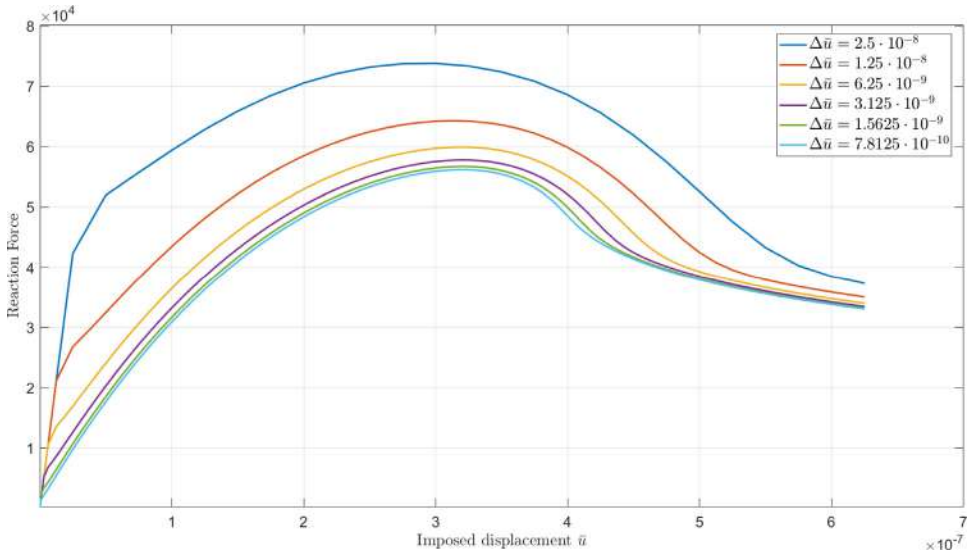

Fig. 8. Convergence analysis with respect to the size of the load step $\Delta\bar{u}$. Global elastic response, i.e. total reaction force vs prescribed displacement for the pantographic coefficient $K_P = K_P^3$.

tension–compression asymmetry in Eq. (21), for the sake of numerical accuracy has been re-scaled as follows,

$$\frac{u_\eta^*}{\alpha^*} = \frac{u_\eta}{\alpha}, \quad \rightarrow \quad \alpha^* = \frac{\alpha}{\gamma}. \tag{57}$$

It is worth to be noted that, as a consequence of the re-scalings assumed in (53), (54), (55) and (57) on the one hand the 5th rank elasticity tensor $\mathbb{M}$ will be re-scaled as follows

$$\mathbb{M}^* = \frac{(L^*)^3}{L^3}\frac{\left(k_\eta^t\right)^*}{k_\eta^t}\mathbb{M} = \frac{1}{\gamma^3}\gamma^2\mathbb{M} = \frac{\mathbb{M}}{\gamma}, \tag{58}$$

and, on the other hand, in order to derive the re-scaling rule for the 6th rank elasticity tensor $\mathbb{D}$, we need to prescribe a re-scaling rule also for the pantographic coefficient K_P. To do this we consider first the case of no pantographic coefficient and derive,

$$K_P = 0, \quad \rightarrow \quad \mathbb{D}^* = \frac{(L^*)^4}{L^4}\frac{\left(k_\eta^t\right)^*}{k_\eta^t}\mathbb{D} = \frac{1}{\gamma^4}\gamma^2\mathbb{D} = \frac{\mathbb{D}}{\gamma^2}. \tag{59}$$

In this case we remark that in the limit of zero averaged intergranular distance $L \rightarrow 0$ (i.e. from (53) in the limit $\gamma \rightarrow \infty$) we derive, from (58) and (59), that $\mathbb{M}^* \rightarrow \mathbf{0}$ and $\mathbb{D}^* \rightarrow \mathbf{0}$, i.e. a situation with no strain gradient effects and therefore vanishingly thin boundary layers in the numerical simulations. However, the presence of the pantographic term changes this undesired effect by ensuring that in this limit the 6th rank elasticity tensor may be the same, i.e.,

$$\lim_{\gamma\rightarrow\infty} \mathbb{D}^* = \mathbb{D} \quad \rightarrow \quad \left(L^*\right)^2 K_P^* = L^2 K_P \quad \rightarrow \quad K_P^* = \gamma^2 K_P,$$

that is, by employing the same re-scaling rules as that for the other stiffness coefficients given in (54).

5.3. Constitutive coefficients setting

For illustration, we will consider three sets of material parameters, namely the sets $\mathcal{P}_1$, $\mathcal{P}_2$ and $\mathcal{P}_3$ that are defined respectively by assuming $\gamma = 1$, $\gamma = 2$ and $\gamma = 5$ according to Tables 1–2, such as to consider a wide range of intergranular distance.

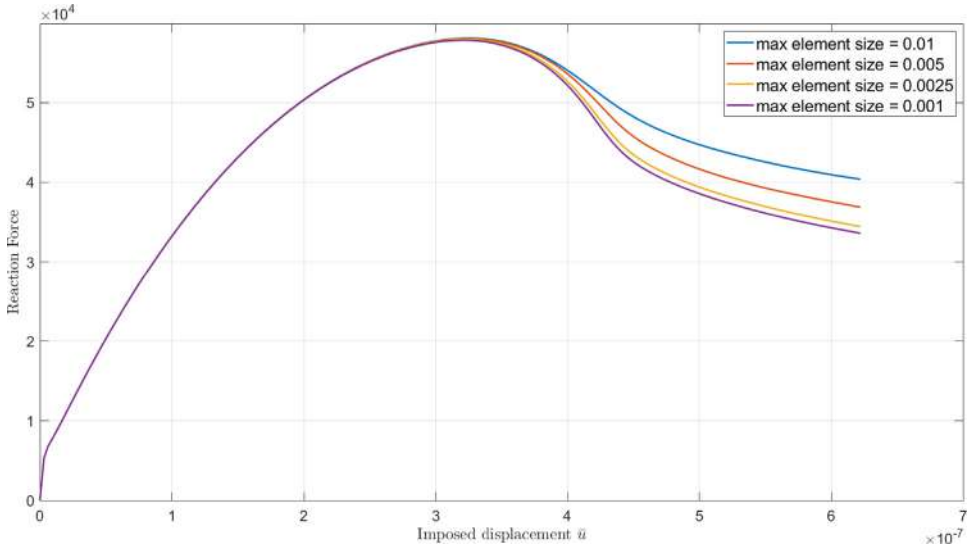

Fig. 9. Mesh-convergence analysis. Global elastic response, i.e. total reaction force vs prescribed displacement for the pantographic coefficient $K_P = K_P^3$.

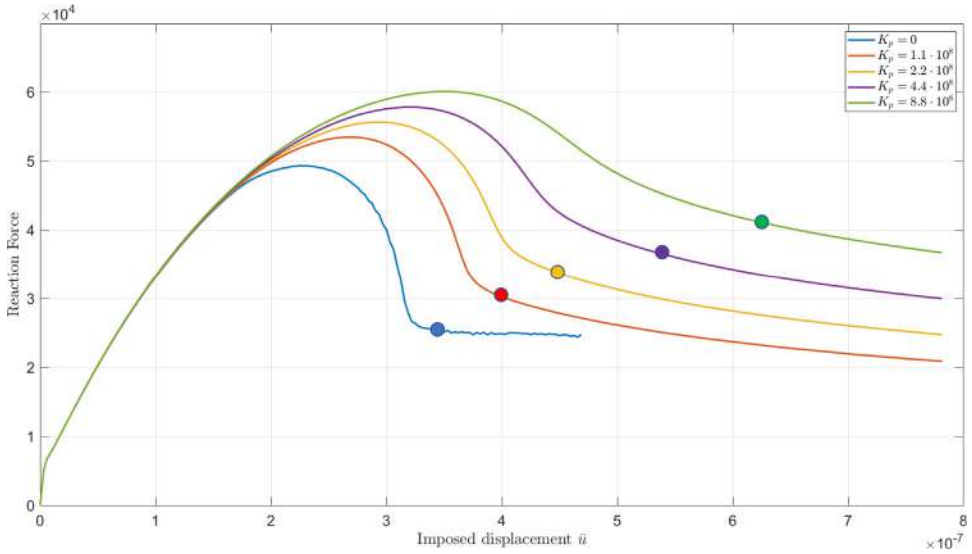

Fig. 10. Force versus displacement diagram for the $\mathcal{P}_1$ set of parameters defined in Tables 1–2 and for different values of K_P. Circle markers indicate approximately the time step, when the crack reaches the boundary of the sample.

Table 1
Values of constitutive parameters used in numerical tests.

	γ	L [m]	k_η^c [J/m^4]	k_η^t [J/m^4]	k_τ [J/m^4]	B_η^c [m]	B_η^t [m]	B_τ [m]	α_1[1]	α_2[1]	α[1]
$\mathcal{P}_1$	1	0.01	$1.4 \cdot 10^{15}$	$1.4 \cdot 10^{14}$	$3 \cdot 10^{13}$	$1.5 \cdot 10^{-7}$	$3.5 \cdot 10^{-8}$	$5 \cdot 10^{-8}$			$3 \cdot 10^{-10}$
$\mathcal{P}_2$	2	0.005	$5.6 \cdot 10^{15}$	$5.6 \cdot 10^{14}$	$1.2 \cdot 10^{14}$	$7.5 \cdot 10^{-8}$	$1.75 \cdot 10^{-8}$	$2.5 \cdot 10^{-8}$	10	14	$1.5 \cdot 10^{-10}$
$\mathcal{P}_3$	5	0.002	$35 \cdot 10^{15}$	$35 \cdot 10^{14}$	$7.5 \cdot 10^{14}$	$3 \cdot 10^{-8}$	$7 \cdot 10^{-9}$	$1 \cdot 10^{-8}$			$75 \cdot 10^{-11}$

Moreover, the values of the pantographic coefficients have been selected by comparing the first and the third row of (32) with the following rule,

$$K_P^i = k_\eta^t L^2 2^{i-8} \tag{60}$$

so that with $i = 4$ the first and the third row of (32) have the same order of magnitude, so that the pantographic coefficient and the tension stiffness have the same role and order of magnitude in the 6th rank elasticity tensor but with $i = 3$ the pantographic coefficient is the half, with $i = 2$ it is one fourth and with $i = 1$ is one eighth, such that the characteristic length of the boundary layers can also be independently varied (controlled).

Finally, for the simulation setups one can see Table 3.

Table 2
Values of the pantographic coefficient K_p used in numerical tests.

	γ	$K_P = 0$	K_P^1 [J/m^2]	K_P^2 [J/m^2]	K_P^3 [J/m^2]	K_P^4 [J/m^2]
$\mathcal{P}_1$	1	0	$1.1 \cdot 10^8$	$2.2 \cdot 10^8$	$4.4 \cdot 10^8$	$8.8 \cdot 10^8$
$\mathcal{P}_2$	2	0	$4.4 \cdot 10^8$	$8.8 \cdot 10^8$	$17.6 \cdot 10^8$	$35.2 \cdot 10^8$
$\mathcal{P}_3$	5	0	$27.5 \cdot 10^8$	$55 \cdot 10^8$	$11 \cdot 10^9$	$22 \cdot 10^9$

5.4. Implementation of the numerical algorithm

For the solution of the problem formulated above, numerical effort is needed. To this end, an algorithm was developed for the numerical

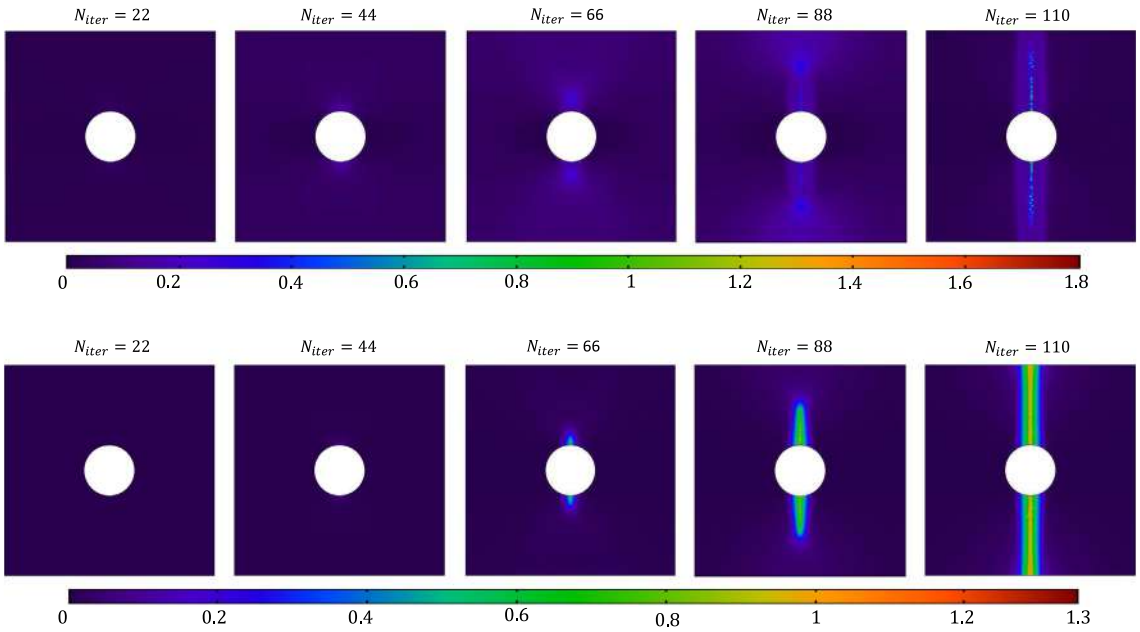

Fig. 11. Contour plots of elastic U (1st row) row) and dissipation W_D (2nd row) energy densities for $K_P = 0$ and for the $\mathcal{P}_1$ set of parameters defined in Tables 1–2.

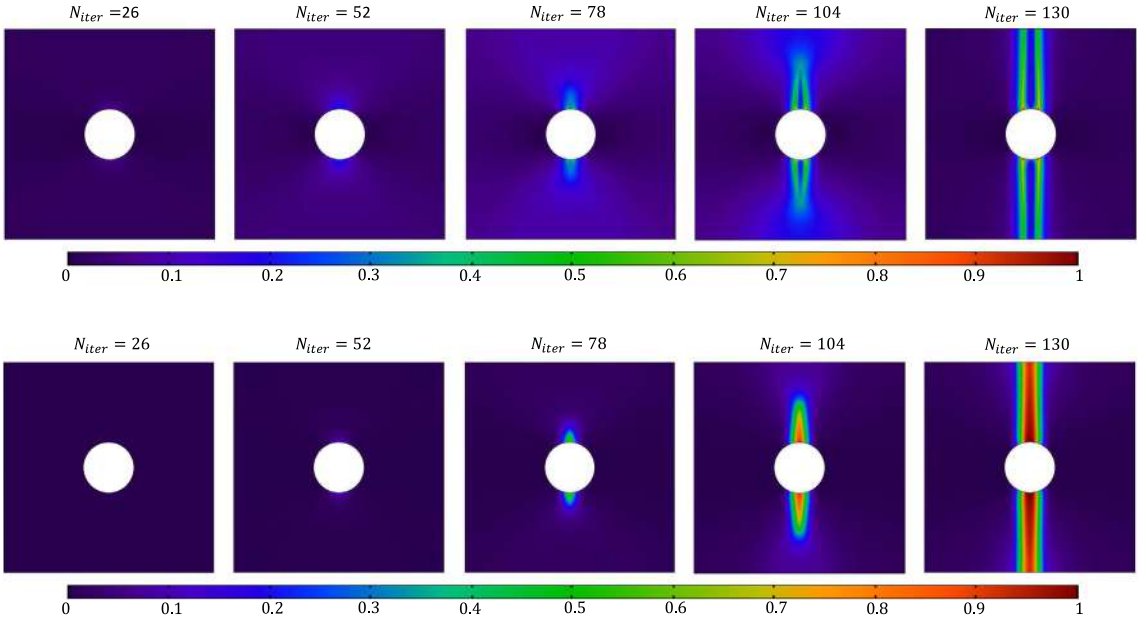

Fig. 12. Contour plots of elastic U (1st row) row) and dissipation W_D (2nd row) energy densities for $K_p = K_P^1 = 1.1 \cdot 10^8$ and for the $\mathcal{P}_1$ set of parameters defined in Tables 1–2.

Table 3
Numerical values used in numerical simulations.

N_θ	$\Delta\bar{u}$ [m]	$K_P = 0$		$K_P = K_P^i > 0$	
		N_{it}	$\bar{u}_{max}$ [m]	N_{it}	$\bar{u}_{max}$ [m]
120	$3.125 \cdot 10^{-9}$	150	$468.75 \cdot 10^{-9}$	250	$781.25 \cdot 10^{-9}$

implementation of the model. The continuum model is solved by means of the commercial software Matlab and COMSOL Multiphysics. An iterative procedure is implemented in a staggered fashion in Matlab as described in the flowchart in Fig. 7, making use of COMSOL Multiphysics as a subroutine solving the elastic equilibrium problem.

The steps of the iterative procedure can be resumed as follows:

1. null initial conditions on the displacement field $\boldsymbol{u}$ and damage fields D_η and D_τ are given together with the material parameters $L, k_\eta^c, k_\eta^t, k_\tau, B_\eta^c, B_\eta^t, B_{\tau 0}, K_P$, according to Tables 1–2. The stiffnesses $k_\eta^c, k_\eta^t, k_\tau$ given as input material parameters may be initially isotropic, i.e. they do not need to depend on the orientation angle θ. It is worth to mention that the effective (i.e. damaged-) stiffnesses $k_{\eta,D}^c, k_{\eta,D}^t, k_{\tau,D}$ may change during the evolution of the system due to the damage induced by the state of deformation, thus leading to non-isotropically distributed effective (damaged-) stiffnesses. Indeed, owing to Eq. (28), this is the reason why – for a given basis – the components of the elasticity tensors may change during the evolution of the system, possibly implying anisotropy shifts. The pantographic coefficient, on the contrary, does not experience damage;
2. the fourth-rank ($\mathbb{C}_{ijab}$), the fifth-rank ($\mathbb{M}_{ijabc}$) and the sixth-rank ($\mathbb{D}_{ijhabc}$) elasticity tensors are computed according to Eqs. (30),

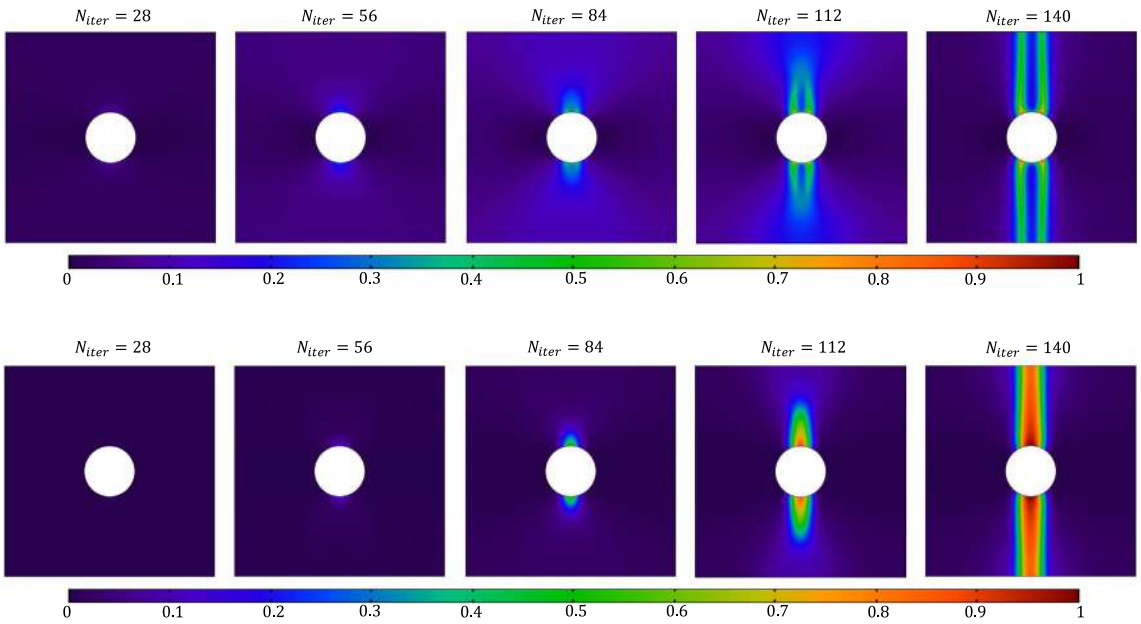

Fig. 13. Contour plots of elastic U (1st row) row) and dissipation W_D (2nd row) energy densities for $K_p = K_P^2 = 2.2 \cdot 10^8$ and for the $\mathcal{P}_1$ set of parameters defined in Tables 1–2.

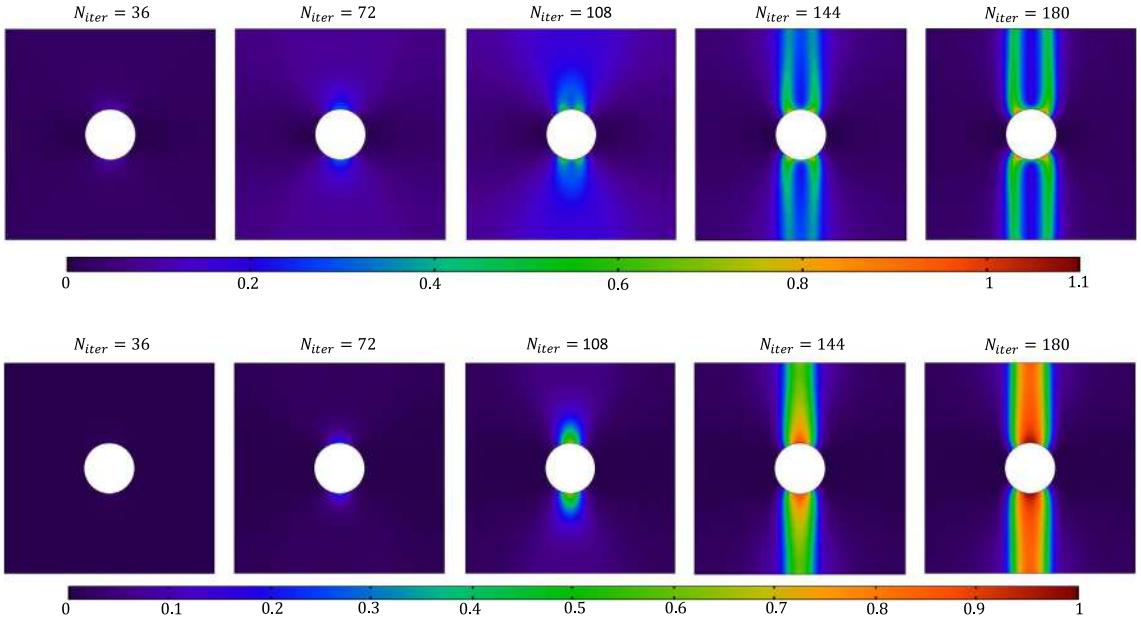

Fig. 14. Contour plots of elastic U (1st row) row) and dissipation W_D (2nd row) energy densities for $K_p = K_P^3 = 4.4 \cdot 10^8$ and for the $\mathcal{P}_1$ set of parameters defined in Tables 1–2.

(31) and (32). Such elastic tensors, as well as boundary conditions, are given as input to a finite element subroutine based on COMSOL Multiphysics. Particularly, the weak form of the equilibrium problem in Eq. (45) is solved by means of the *weak form* package. Quintic Argyris polynomials are used as shape functions ensuring C^2 continuity across elements along the normal to element boundaries. A Delaunay-tessellated triangular mesh was employed. Different mesh sizes were considered to investigate mesh independence. The output of this subroutine is the displacement field. It is worth to mention here that the pantographic coefficient K_p does not experience any change due to damage evolution;

3. the increment of the displacement field with respect to the previous step is node-wise compared with a tolerance. When such a tolerance is not respected, then the displacement parameters $\bar{u}$ or $\bar{u}_1$, $\bar{u}_2$ are reduced to re-initialize the finite element subroutine;
4. when the increment of the displacement field with respect to the previous step compares positively with the above-mentioned chosen tolerance, then the components of the strain field $\boldsymbol{G}$ and of its gradient are computed making use of the displacement field. The strain fields are then used by means of Eq. (11) to compute the relative displacements u_η and $\boldsymbol{u}_\tau$, which depend on the space coordinates and on the orientation θ. Such displacements are then given as input to the KKT conditions in Eqs. (50) and (51) and, as an output, the damage fields D_η and D_τ are recovered. In formulas, we have

$$D_\eta^t = \max\left\{\tilde{D}_\eta^t, D_\eta^{t-1}\right\}, \quad D_\tau^t = \max\left\{\tilde{D}_\tau^t, D_\tau^{t-1}\right\}, \tag{61}$$

where t is an index used to label the loading steps. Eqs. (61) have been conceived to take into account that, according to Eqs. (50) and (51), damage fields cannot decrease and they do not reach the unit value;

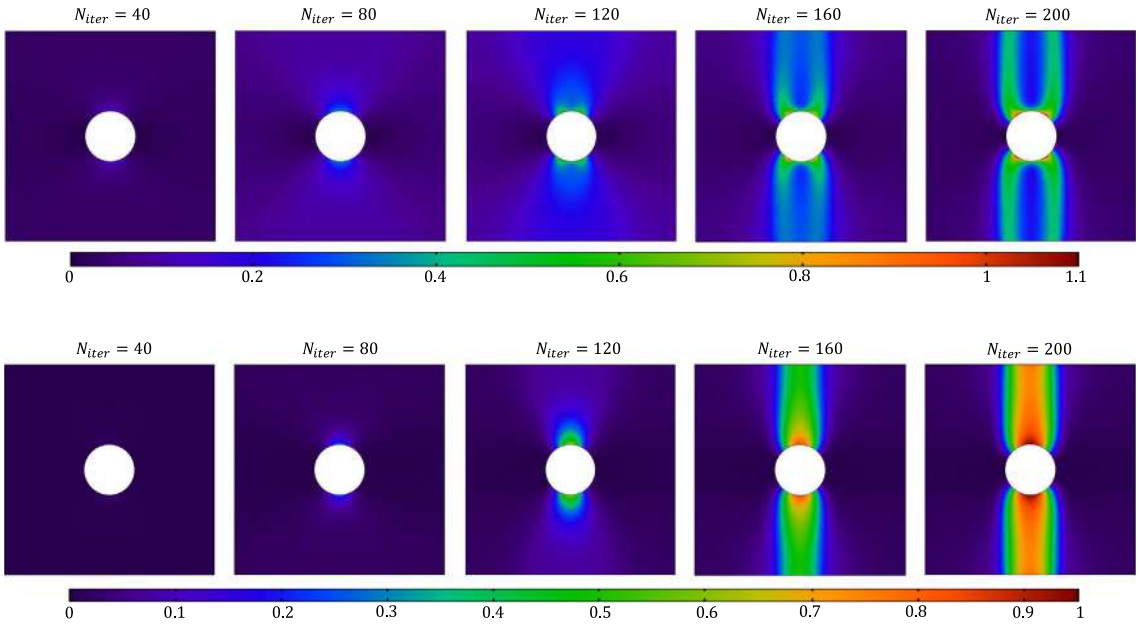

Fig. 15. Contour plots of elastic U (1st row) row) and dissipation W_D (2nd row) energy densities for $K_p = K_P^4 = 8.8 \cdot 10^8$ and for the $\mathcal{P}_1$ set of parameters defined in Tables 1–2.

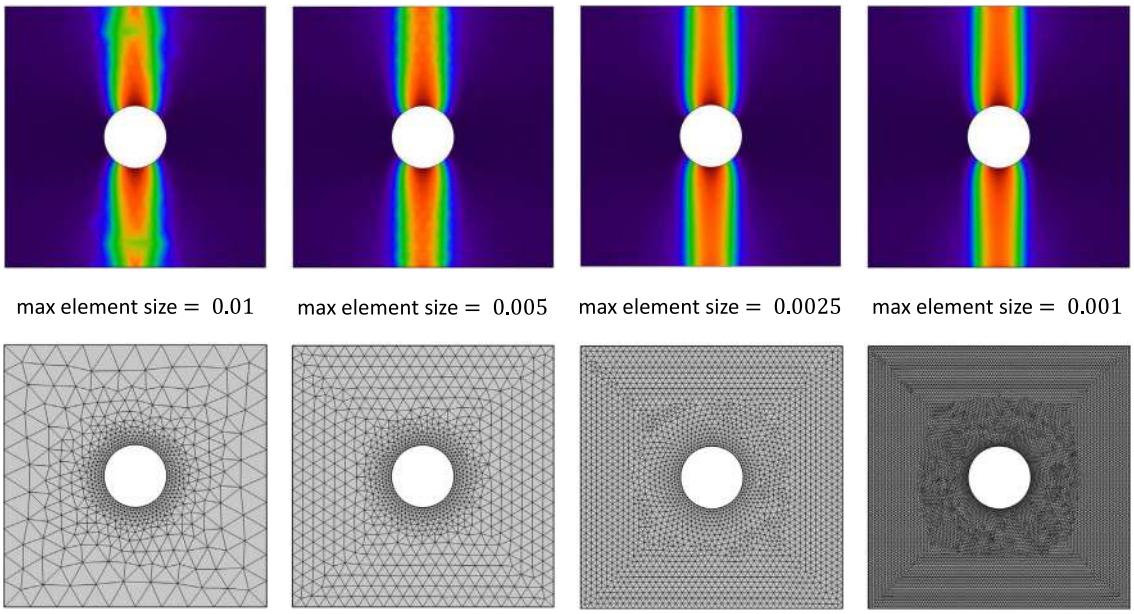

Fig. 16. Contour plots of dissipation energy density W_D (1st row) for $K_p = K_P^3 = 4.4 \cdot 10^8$ and for the $\mathcal{P}_1$ set of parameters defined in Tables 1–2 obtained for a given loading step $N_{it} = 180$ for different meshes (2nd row).

5. the load parameter $\bar{u}$ is increased.

The instructions above (from point 2) are repeated until a termination criterion is not verified. As mentioned at the beginning of the section, the termination criterion is given by $\bar{u}$ reaching a maximum desired value $\bar{u}_{max}$ or by reaching $\bar{u}_1$, $\bar{u}_2$ maximum values $\bar{u}_1^{max}$, $\bar{u}_2^{max}$ respectively.

5.5. Parametric analysis with respect to the pantographic coefficient for constant intergranular distance

In this subsection we consider results, according to Tables 1–2, of the $\mathcal{P}_1$ series of extension tests corresponding to the intergranular distance $L = 0.01$. The aim of performing these tests was to investigate mechanical properties of the model taking into account the pantographic interaction, which is imposed by choosing values of K_P different from zero, according to (60).

For the numerical loading process, we first perform a convergence analysis for the incremental loading size. Fig. 8 presents a convergence analysis with respect to the size of the load step $\Delta\bar{u}$. It is observed that convergence is taking place. For the subsequent simulations, $\Delta\bar{u} = 3.125 \cdot 10^{-9}$ is chosen, since the difference between the force displacement curve corresponding to this value of $\Delta\bar{u}$ and that related to the smallest $\Delta\bar{u}$ indicated in Fig. 8 is reasonably small, considering that for the smallest $\Delta\bar{u}$ it takes much more computational time to get results.

Fig. 9 shows that convergence with respect to the maximum mesh element size is taking place as well. For the subsequent simulations maximum element size equal to 0.001 is chosen.

In Fig. 10 one can see the computed force–displacement diagrams. It is clear from the plot that, by introducing K_P different from zero,

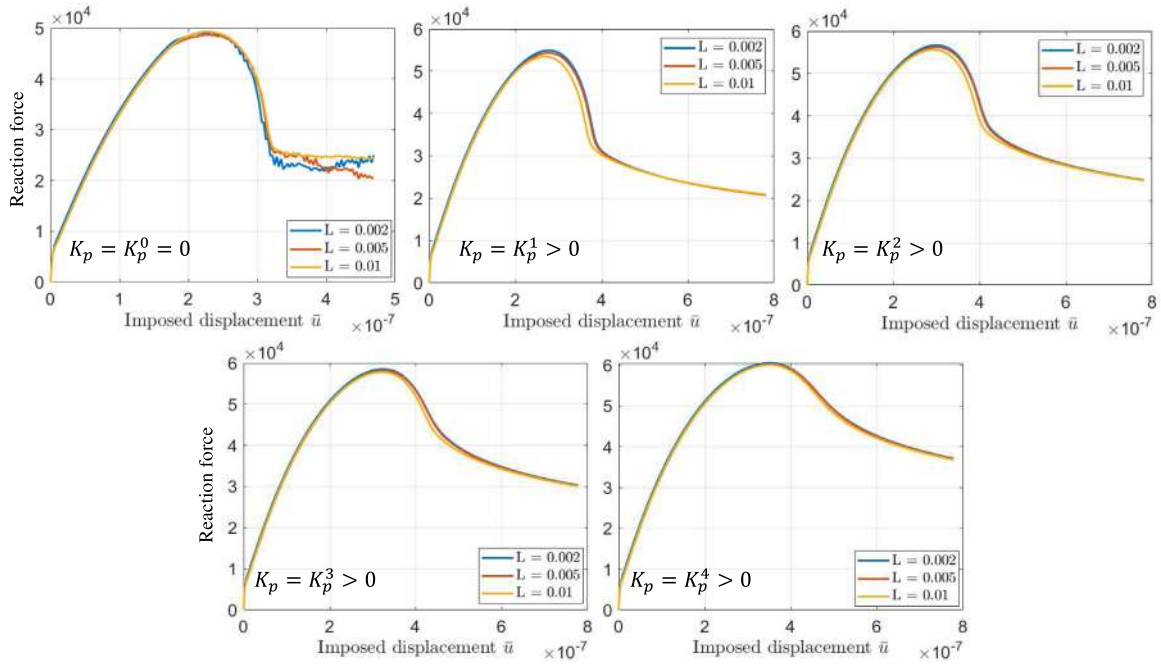

Fig. 17. Force versus displacement diagrams for different values of L and K_p.

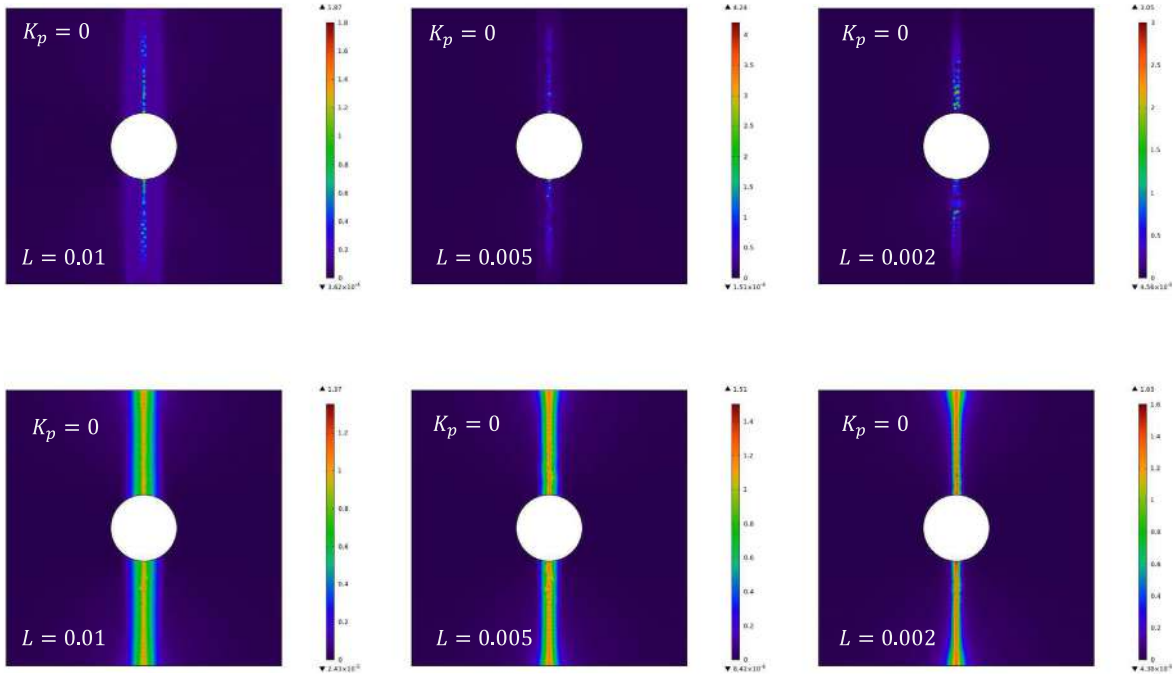

Fig. 18. Contour plots, at the final step, of elastic U (1st row) and dissipation W_D (2nd row) energy densities for $K_p = K_p^0$ and different L. All material parameters are rescaled in order to obtain the same Young modulus and Poissons ration for the calculations.

we obtain a stronger response of the sample with respect to the case of $K_P = 0$, as shown by the increase in peak reaction. Furthermore, increasing pantographic coefficient leads to an increase of the reaction force in the softening part of the response and a slowed rate of softening. The observed nature of the force–displacement curves can be exed by considering Eqs. (30)–(32), where expressions of elasticity tensors are presented. Specifically, the additional term K_P increases the values of the components of $\mathbb{D}$, and since K_P is not affected by damage, the components of $\mathbb{D}$ never vanish. Therefore, there will be always some elastic energy that is stored at each material point of the considered sample even as the damage within materials points tend to 1.

Figs. 11–15 show contour plots for elastic (1st row of contour plots) and dissipation (2nd row of contour plots) energy densities evolution throughout the simulation, where increasing N_{iter} indicates the increase in the imposed displacement. These contour plots show the development of concentration zones which emanate from the hole and grow towards the outer edges of the square specimen. The evolution of dissipation (due to damage in this case) is of particular interest in these simulations from the viewpoint of describing its localization as well as the characteristic length of the damage localization zone. These plots makes evident micro-mechanical effect of the pantographic interaction on the damage behavior on macro-scale. We can observe

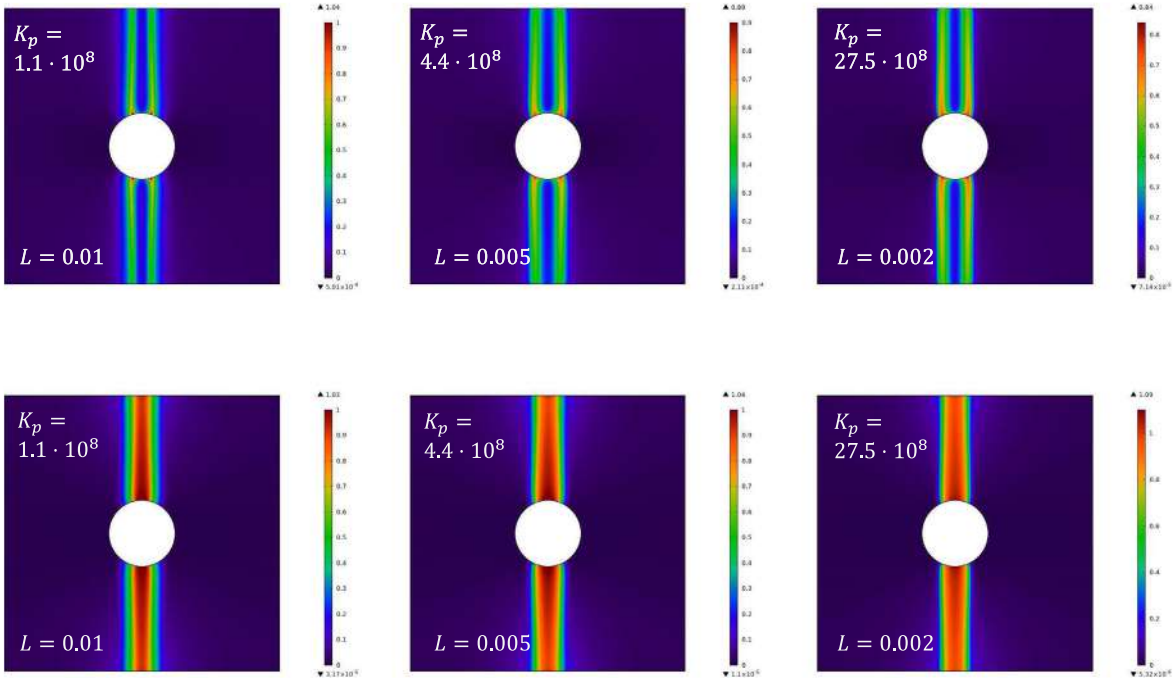

Fig. 19. Contour plots, at the final step, of elastic U (1st row) and dissipation W_D (2nd row) energy densities for $K_p = K_p^1$ and different L. All material parameters are re-scaled in order to obtain the same Young modulus and Poissons ratio for the calculations.

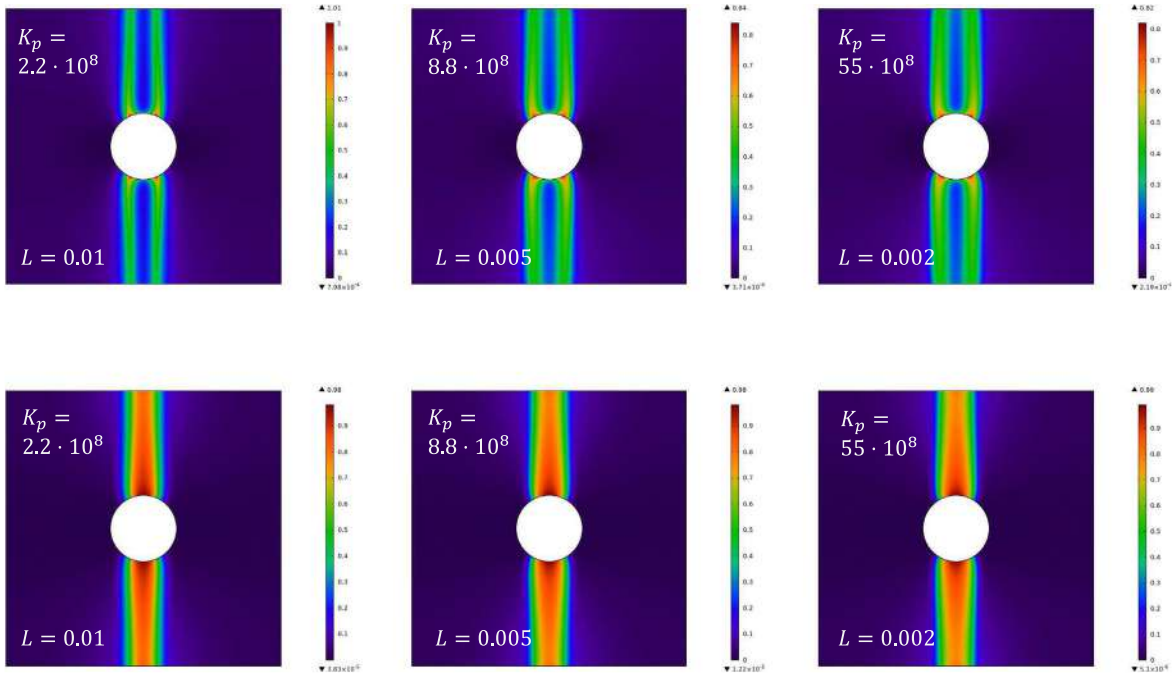

Fig. 20. Contour plots, at the final step, of elastic$U$ (1st row) and dissipation W_D (2nd row) energy densities for $K_p = K_p^2$ and different L. All material parameters (including K_p) are re-scaled in order to obtain the same Young modulus and Poissons ratio for the calculations.

that by choosing different pantographic coefficient, K_P, the width of the localization zone can be controlled. Indeed, a higher value of the pantographic coefficient, K_P, results in a thicker damage zone. We further note here that in the next section, the micromechanical effects are further illustrated by showing that model can predict localization zones that are independent of the intergranular distance, an effect which is a direct consequence of the pantographic interaction. The localization thickness could be described as proportional to the material characteristic length roughly estimated from the ratio of the 2nd and 1st gradient moduli in Eqs. (30)–(32), with the caveat that these moduli, and therefore, the characteristic lengths evolve during the loading process. For the case of pantographic coefficient, $K_P = 0$, the damage zone is thin as in this case it has the order of the averaged intergranular distance L. By selecting appropriate pantographic coefficient, K_P, the size of the localization zone can be increased in a pre-specified manner even to the order of the flaw size (in this case size of the circular hole), while keeping the averaged intergranular distance L unchanged. It is noteworthy, that the included pantographic effect can arise at

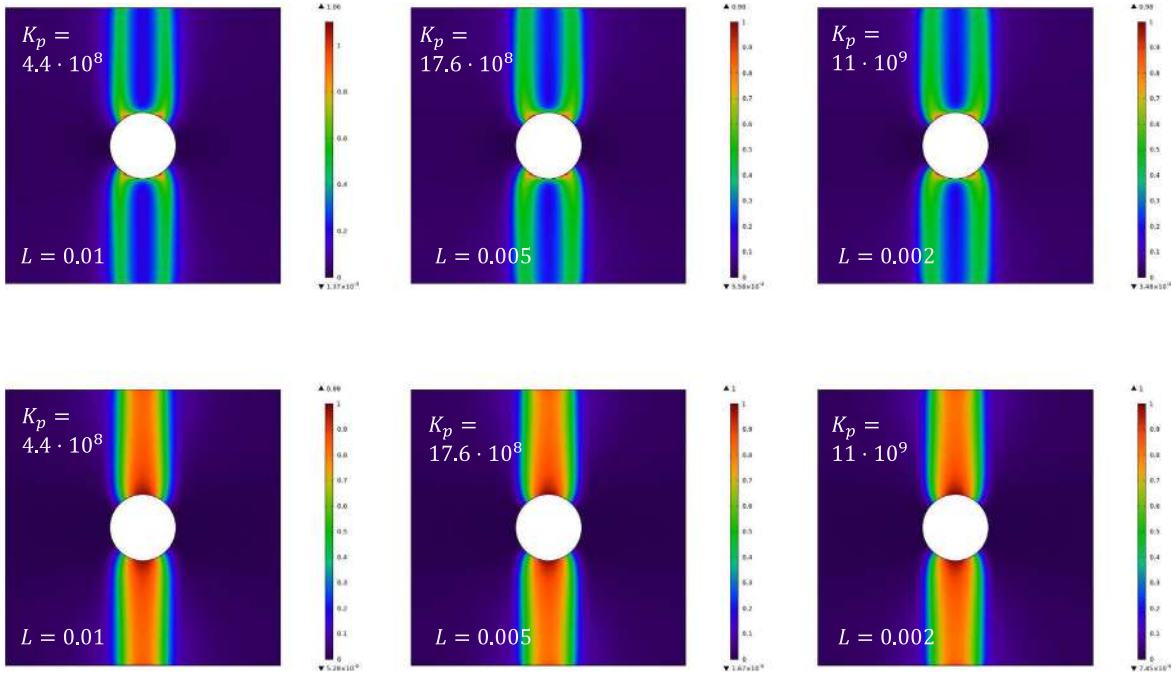

Fig. 21. Contour plots, at final step, of elastic U (1st row) and dissipation W_D (2nd row) energy densities for $K_p = K_p^3$ and different L. All material parameters (including K_p) are re-scaled in order to obtain the same Young modulus and Poissons ratio for the calculations.

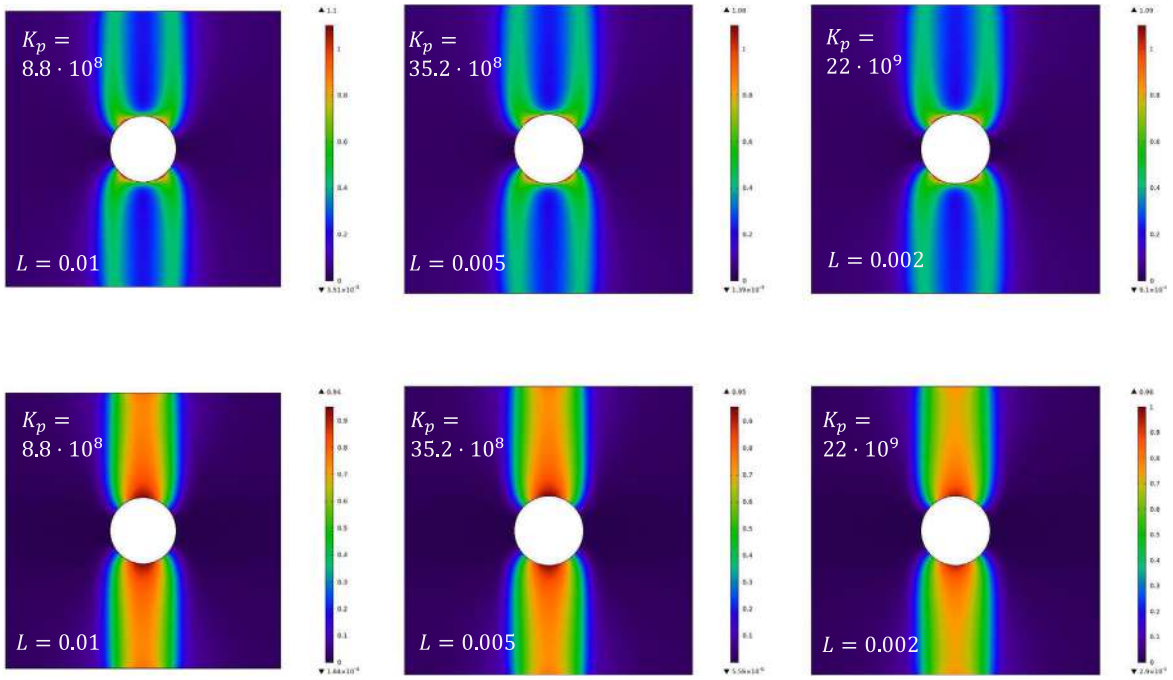

Fig. 22. Contour plots, at the final step, of elastic U (1st row) and dissipation W_D (2nd row) energy densities for $K_p = K_p^4$ and different L. All material parameters (including K_p) are re-scaled in order to obtain the same Young modulus and Poissons ratio for the calculations.

the micro- or grain-scale through a variety of long-range mechanisms, including grain rotation, that introduce floppy modes resulting from the micro-mechano-morphology of the material. Finally, it is worthwhile to note the concentration features in the elastic energy contours on the two edges of the damaged zone, which indicate the large elastic deformations that occur in the locations immediately contiguous to the damage localization.

Fig. 16 shows contour plots for dissipation energy (1st row of contour plots) with $K_P = K_P^2 = 2.2 \cdot 10^8$ for a given time step $N_{it} = 180$ and different meshes (2nd row of contour plots). It is observed, that thickness of the damaged area does not change with mesh refinement.

5.6. Parametric analysis for varying averaged intergranular distance

Fig. 17 shows 5 force–displacement diagrams, where each diagram is obtained for a given value of the pantographic coefficient $K_P = 0$ and $K_P = K_P^i$, $i = 1, \dots, 4$ and for different set of parameters $\mathcal{P}_1$ ($\gamma = 1$), $\mathcal{P}_2$ ($\gamma = 2$) or $\mathcal{P}_3$ ($\gamma = 5$). The plots indicate that the re-scaling adopted

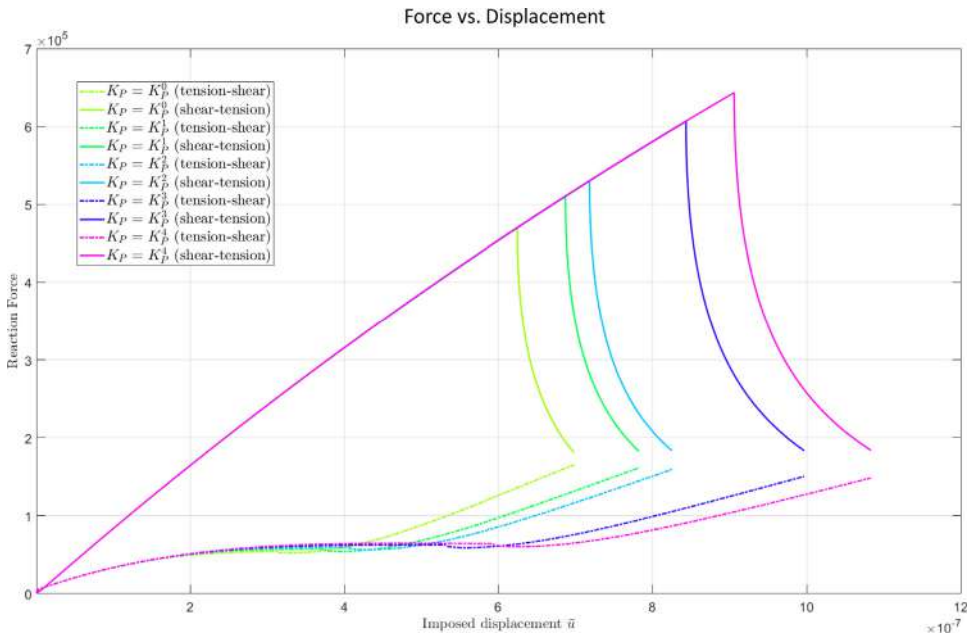

Fig. 23. Force versus displacement diagram for the $\mathcal{P}_1$ set of parameters defined in Tables 1–2 and for different values of K_P.

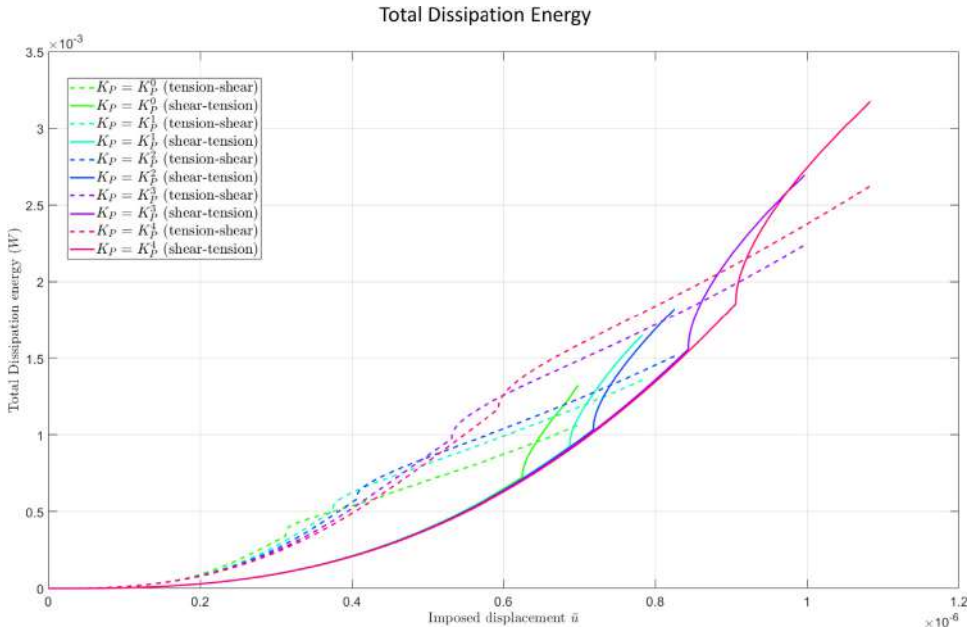

Fig. 24. Total dissipation energy versus displacement diagram for the $\mathcal{P}_1$ set of parameters defined in Tables 1–2 and for different values of K_P.

in Section 5.2 is valid because no significant difference is recognized for different values of γ and the higher is the pantographic coefficient K_P, the lower is such a difference.

Figs. 18–22 show contour plots for elastic (1st row of contour plots) and dissipation (2nd row of contour plots) energy densities at the final time step and for different sets of parameters $\mathcal{P}_1$ ($\gamma = 1$), $\mathcal{P}_2$ ($\gamma = 2$) or $\mathcal{P}_3$ ($\gamma = 5$) corresponding to different values of the intergranular distance L. It can be seen from the plots, that when $K_P = 0$ decreasing L implies also the reduction of the thickness of the damaged area, such that as the intergranular distance L, tends to vanish, the thickness of the localization zone will also vanish. Indeed, in most past micro-macro identification in which 2nd gradient stiffnesses are proportional to the square of the RVE or to the lattice size, or the intergranular distance L as it is here for $K_P = 0$, the 2nd gradient constants vanish in the limit of such a size going to zero. In these cases, the localization zone is restricted to be the size of the intergranular distance L.

However, for the cases $K_P = K_P^i > 0$, $i = 1, \dots, 4$ the situation is different. We can see that enhancing the pantographic interaction K_P means to attenuate such a reduction of the thickness of the damaged area. In other words, as the pantographic coefficient K_P increases, the thickness of the damage localization zone becomes independent of the intergranular distance L. In fact, through the proposed re-scaling, we define a family of discrete systems whose structural response remains invariant to change of grain size, but whose damage localization zone can be independently varied by accounting for the long-range effects modeled using the pantographic coefficient K_P. Hence, we may conjecture that physical systems obeying the discrete description could be designed such that second gradient effect remains non-negligible

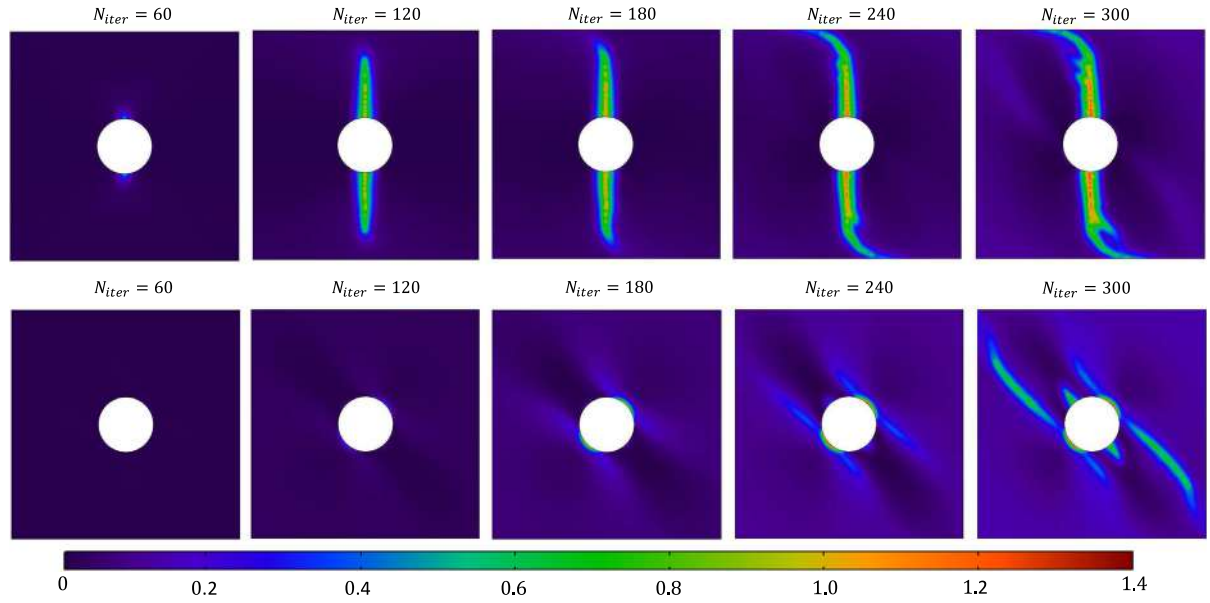

Fig. 25. Contour plots of dissipation W_D energy densities tension–shear (1st row) and shear–tension (2nd row) for $K_P = 0$ and for the $\mathcal{P}_1$ set of parameters defined in Tables 1–2.

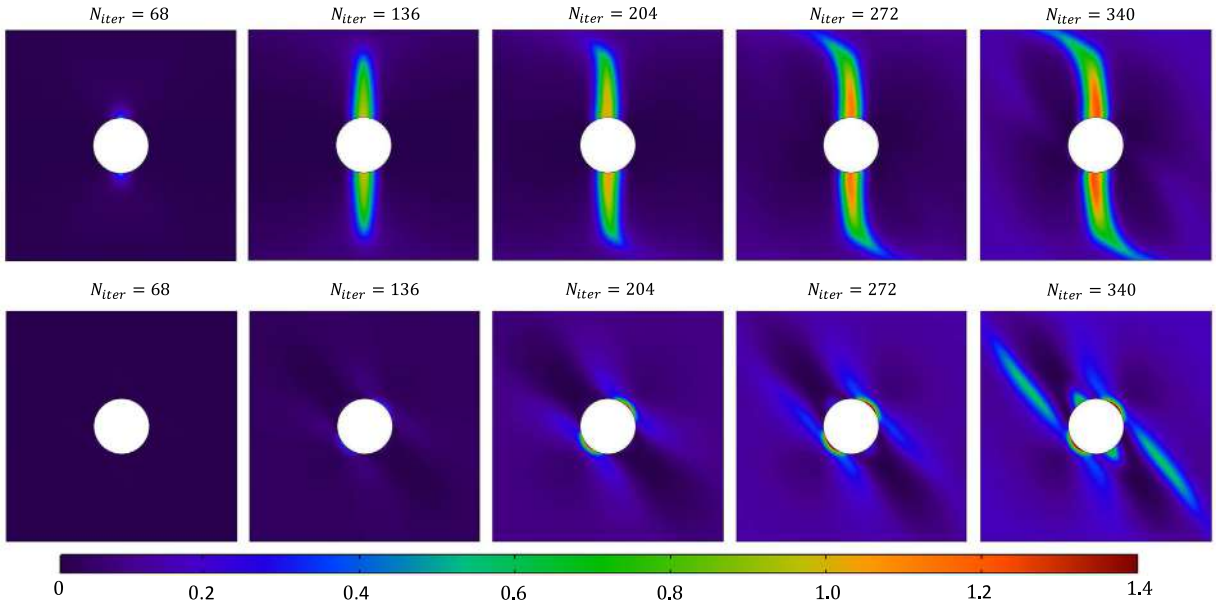

Fig. 26. Contour plots of dissipation W_D energy densities tension–shear (1st row) and shear–tension (2nd row) for $K_P = K_p^1$ and for the $\mathcal{P}_1$ set of parameters defined in Tables 1–2.

even for very dense physical systems. In this sense, embedding micro-structural interactions giving a non-zero gradient effect into an existing micro-structure could significantly improve the mechanical properties of the material.

5.7. Path-dependency of damage localization evolution

To further highlight the micromechanical effects on the macro damage model, we contrast the morphology of damage evolution under the tension–shear and shear–tension loading paths illustrated in Fig. 6. The details of the simulation steps for the two loading-paths are given in Table 4, where we note that the number of load-steps to reach a comparative damage condition increase with increasing K_P as seen from Fig. 10.

Further, in Fig. 23 we give the calculated reaction force–displacement response for the tension–shear and shear–tension simulations, where we consider the resultant reaction force and the imposed resultant displacement at the right vertical boundary. We can see, that the response for the tension–shear simulations is significantly different from the one for shear–tension simulations for each K_P. In particular, we can observe that the shear–tension response, which is dominated by the grain-scale shear interactions, are considerably

Table 4
Number of load-steps.

$K_P = K_p^0$	$N_{it}^{tens} = 100$	$N_{it}^{shear} = 200$	$N_{it}^{total} = 300$
$K_P = K_p^1$	$N_{it}^{tens} = 120$ (+20)	$N_{it}^{shear} = 220$ (+20)	$N_{it}^{total} = 340$
$K_P = K_p^2$	$N_{it}^{tens} = 130$ (+30)	$N_{it}^{shear} = 230$ (+30)	$N_{it}^{total} = 360$
$K_P = K_p^3$	$N_{it}^{tens} = 170$ (+70)	$N_{it}^{shear} = 270$ (+70)	$N_{it}^{total} = 440$
$K_P = K_p^4$	$N_{it}^{tens} = 190$ (+90)	$N_{it}^{shear} = 290$ (+90)	$N_{it}^{total} = 480$

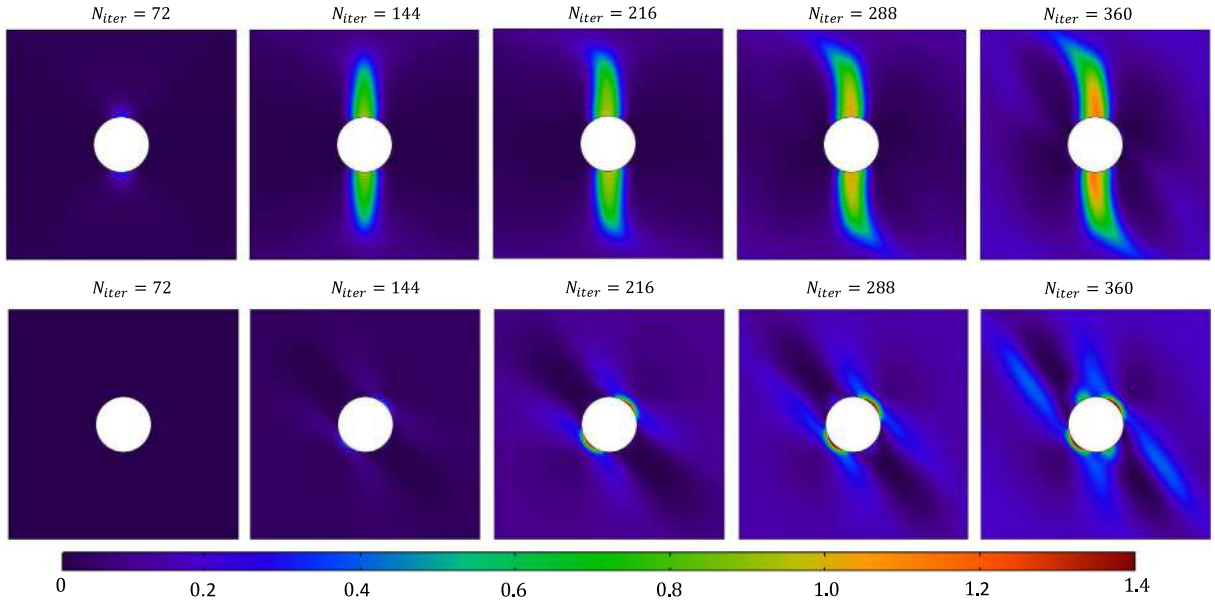

Fig. 27. Contour plots of dissipation W_D energy densities tension–shear (1st row) and shear–tension (2nd row) for $K_P = K_p^2$ and for the $\mathcal{P}_1$ set of parameters defined in Tables 1–2.

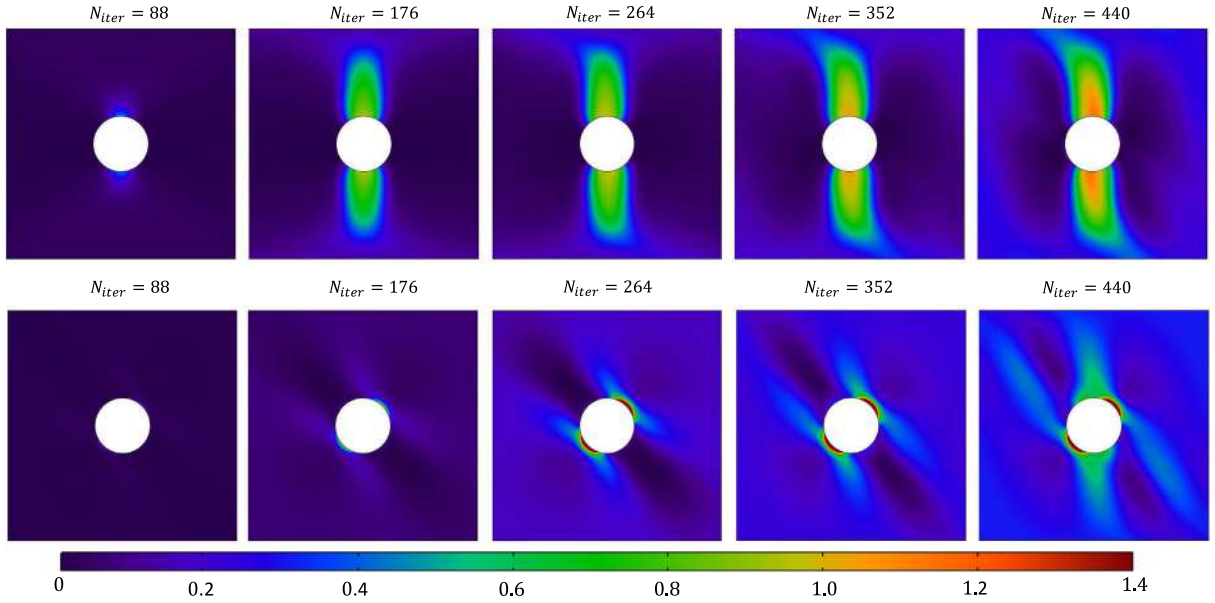

Fig. 28. Contour plots of dissipation W_D energy densities tension–shear (1st row) and shear–tension (2nd row) for $K_P = K_p^3$ and for the $\mathcal{P}_1$ set of parameters defined in Tables 1–2.

softer compared to the tension–shear response, dominated by the grain-scale normal interactions. The same conclusion can be made from Fig. 24 where total dissipation energy versus displacement diagram is presented. However, it is also interesting to observe that the final reaction, at the end of the loading, are close for both cases of simulations for each K_P. So although it appears that for a given deformed shape, the reaction force or dissipated energies are similar, the micromechanical effects predicate the loading path dependency of the force–displacement response during the loading process. This point is further illustrated by the evolution of the damage localization as shown in the Figs. 25–30 which show contour plots for dissipation energy densities evolution tension–shear (1st row of contour plots) and shear–tension (2nd row of contour plots) tests throughout the simulation for different K_P, where increasing N_{iter} indicates the increase in the imposed displacement. In the tension–shear test, we see that the damage zone progresses vertically, during the tensile phase, and subsequently tilts in the shear phase of the of loading path to form a winged zone. Furthermore, increasing K_P, results in controlling the thickness of the damage zone as well as in suppressing the emergence or manifestation of tilt. In contrast, in the shear–tension test we observe a completely different evolution of damage zone which develops in the diagonal direction under the shear phase and further grows diagonally under the tension phase. Although some rotation of the diagonal damage zone towards the vertical is notable whose extent is controlled by the pantographic coefficient K_P. It is clear from these simulation that the micro-macro correlations and the introduction of the pantographic coefficient K_P, introduce unprecedented load-path dependency that

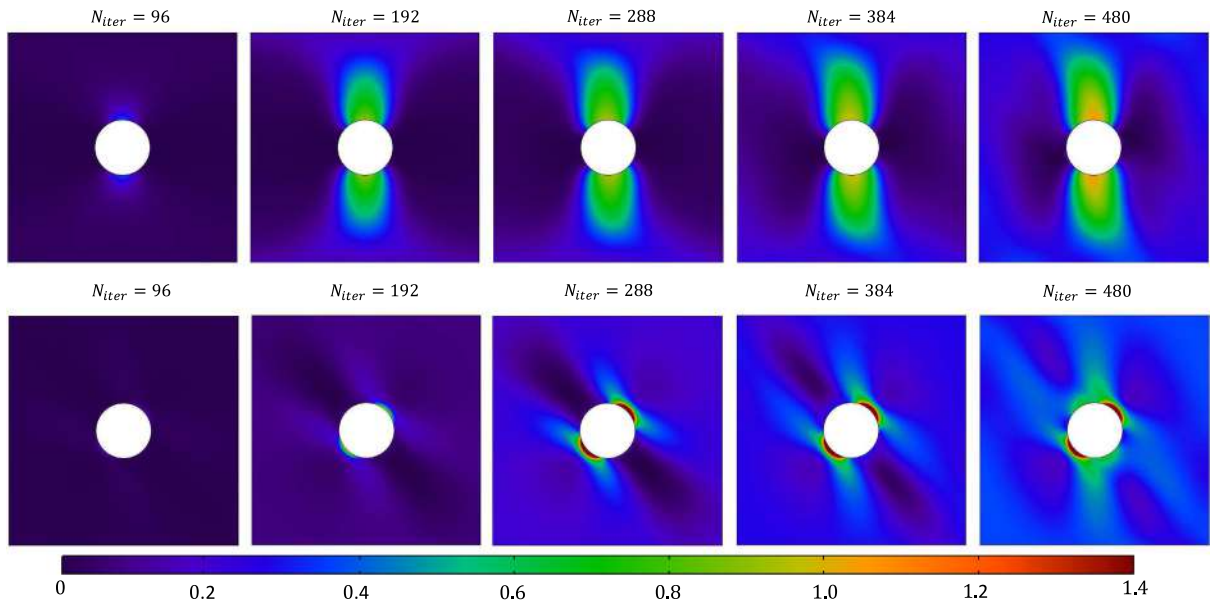

Fig. 29. Contour plots of dissipation W_D energy densities tension–shear (1st row) and shear–tension (2nd row) for $K_P = K_p^4$ and for the $\mathcal{P}_1$ set of parameters defined in Tables 1–2.

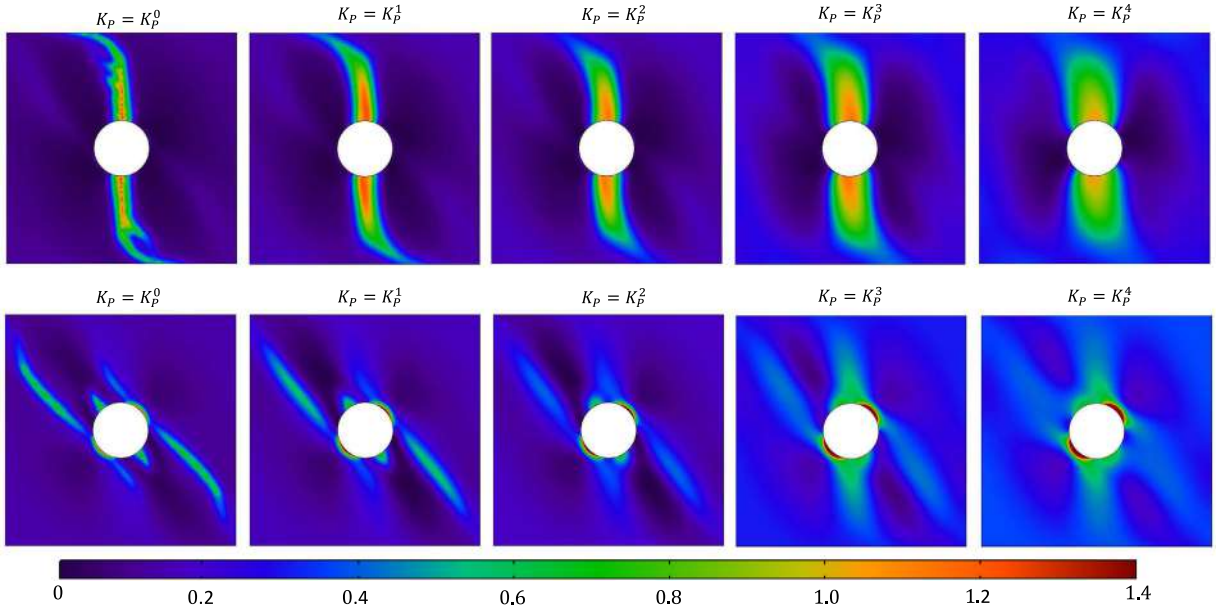

Fig. 30. Contour plots of dissipation W_D energy densities tension–shear (1st row) and shear–tension (2nd row) for $K_P = K_p^2$ and for the $\mathcal{P}_1$ set of parameters defined in Tables 1–2 to compare the last time-steps of the simulations.

leads to completely different states at the end of the loading otherwise characterized by the same overall deformed shape of the specimen and similar reaction force as exemplified in Fig. 30.

6. Conclusion

The key findings of the work reported here is that long-range (beyond nearest neighbor) mechanism must be included in continuum models based upon micro-macro identification derived from discrete models. Here, we have shown that by including at micro-scale additional pantographic grain-pair interactions that store elastic energy in response to strain gradients, we can control at macro-scale the thickness of the localization zones that form as failure (fracture) nucleates from certain prescribed weakness. This outcome is demonstrated via numerical simulation of localization nucleation and propagation in a plate with prescribed hole. The influence of the pantographic term is observed both in the case of single loading and in more complex experiments. We find completely different localization characteristics even for the same final deformed shape of the specimen. This localization strongly depends upon the loading-path and reflects the consequences of different loading history for each grain-pair direction at the microscale. The results illustrate the capabilities of the micro-macro identification based upon the granular micromechanics paradigm, which we have demonstrated models load path dependency that gives rise to evolving anisotropy and material chirality as well as growth of localization zones from location other than the prescribed weakness. Future outlooks of the present work include the applications of the present framework to the study of more complex loading conditions and materials, as well as the development of actual granular metamaterials with pantographic connections. For those parameters

related to damage dissipation energy there is a work in progress to find a proper way for their experimental validation.

Declaration of competing interest

The authors declare that they have no known competing financial interests or personal relationships that could have appeared to influence the work reported in this paper.

Acknowledgments

AM is supported in part by the United States National Science Foundation grant CMMI -1727433. This project has received funding from the European Union's Horizon 2020 research and innovation program under the Marie Skłodowska-Curie grant agreement No 899546.

References

Askes, Harm, Aifantis, Elias C., 2011. Gradient elasticity in statics and dynamics: an overview of formulations, length scale identification procedures, finite element implementations and new results. Int. J. Solids Struct. 48 (13), 1962–1990.

Askes, Harm, Metrikine, Andrei V., 2005. Higher-order continua derived from discrete media: continualisation aspects and boundary conditions. Int. J. Solids Struct. 42 (1), 187–202.

Babuska, Ivo, Oden, J. Tinsley, 2004. Verification and validation in computational engineering and science: basic concepts. Comput. Methods Appl. Mech. Engrg. 193 (36), 4057–4066.

Barchiesi, Emilio, Eugster, Simon R., Placidi, Luca, dell'Isola, Francesco, 2019. Pantographic beam: a complete second gradient 1D-continuum in plane. Z. Angew. Math. Phys. 70 (5), 1–24.

Barchiesi, E., Laudato, M., Di Cosmo, F., 2018. Wave dispersion in non-linear pantographic beams. Mech. Res. Commun. 94, 128–132.

Boutin, C., Giorgio, I., Placidi, L., et al., 2017. Linear pantographic sheets: Asymptotic micro-macro models identification. Math. Mech. Complex Syst. 5 (2), 127–162.

Brach, Stella, Tanné, Erwan, Bourdin, Blaise, Bhattacharya, Kaushik, 2019. Phase-field study of crack nucleation and propagation in elastic–perfectly plastic bodies. Comput. Methods Appl. Mech. Engrg. 353, 44–65.

Carcaterra, A., dell'Isola, F., Esposito, R., Pulvirenti, M., 2015. Macroscopic description of microscopically strongly inhomogeneous systems: A mathematical basis for the synthesis of higher gradients metamaterials. Arch. Ration. Mech. Anal. 218 (3), 1239–1262.

Carrara, Pietro, Ambati, Marreddy, Alessi, Roberto, De Lorenzis, Laura, 2020. A framework to model the fatigue behavior of brittle materials based on a variational phase-field approach. Comput. Methods Appl. Mech. Engrg. 361, 112731.

Chang, Ching S., Gao, Jian, 1995. Second gradient constitutive theory for granular material with random packing structure. Int. J. Solids Struct. 32 (16), 2279–2293.

Coutris, Nicole, Thompson, Lonny L., Kosaraju, Sai, 2020. Asymptotic homogenization models for pantographic lattices with variable order rotational resistance at pivots. J. Mech. Phys. Solids 134, 103718.

De Angelo, Michele, Placidi, Luca, Nejadsadeghi, Nima, Misra, Anil, 2020. Non-standard timoshenko beam model for chiral metamaterial: Identification of stiffness parameters. Mech. Res. Commun. 103, 103462.

Del Vescovo, D., Giorgio, I., 2014. Dynamic problems for metamaterials: review of existing models and ideas for further research. Internat. J. Engrg. Sci. 80, 153–172.

dell'Isola, F., Bucci, S., Battista, A., 2016a. Against the fragmentation of knowledge: The power of multidisciplinary research for the design of metamaterials. Z. Angew. Math. Phys. 67 (4).

dell'Isola, F., Giorgio, I., Pawlikowski, M., Rizzi, N., 2016b. Large deformations of planar extensible beams and pantographic lattices: heuristic homogenization, experimental and numerical examples of equilibrium. Proc. R. Soc. Lond. Ser. A Math. Phys. Eng. Sci. 472 (2185), 20150790.

dell'Isola, Francesco, Turco, Emilio, Misra, Anil, Vangelatos, Zacharias, Grigoropoulos, Costas, Melissinaki, Vasileia, Farsari, Maria, 2019. Force–displacement relationship in micro-metric pantographs: Experiments and numerical simulations. Comp. R. Méc. 347 (5), 397–405.

Fang, Jianguang, Wu, Chengqing, Rabczuk, Timon, Wu, Chi, Sun, Guangyong, Li, Qing, 2020. Phase field fracture in elasto-plastic solids: a length-scale insensitive model for quasi-brittle materials. Comput. Mech. 66 (4), 931–961.

Giorgio, Ivan, Ciallella, Alessandro, Scerrato, Daria, 2020a. A study about the impact of the topological arrangement of fibers on fiber-reinforced composites: some guidelines aiming at the development of new ultra-stiff and ultra-soft metamaterials. Int. J. Solids Struct. 203, 73–83.

Giorgio, Ivan, dell'Isola, Francesco, Misra, Anil, 2020b. Chirality in 2D cosserat media related to stretch-micro-rotation coupling with links to granular micromechanics. Int. J. Solids Struct. 202, 28–38.

Golaszewski, Maciej, Grygoruk, Roman, Giorgio, Ivan, Laudato, Marco, Di Cosmo, Fabio, 2019. Metamaterials with relative displacements in their microstructure: technological challenges in 3D printing, experiments and numerical predictions. Contin. Mech. Thermodyn. 31 (4), 1015–1034.

Jia, D., Ramesh, K.T., Ma, E., 2003. Effects of nanocrystalline and ultrafine grain sizes on constitutive behavior and shear bands in iron. Acta Mater. 51 (12), 3495–3509.

Joshi, Shailendra P., Ramesh, K.T., 2008. Rotational diffusion and grain size dependent shear instability in nanostructured materials. Acta Mater. 56 (2), 282–291.

Kumar, Aditya, Bourdin, Blaise, Francfort, Gilles A., Lopez-Pamies, Oscar, 2020. Revisiting nucleation in the phase-field approach to brittle fracture. J. Mech. Phys. Solids 142, 104027.

Maranganti, R., Sharma, P., 2007. A novel atomistic approach to determine strain-gradient elasticity constants: Tabulation and comparison for various metals, semiconductors, silica, polymers and the (ir) relevance for nanotechnologies. J. Mech. Phys. Solids 55 (9), 1823–1852.

Miehe, C., Teichtmeister, S., Aldakheel, F., 2016. Phase-field modelling of ductile fracture: a variational gradient-extended plasticity-damage theory and its micromorphic regularization. Phil. Trans. R. Soc. A 374 (2066), 20150170.

Misra, Anil, Nejadsadeghi, Nima, De Angelo, Michele, Placidi, Luca, 2020. Chiral metamaterial predicted by granular micromechanics: verified with 1D example synthesized using additive manufacturing. Contin. Mech. Thermodyn. 32 (5), 1497–1513.

Misra, Anil, Placidi, Luca, dell'Isola, Francesco, Barchiesi, Emilio, 2021. Identification of a geometrically nonlinear micromorphic continuum via granular micromechanics. Z. Angew. Math. Phys. 72 (4), 1–21.

Misra, A., Poorsolhjouy, P., 2015. Granular micromechanics model for damage and plasticity of cementitious materials based upon thermomechanics. Math. Mech. Solids 1081286515576821.

Misra, A., Singh, V., 2015. Thermomechanics-based nonlinear rate-dependent coupled damage-plasticity granular micromechanics model. Contin. Mech. Thermodyn. 27 (4–5), 787.

Mohsenizadeh, Mehrdad, Gasbarri, Federico, Munther, Michael, Beheshti, Ali, Davami, Keivan, 2018. Additively-manufactured lightweight metamaterials for energy absorption. Mater. Des. 139, 521–530.

Molnár, Gergely, Doitrand, Aurélien, Estevez, Rafaël, Gravouil, Anthony, 2020. Toughness or strength? Regularization in phase-field fracture explained by the coupled criterion. Theor. Appl. Fract. Mech. 109, 102736.

Nejadsadeghi, Nima, Placidi, Luca, Romeo, Maurizio, Misra, Anil, 2019. Frequency band gaps in dielectric granular metamaterials modulated by electric field. Mech. Res. Commun. 95, 96–103.

Nguyen, Hoang Thai, Pathirage, Madura, Cusatis, Gianluca, Bažant, Zdeněk P, 2020. Gap test of crack-parallel stress effect on quasibrittle fracture and its consequences. J. Appl. Mech. 87 (7), 071012.

Oberkampf, William L., Trucano, Timothy G., Hirsch, Charles, 2004. Verification, validation, and predictive capability in computational engineering and physics. Appl. Mech. Rev. 57 (5), 345–384.

Ouali, M. Ould, Poorsolhjouy, P., Placidi, L., Misra, A., 2021. Evaluation of the effects of stress concentrations on plates using granular micromechanics. Constr. Build. Mater. 290, 123227.

Placidi, Luca, Barchiesi, Emilio, Misra, Anil, 2018a. A strain gradient variational approach to damage: a comparison with damage gradient models and numerical results. Math. Mech. Complex Syst. 6 (2), 77–100.

Placidi, Luca, Barchiesi, Emilio, Misra, Anil, Timofeev, Dmitry, 2021. Micromechanics-based elasto-plastic-damage energy formulation for strain gradient solids with granular microstructure. Contin. Mech. Thermodyn. 1–29.

Placidi, Luca, Misra, Anil, Barchiesi, Emilio, 2018b. Two-dimensional strain gradient damage modeling: a variational approach. Z. Angew. Math. Phys. 69 (3), 56.

Placidi, Luca, Misra, Anil, Barchiesi, Emilio, 2019. Simulation results for damage with evolving microstructure and growing strain gradient moduli. Contin. Mech. Thermodyn. 31 (4), 1143–1163.

Polyzos, D., Fotiadis, D.I., 2012. Derivation of Mindlin's first and second strain gradient elastic theory via simple lattice and continuum models. Int. J. Solids Struct. 49 (3–4), 470–480.

Pook, Leslie Philip, 2000. Linear Elastic Fracture Mechanics for Engineers: Theory and Applications. WIT Press.

Rahali, Y., Giorgio, I., Ganghoffer, J.F., Dell'Isola, F., 2015. Homogenization à la Piola produces second gradient continuum models for linear pantographic lattices. Internat. J. Engrg. Sci. 97, 148–172.

Schwer, L.E., 2007. An overview of the PTC 60/V& V 10: Guide for verification and validation in computational solid mechanics. Eng. Comput. 23 (4), 245–252.

Seppecher, Pierre, Spagnuolo, Mario, Barchiesi, Emilio, Hild, François, Lekszycki, Tomasz, Giorgio, Ivan, Placidi, Luca, Andreaus, Ugo, Cuomo, Massimo, Eugster, Simon R., et al., 2019. Advances in pantographic structures: design, manufacturing, models, experiments and image analyses. Contin. Mech. Thermodyn. 31 (4).

Spagnuolo, Mario, Peyre, Patrice, Dupuy, Corinne, 2019. Phenomenological aspects of quasi-perfect pivots in metallic pantographic structures. Mech. Res. Commun. 101, 103415.

Tanné, Erwan, Li, Tianyi, Bourdin, Blaise, Marigo, J-J, Maurini, Corrado, 2018. Crack nucleation in variational phase-field models of brittle fracture. J. Mech. Phys. Solids 110, 80–99.

Timofeev, Dmitry, Barchiesi, Emilio, Placidi, Luca, Misra, Anil, 2020. Hemivariational continuum approach for granular solids with damage-induced anisotropy evolution. Math. Mech. Solids 26, 1–33.

TMS, The Minerals Metals & Materials Society (TMS), 2019. Verification & Validation of Computational Models Associated with the Mechanics of Materials. TMS, Pittsburgh, PA.

Tokaji, Keiro, Ogawa, Takeshi, Harada, Yukio, 1987. Evaluation on limitation of linear elastic fracture mechanics for small fatigue crack growth. Fatigue Fract. Eng. Mater. Struct. 10 (4), 281–289.

Triantafyllidis, Nicolas, Bardenhagen, S., 1993. On higher order gradient continuum theories in 1-D nonlinear elasticity. Derivation from and comparison to the corresponding discrete models. J. Elasticity 33 (3), 259–293.

Trippel, Antonina, Stilz, Maximilian, Gutmann, Florian, Ganzenmueller, Georg C, Hiermaier, Stefan, 2020. A device for characterizing rotational joints in metamaterials. Mech. Res. Commun. 104, 103501.

Turco, Emilio, 2019. Numerically driven tuning of equilibrium paths for pantographic beams. Contin. Mech. Thermodyn. 31 (6), 1941–1960.

Turco, Emilio, 2021. A numerical survey of nonlinear dynamical responses of discrete pantographic beams. Contin. Mech. Thermodyn. 1–21.

Turco, Emilio, Barchiesi, Emilio, dell'Isola, Francesco, 2021. A numerical investigation on impulse-induced nonlinear longitudinal waves in pantographic beams. Math. Mech. Solids 10812865211010877.

Turco, E., dell'Isola, F., Rizzi, N.L., Grygoruk, R., Müller, W.H., Liebold, C., 2016. Fiber rupture in sheared planar pantographic sheets: Numerical and experimental evidence. Mech. Res. Commun. 76, 86–90.

Turco, Emilio, Rizzi, Nicola Luigi, 2016. Pantographic structures presenting statistically distributed defects: numerical investigations of the effects on deformation fields. Mech. Res. Commun. 77, 65–69.

Wang, C., Qian, X., 2018. Heaviside projection based aggregation in stress constrained topology optimization. Internat. J. Numer. Methods Engrg. 115 (7), 849–871.

Yildizdag, Mustafa Erden, Tran, Chuong Anthony, Barchiesi, Emilio, Spagnuolo, Mario, dell'Isola, Francesco, Hild, François, 2019. A multi-disciplinary approach for mechanical metamaterial synthesis: a hierarchical modular multiscale cellular structure paradigm. In: State of the Art and Future Trends in Material Modeling. Springer, pp. 485–505.

Zheng, Xiaoyu, Lee, Howon, Weisgraber, Todd H, Shusteff, Maxim, DeOtte, Joshua, Duoss, Eric B, Kuntz, Joshua D, Biener, Monika M, Ge, Qi, Jackson, Julie A, et al., 2014. Ultralight, ultrastiff mechanical metamaterials. Science 344 (6190), 1373–1377.

Chapter 5

Dynamic modeling of strain gradient fracture propagation

This chapter presents a physico-mathematical model for dynamic fracture propagation in materials with strain gradient effects. The second gradient approach is applied to develop the model, which is implemented in the finite elements simulations. The model is validated by comparing the simulation results with experimental data obtained from fracture tests on notched specimens. The comparison shows good agreement between the model predictions and experimental measurements done by Ozbolt . The simulations reveal that strain gradient effects significantly affect the fracture propagation process, leading to finite fracture thickness that is independet of the mesh topology. In addition, the effects of kinetic energy and, therefore loading rate, on fracture behavior is investigated for the first time in framework for strain-gradient materials. The results show that increasing the kinetic energy and loading rate leads to a deviation of a standard mode-I crack propogation. This study highlights the importance of considering the effects of kinetic energy and loading rate in fracture mechanics models for accurate predictions of fracture behavior in materials. The presented model and simulation results can be useful in the design and optimization of structural components subjected to dynamic loading conditions.

5.1 Introduction

Fracture mechanics is a fundamental field of study that seeks to understand the behavior and mechanics of cracks in various materials. Over the years, extensive research has focused on studying fracture processes under static conditions, providing valuable insights into crack initiation, propagation, and structural failure. However, in many real-world scenarios, materials are subjected to dynamic loading conditions, where cracks can propagate at high speeds and exhibit unique fracture behaviors [13], [97], [61], [100], [93], [81], [54], [59]. Understanding the mechanics of dynamic fracture is crucial for enhancing the safety and reliability of structural components and advancing the design of resilient materials. The mechanics of dynamic fracture is much more complicated than that under quasi-static loading condition [71, 72, 73, 74]. Experimental studies show the practical relevance of it [101], [88], [34], [20], [36], [11], [99], [25] . Some experimental analysis show the dependence of loading or strain rate on fracture [43], [35], [92], [98], [38], [41], [90], [56], [60].

Dynamic fracture phenomena occur in a wide range of applications, including engineering [16], automotive safety [46], medicine [89], biology [94], and even natural disasters such as earthquakes [35]. Examples of dynamic fracture events include rapid crack propagation in structural components under impact or explosion, fragmentation of brittle materials under high-velocity impacts, and crack propagation in geological formations due to seismic activity. The study of dynamic fracture mechanics aims to unravel the underlying mechanisms governing the

initiation, propagation, and arrest of cracks under these extreme loading conditions.

Experimental analysis conducted in [57] demonstrated the dependence of fracture path on the loading rate. In a theoretical paper aimed at describing fracture path and branching phenomena, the authors used a microplane model [58] in a 3D numerical simulation. In works [10], [91], [32] to describe [57] were used different approaches like peridynamic model and phase-field damage model. The strain gradient with inertia gradient effects was used in [83] and show capability of give approach in analitical solution without application of finite element method (FEM). Present work shows good comparability with experimental data using the application of FEM.

5.2 Formulation of the problem

5.2.1 Preliminary definitions

Let us consider 2D continuum body $\mathfrak{V} \subset E^2$, where the domain E^2 is Euclidean two-dimensional space. The position of every single point on its body is established through the utilization of X coordinates in some frame of reference. The set of kinematical descriptors for such a model contains both, the the displacement field $u = u(X,t)$ and damage field $\omega = \omega(X,t)$. The damage state of a material point X is therefore characterized, at time t and again for the sake of simplicity, by a scalar internal variable ω, that is assumed to be within the range [0, 1]. The case $\omega = 0$ corresponds to the undamaged state while $\omega = 1$ corresponds to complete failure. Let us perform the dynamic approximation, that is equivalent to say that we have inertia force, i.e., the kinetic energy. We assume the material to be not self-healing and, hence, ω is assumed to be a non-decreasing function of time. If we consider the damaged material as a microstructured material where damage results in a microstructure, it becomes significant to allow the internal deformation energy density to vary based on the second gradient of the displacement. Thus, because of objectivity, the deformation density energy functional is assumed to be a function of the strain tensor G, of its gradient ∇G and of the damage ω, i.e. $U = U(G, \nabla G, \omega)$. Here, $G = \frac{1}{2}\left(F^T F - I\right)$, where $F = \nabla\chi$ is deformation gradient tensor, $\chi = X + u$ is the placement function, F^T is the transpose of F. For the small displacement approximation that is dealt in this work, the strain tensor G is assumed to be equal to $E = Sym(H)$, the symmetric part of the displacement gradient $H = \nabla u$.

5.2.2 Deformation energy functional

The deformation energy functional $\mathcal{E}(u,\omega)$ depends on the displacement u and the damage ω was determinated in [67] and fields as follows:

$$\mathcal{E}(u,\omega) = \int_{\mathfrak{V}} \left[U(G,\nabla G,\omega) - b^{ext}\cdot u - m^{ext} : \nabla u\right] dA - \int_{\partial\mathfrak{V}} [t^{ext}\cdot u + \tau^{ext}\cdot[(\nabla u)n]]ds - \int_{\partial\partial\mathfrak{V}} f^{ext}\cdot u \qquad (5.1)$$

where n is the unit external normal; the dot $(\cdot)$ indicates the scalar product between vectors or tensors; b^{ext} and m^{ext} are respectively the external body force and double force (per unit area); t^{ext} and τ^{ext} are respectively the external force and double force (per unit length); f^{ext} is the external concentrated force which is applied on the vertices $[\partial\partial\mathfrak{V}]$.

5.2.3 Variational principle

In order to get governing equations for this model, we resort to the variational principle thoroughly presented in [96, 62, 64], where the case of one-dimensional bodies was considered. We assume that the descriptors $u(X,t)$ and $\omega(X,t)$ verify the condition:

$$\delta\mathcal{E}(u,\omega,\dot{u},\dot{\omega}) \leq \delta\mathcal{E}(u,\omega,\nu,\beta), \qquad \forall\nu,\ \forall\beta \geq 0, \qquad (5.2)$$

where ν and β are compatible virtual velocities and dots represent derivation with respect to time.
The functional $\delta\mathcal{E}(u,\omega,\delta u,\delta\omega)$ must be defined as follows:

$$\delta\mathcal{E}(u,\omega,\delta u,\delta\omega)=\int_{\mathfrak{V}}\left[\frac{\partial U}{\partial G}\delta G+\frac{\partial U}{\partial\nabla G}\delta\nabla G+\frac{\partial U}{\partial\omega}\delta\omega-b^{ext}\cdot\delta u-m^{ext}:\delta\nabla u\right]+$$
$$-\int_{\partial\mathfrak{V}}[t^{ext}\cdot\delta u+\tau^{ext}\cdot(\delta\nabla u)n]-\int_{\partial\partial\mathfrak{V}}f^{ext}\cdot\delta u.$$

5.2.4 Reduction from the 3D Mindlin elastic strain gradient energy to the 2D explicit form

A general form of the elastic part U_e of the internal deformation energy density functional U of a 3D isotropic second gradient elastic material is provided in [47]. When the specialization of 5.3 to the plane strain case ($u_{1,3}=u_{2,3}=u_3=0$) is considered, we have

$$U_e(G,\nabla G)=\frac{\lambda}{2}G_{ii}G_{jj}+\mu G_{ij}G_{ij}+2c_3G_{ii,j}G_{jh,h}+\frac{c_4}{2}G_{ii,k}G_{ll,k}+2c_5G_{ij,i}G_{jm,m}+c_6G_{ij,k}G_{ij,k}+2c_7G_{ij,k}G_{ki,j}\quad(5.3)$$

where λ, μ, c_3, c_4, c_5, c_6, $c_7\in\mathbb{R}$ are independent parameters; λ and μ referred to as Lamé parameters (that can be easily related to the Young modulus Y and and to the Poisson ratio ν) and this choise is clear by looking in 5.3 without the last five strain gradient terms. The parameters λ, μ, c_3-c_7 don't depend upon the strain tensor (or its gradient) while they are functions of $X\in\mathfrak{V}$ and t, i.e., they are scalar fields depending upon time. The coefficients c_3-c_7 due to the granular approach according [6] are determinated as follows

$$\begin{cases} c_3=YL^2\frac{\nu}{112(1+\nu)(1-2\nu)}=\frac{L^2}{112}\lambda,\\ c_4=YL^2\frac{\nu}{112(1+\nu)(1-2\nu)}=\frac{L^2}{112}\lambda,\\ c_5=YL^2\frac{7-8\nu}{2240(1+\nu)(1-2\nu)}=\frac{L^2}{2240}(7\mu+3\lambda),\\ c_6=YL^2\frac{7-18\nu}{1120(1+\nu)(1-2\nu)}=\frac{L^2}{1120}(7\mu-4\lambda),\\ c_7=YL^2\frac{7-8\nu}{2240(1+\nu)(1-2\nu)}=\frac{L^2}{2240}(7\mu+3\lambda). \end{cases}\quad(5.4)$$

We now include the damage ω by including, in the internal deformation energy function U not only its elastic part U_e but also with a dissipation energy. It is worth to note that in our isotropic model we want to avoid the evolution of damage in compression and see it only in tension. For this we introduce the condition 5.6 that damage evaluate only in the case when trace of G is positive and bigger its treshold.

$$U(G,\nabla G,\omega)=U_e(G,\nabla G,\omega)+\frac{1}{2}k_\omega\omega^2\mathbb{H}(TrG-\gamma)\quad(5.5)$$

$$TrG\geqslant\gamma,\ \gamma\in\mathbb{R}_+\quad(5.6)$$

where k_ω represent the resistance to damage, $\mathbb{H}$ is Heaviside function, TrG is trace of G, γ is trace of G treshold.
The explicit form, with respect to damage, of the density of the elastic energy

$$U_e(G,\nabla G,\omega)=(\frac{\lambda}{2}G_{ii}G_{jj}+\mu G_{ij}G_{ij})\cdot(1-\mathscr{R}\cdot\omega)+(2c_3G_{ii,j}G_{jh,h}+\frac{1}{2}c_4G_{ii,k}G_{ll,k}\quad(5.7)$$
$$+2c_5G_{ij,i}G_{jm,m}+c_6G_{ij,k}G_{ij,k}+2c_7G_{ij,k}G_{ki,j})\cdot(1+\mathscr{M}\cdot\omega)$$

where $\mathscr{R}$ - controls the 1^{st} gradient residual inside the fracture, $\mathscr{M}$ - parameter controls micro−structure due

to damage. Parameters $\mathscr{R}$ and $\mathscr{M}$ should be as close as possible to the value 1.

By choosing $\nu = \dot{u}$ and $\beta = 0$ (followed by the choice $\beta = 2\dot{\omega}$ and then by the choice $\beta = \dot{\omega}$)

$$\frac{\partial U}{\partial \omega} \geq 0 \qquad \forall X \in \mathcal{B} \tag{5.8}$$

$$\frac{\partial U}{\partial \omega}\dot{\omega} = 0 \qquad \forall X \in \mathcal{B} \tag{5.9}$$

thus

$$\begin{aligned}\frac{\partial U}{\partial \omega}(G, \nabla G, \omega) = (-\mathscr{R}) \cdot (\frac{\lambda}{2} G_{ii} G_{jj} + \mu G_{ij} G_{ij}) + (\mathscr{M}) \cdot (2c_3 G_{ii,j} G_{jh,h} + \frac{1}{2} c_4 G_{ii,k} G_{ll,k} \\ +2c_5 G_{ij,i} G_{jm,m} + c_6 G_{ij,k} G_{ij,k} + 2c_7 G_{ij,k} G_{ki,j}) + k_\omega \omega H(TrG - \gamma) = 0\end{aligned} \tag{5.10}$$

where damage on current step calculate according:

$$\omega = -\left[\frac{\partial U_e}{\partial \omega} / \left[k_\omega \cdot \mathbb{H}(TrG - \gamma)\right]\right]. \tag{5.11}$$

In the case of no external distributed actions i.e., in the case $b^{ext} = m^{ext} = 0$, from the condition 5.9 and taking into account 5.12 and 5.13

$$G_{ij} = \frac{1}{2}(u_{i,j} + u_{j,i}) \tag{5.12}$$

$$G_{ij,k} = \frac{1}{2}(u_{i,jk} + u_{j,ik}) \tag{5.13}$$

we get the general form

$$\begin{aligned}\omega(X,t) = \{\left[\frac{\lambda}{2} u_{i,i} u_{j,j} + \frac{\mu}{4}(u_{i,j} + u_{j,i})^2\right] * \mathscr{R} + \Big[c_3 u_{i,ij}(u_{j,hh} + u_{h,jh}) + \frac{c_4}{2} u_{i,ij} u_{l,lk} \\ + \frac{c_5}{2}(u_{i,ji} + u_{j,ii})(u_{j,mm} + u_{m,jm}) + \frac{c_6}{4}(u_{i,jk} + u_{j,ik})^2 + \frac{c_7}{2}(u_{i,jk} + u_{j,ik})(u_{k,ij} + u_{i,kj})\Big] * (-\mathscr{M})\}/k_\omega.\end{aligned} \tag{5.14}$$

If $\omega(X,t)$, computed by using 5.14, is such that $\dot{\omega} < 0$ then $\dot{\omega} = 0$, otherwise the damage value calculated with 5.14 is assumed to be valid. Indeed, fixed $X \in \mathfrak{V}$ and for each time step t the following condition must be verified

$$\omega(X,t) \geq \omega(X, t - \triangle t).$$

If this is not the case, then

$$\omega(X,t) = \omega(X, t - \triangle t).$$

The kinetic energy part is assumed to be as follows:

$$U_k = \frac{1}{2}\rho\left[\left(\frac{\partial u_1}{\partial t}\right)^2 + \left(\frac{\partial u_2}{\partial t}\right)^2\right]. \tag{5.15}$$

where ρ is material density per unit area, u_1 and u_2 are displacement in horizontal and vertical directions, t is time of the action.

It is possible to prove that the equivalent to have

$$b^{ext} = -\rho\ddot{u}.$$

5.3 Numerical results

5.3.1 Description of the numerical experiments

In the current section, we present numerical simulations to show the capabilities of the derived model to describe initiation and growth of damage localization zones. Following [57]we consider 2D square specimen with a notch (pre-crack). The follow types of numerical experiments is employed: the left edge of the notch (the blue line) is fixed in the opposite of $\hat{e_x}$ direction while the right edge of the notch (the red line) is subjected to a applied velocity in the $\hat{e_x}$ direction (from left to right). Fig. 5.1 illustrates this loading type. In the original paper [57] there are twelve cases of different applied velocities, the loading-rates are in the range from 0.045 m/s to 4.298m/s. In this section, only four cases of tested velocities are picked up for study, which are Case 1: 0.491 m/s; Case 2: 1.375 m/s; Case 3: 3.268 m/s and Case 4: 4.298 m/s.

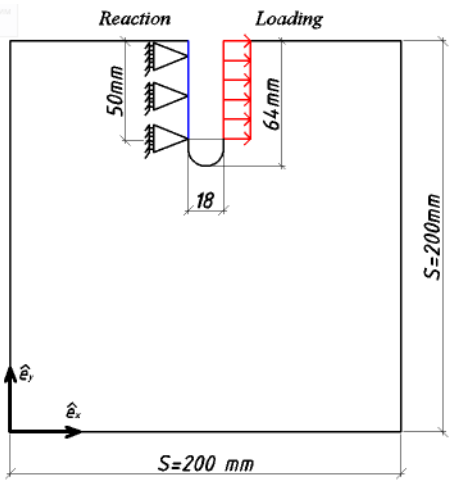

Figure 5.1: Schematics of analyzed domains and considered boundary conditions.

Since, the data of the actual loading history used in the experiments was not reported , in the current study, the applied velocity is assumed to be modelled as

$$v = \begin{cases} \frac{t}{t_0} v_0 & if\ t \leq t_0 \\ v_0 & if\ t > t_0 \end{cases} \tag{5.16}$$

with t_0= 100 μs and t= 500 μs.

Representation of velocity function for given value v_0=3.268 m/s on imposed displacements versus time diagram showed in Fig. 5.2.

The constitutive parameters used in numerical simulations in damage case are represented in Tab. 5.1, where Y is Young's modulus, ν - Poisson's ratio, L - characteristic length (intergranular distance), ρ - density, kw - resistance of damage, t_f - time horizon, $\triangle t$ - time step,

It should be noted that simulations were done for 2D case, in this case to take into account the thickness of the specimen (it is 25 mm) some constitutive parameters were multiplied by this value.

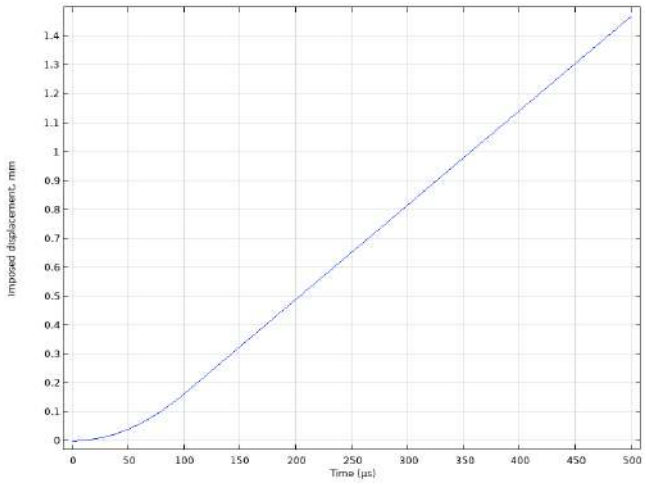

Figure 5.2: Representation of velocity function for value v=3.268 m/s on imposed displacements versus time diagram

Y	ν	L	ρ	k_ω	t_f	$\triangle t$	γ	$\mathscr{R}$	$\mathscr{M}$
15 GPa	0.18	0.01118 m	2400 kg/m^3	5 J/m^2	500 μs	0.5 μs	0,0012	0,99999	0,99999

Table 5.1: Values of constitutive parameters used in numerical tests.

5.3.2 Convergence analysis

For convergence analysis it was done 2 kinds of numerical simulations: elastic and damage. To avoid damage and have only elastic simulation Trace of G (TrG) threshold was applied $TrG > 1$. In elastic simulation it was shown that strain gradient regularization gives better convergence with respect to finite element size while without it implementations the mesh should be refine more.

From Figs 5.3-5.4 we can see, that without implementation of second gradient there is no convergence for given values of maximum finite element size, however the implementation of this term lead us to convergence with refinement of mesh. From Figs 5.5-5.6 we can see that we got the better convergence for maximum finite element size=0,002 m.

This approach was approved also in damage case with applied velocity v_0=3,268 m/s. On Fig. 5.7 shown the representation of mesh with different maximum finite element size. On Fig. 5.8 shown comparison of of reaction force versus time diagrams (the first row) and damage contour plots (the second row) with respect to different maximum finite element size. Damage contour plot correspond to the time when the fracture arrived to the boundary. This moment indicates by arrow on reaction force diagram. We can see that behavior of the fracture path every time the same. Also important thing that on the Fig. 5.9we can compare the thickness of the fracture with different mesh. For a maximum finite element size=0.004 we can see only one damaged element, however with decreasing of element size the number of elements increases and the thickness of the crack is almost the same for all simulations. That show to us mesh independence of the results. From Fig. 5.10we can see that the evolution of reaction force in time is almost the same but the maximum value it get at different time moment, also fracture reaches the boundary in different time. A maximum mesh size of 0.001 m was chosen for the following simulations

5.3.3 Numerical results with different loading rate.

According the convergence analysis it was done set of numerical simulations with the same constitutive parameters from Tab.5.1 for a mesh with maximum element size=0.001m.The difference between the simulations - the value of applied velocity. It was done comparison of the results with experimental data.

On Figs. 5.11, 5.12 and 5.13 showed the results for applied velocity v=0,491 m/s. On Figs. 5.14, 5.15 and

degrees of freedom	number of elements	Maximum element size	Reaction force	Integration over the *t*
656 (plus 660 internal DOFs)	110	0,1	77,35	17,6204
684 (plus 690 internal DOFs)	115	0,08	76,87	17,5195
752 (plus 768 internal DOFs)	128	0,066	77,15	17,5876
796 (plus 816 internal DOFs)	136	0,04	76,16	17,408
1108 (plus 1170 internal DOFs)	195	0,026	76,17	17,433
1614 (plus 1752 internal DOFs)	292	0,02	76,01	17,3816
2768 (plus 3084 internal DOFs)	514	0,0134	75,43	17,284
3526 (plus 3966 internal DOFs)	661	0,0106	75,52	17,3038
5200 (plus 5922 internal DOFs)	987	0,008	75,32	17,2693
14500 (plus 16908 internal DOFs)	2818	0,004	75,5	17,3041
51046 (plus 60360 internal DOFs)	10060	0,002	75,17	17,2411
186276 (plus 221946 internal DOFs)	36991	0,001	74,8	17,1749

Figure 5.3: Data from convergence analysis without implementation of strain gradient for different mesh sizes

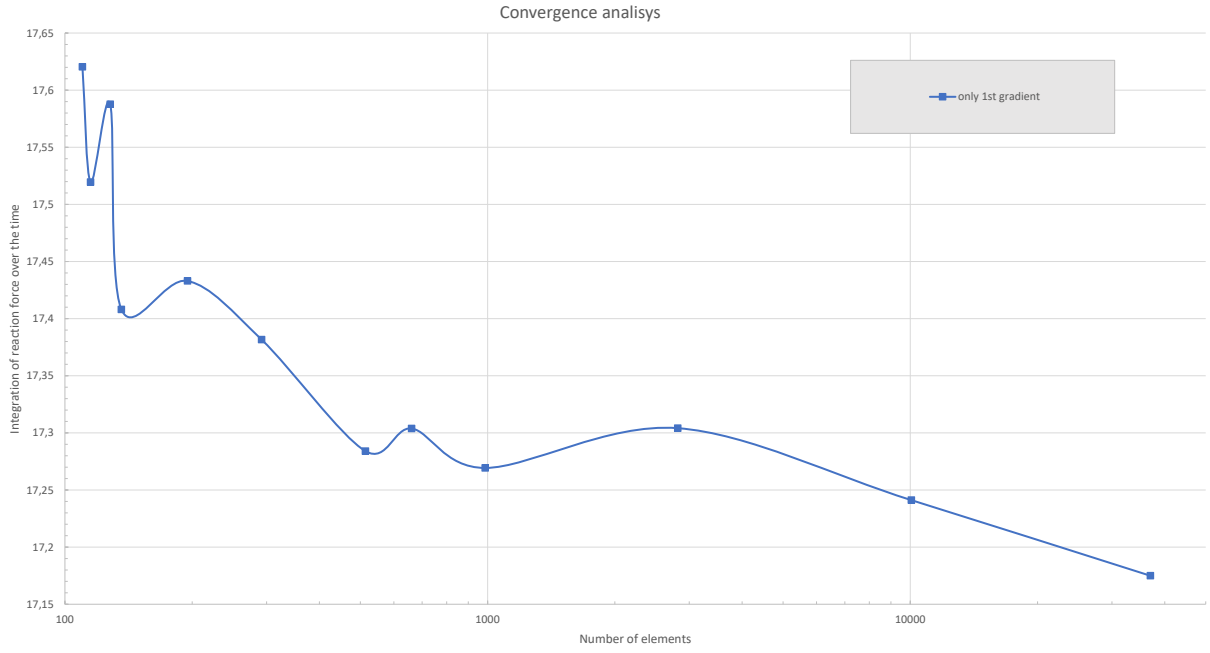

Figure 5.4: Diagram of integration the reaction force over the time versus number of finite elements from convergence analysis without implementation of strain gradient

degrees of freedom	number of elements	Maximum element size	Reaction force	Integration over the *t*
660 (plus 660 internal DOFs)	110	0,1	88,64	19,5598
706 (plus 702 internal DOFs)	117	0,08	82,94	18,562
734 (plus 732 internal DOFs)	122	0,066	82,18	18,4343
968 (plus 1002 internal DOFs)	167	0,04	80,39	18,1514
1252 (plus 1326 internal DOFs)	221	0,026	80,67	18,2078
1720 (plus 1866 internal DOFs)	311	0,02	80,56	18,1968
2866 (plus 3192 internal DOFs)	532	0,0134	80,35	18,0792
3544 (plus 3978 internal DOFs)	663	0,0106	80,24	18,1218
5206 (plus 5916 internal DOFs)	986	0,008	80,19	18,1218
14914 (plus 17388 internal DOFs)	2898	0,004	80,18	18,1952
51430 (plus 60804 internal DOFs)	10134	0,002	79,99	18,0683
187460 (plus 223350 internal DOFs)	37225	0,001	79,99	18,0746

Figure 5.5: Data from convergence analysis with implementation of strain gradient for different mesh sizes

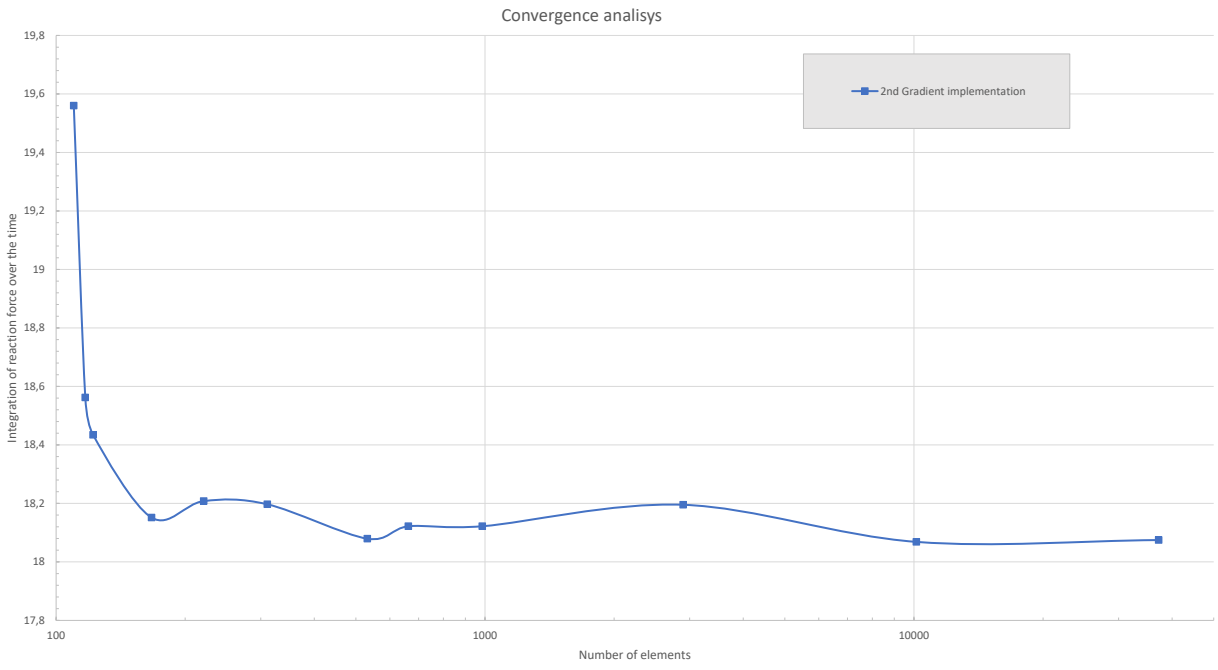

Figure 5.6: Diagram of integration the reaction force over the time versus number of finite elements from convergence analysis with implementation of strain gradient

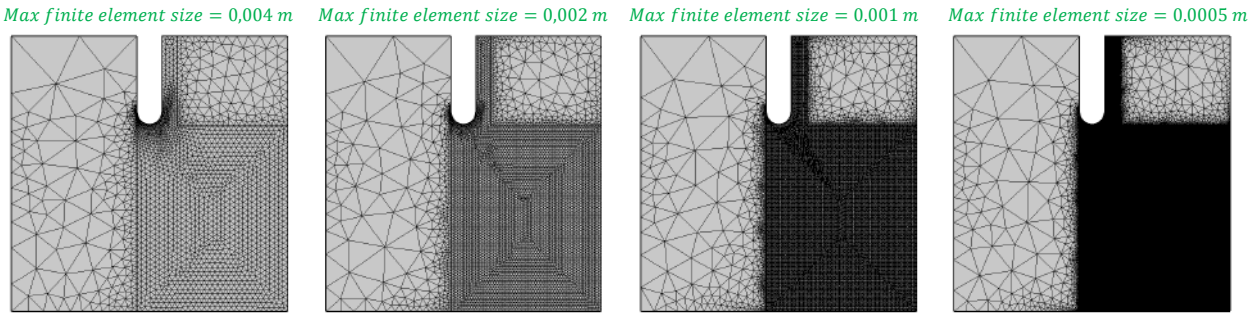

Figure 5.7: Representation of mesh with different maximum finite element size.

5.16showed the results for applied velocity v=1,375 m/s. On Figs. 5.17, 5.18 and 5.19 showed the results for applied velocity v=3,268 m/s. On Figs. 5.20, 5.21and 5.22 showed the results for applied velocity v=4,298 m/s. The path and character of the fracture correspond to the experimental data. For a low loading rate the propagation is almost vertical, with increasing applied velocity we can see the inclination of the fracture and also phenomena of branching. For the applied velocity v=1,375 m/s the angle in the begging is the same like in experimental data. However at the end fracture arrived in the different point of the boundary. For the applied velocity v=3,375 m/s one can see branching. For the applied velocity v=4,298 m/s we can see multiple branching. This difference we can explain in the way, that it was not correspond that all twelve experimental specimens were done from the same concrete and have exactly the same properties. As well it is not enough the statistics and some errors could occur during the experiments. Any way numerical simulations is the way to predict the behavior and could be improved.

One can observe loading rate effect. As slower the applied velocity as less maximum reaction force has the specimen, as faster the applied velocity as more imposed displacement has the specimen to reach the maxim value of reaction force 5.23. But it need different simulation time to get the maximum reaction force because the increment depends from loading rate. It would be worth to note that the kinetic energy occurs only on the area in the direction of loading. Kinetic energy evolves on one side of the fracture. Increasing applied velocity one can see the growing of order of magnitude of the kinetic energy. All this phenomena are due to the inertia forces.

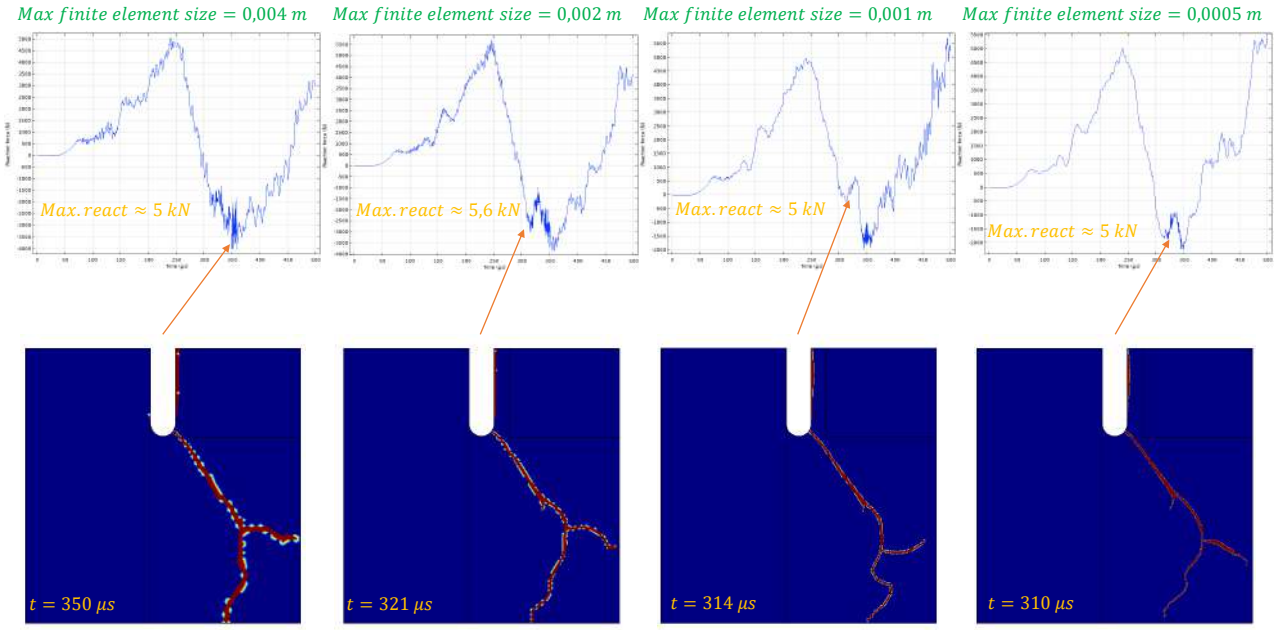

Figure 5.8: Representation of reaction force versus time diagrams (the first row) and damage contour plots (the second row) with respect to different maximum finite element size.

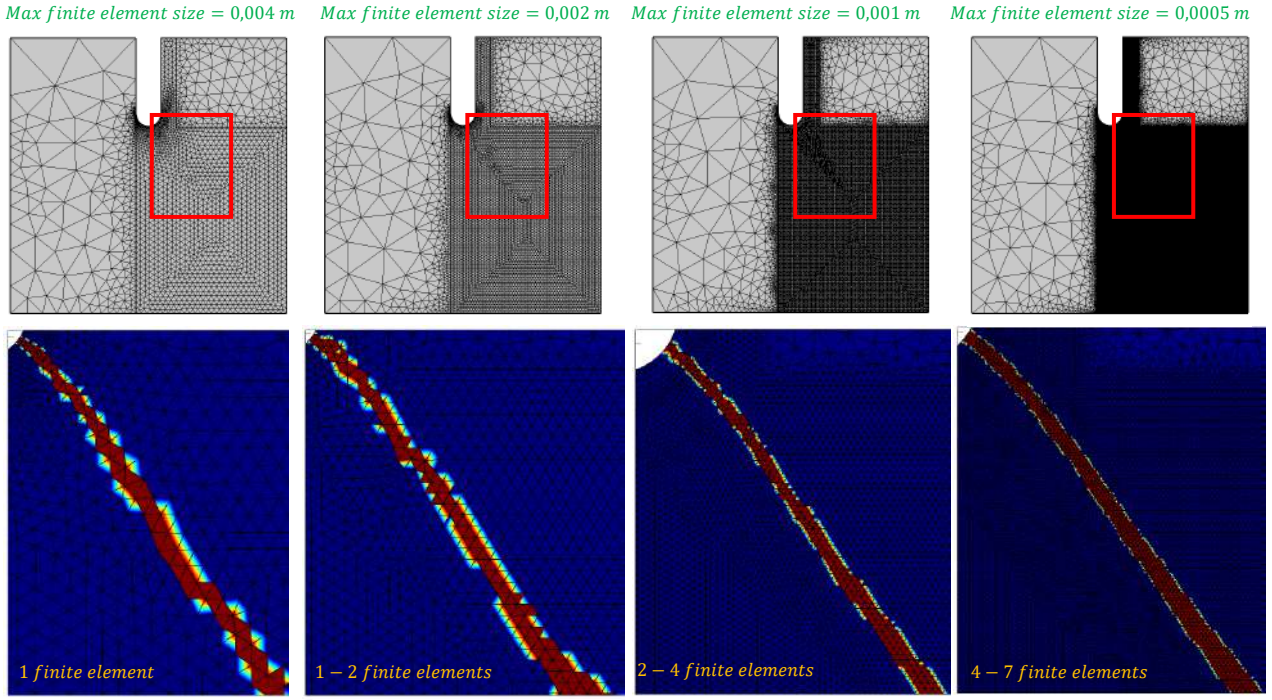

Figure 5.9: Comparison of thickness of the fracture with different maximum finite element size in central area.

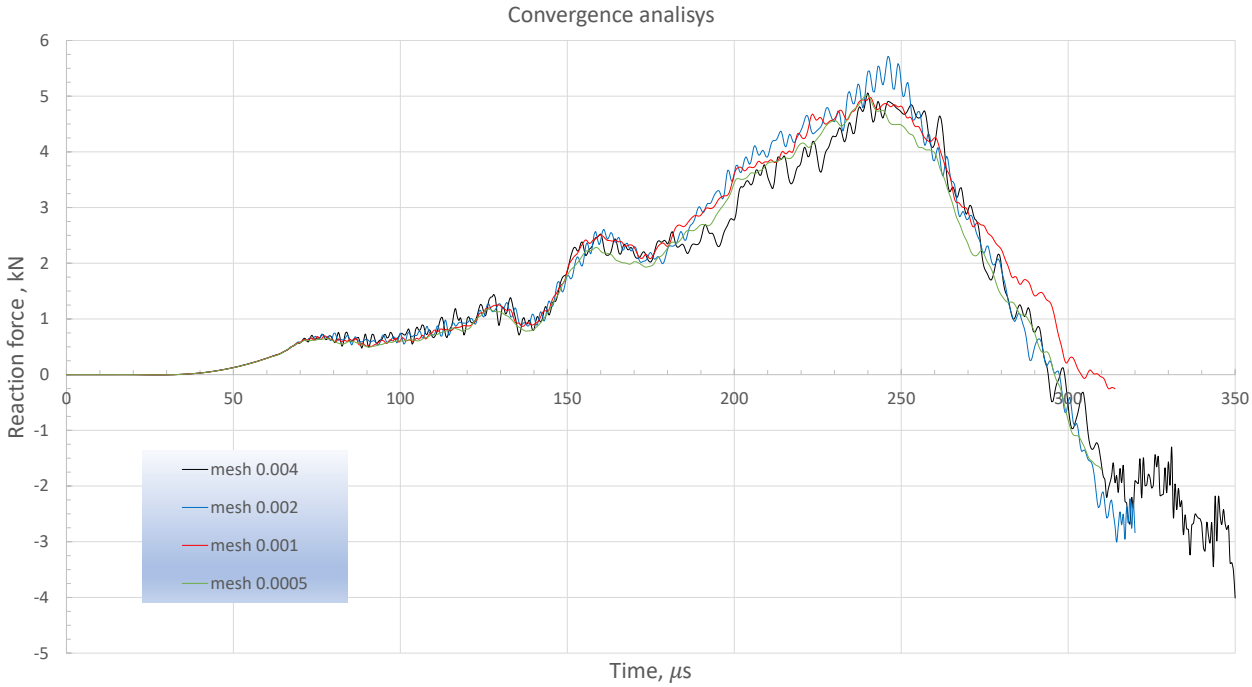

Figure 5.10: Comparison of reaction force diagram versus time for different maximum finite element size.

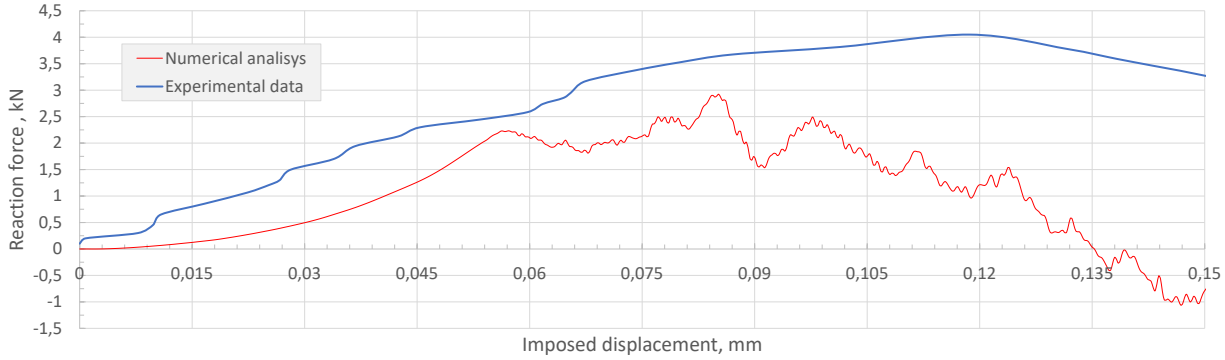

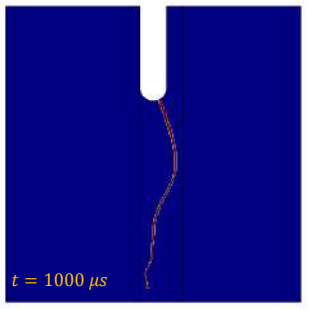

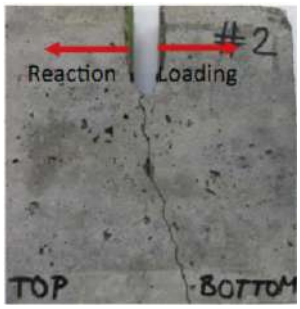

	Numerical simulation	Experimental data
Maximum reaction force	2,88 kN	4,05 kN
Imposed displacement	0,085 mm	0,12 mm
Character of fracture	Single crack	Single crack

Figure 5.11: Comparison of numerical simulation results with experimental test for applied velocity v=0,491 m/s.

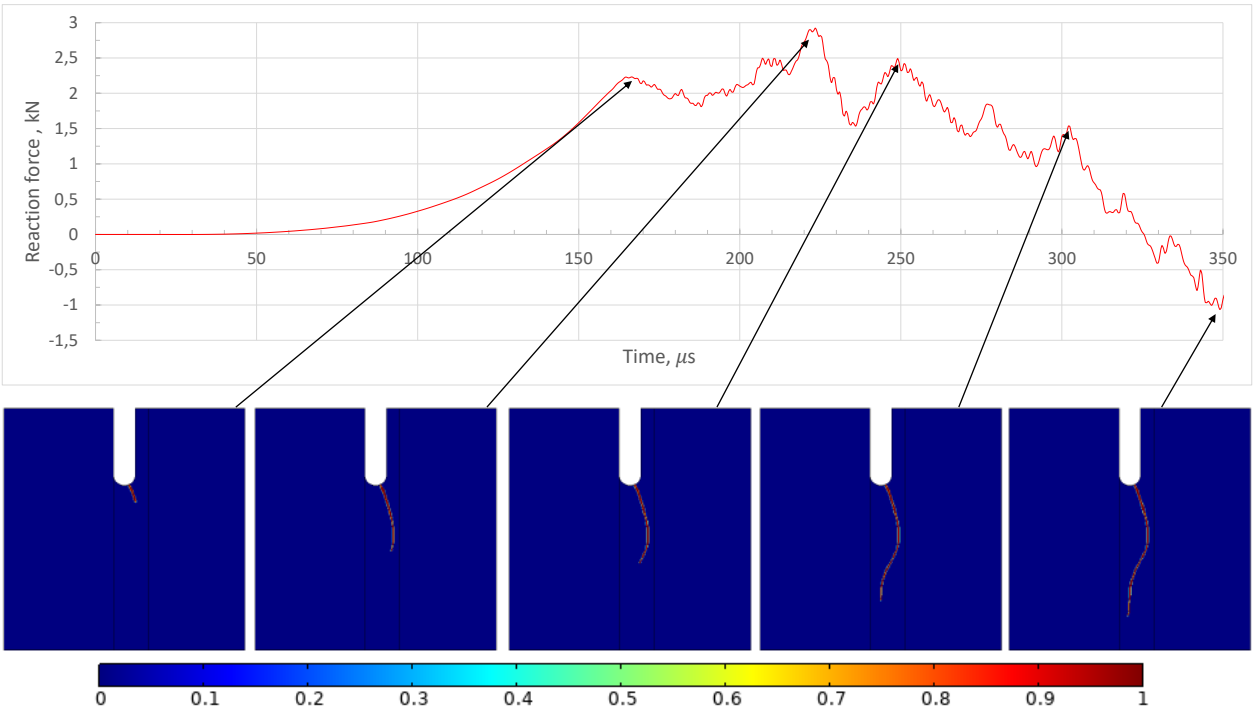

Figure 5.12: Contour plots of evolution of damage for applied velocity v=0,491 m/s.

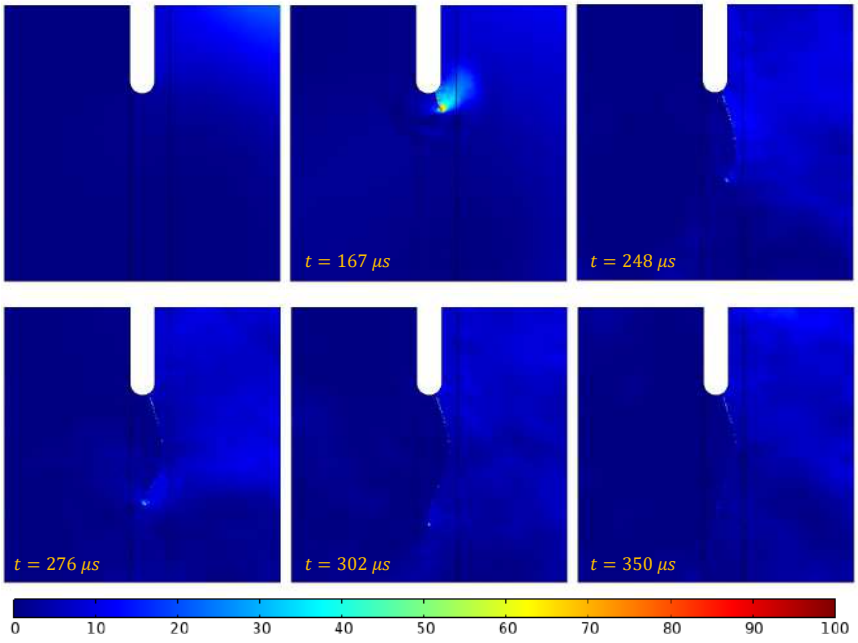

Figure 5.13: Contour plots of evolution of kinetic energy for applied velocity v=0,491 m/s.

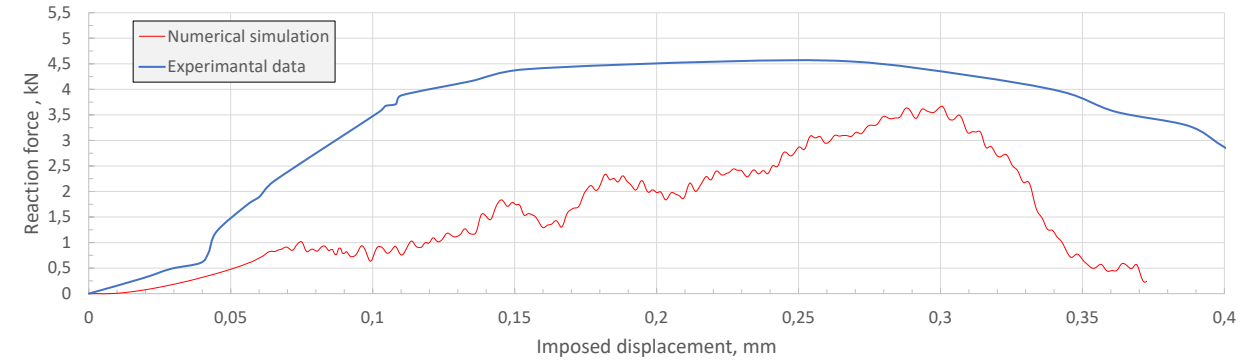

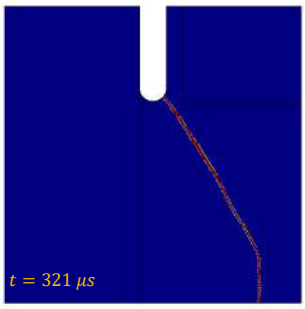

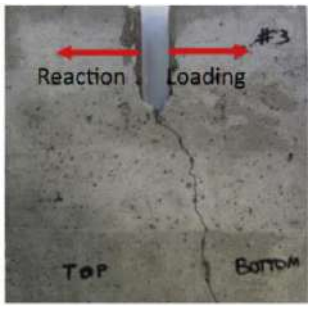

	Numerical simulation	Experimental data
Maximum reaction force	3,68 kN	4,64 kN
Imposed displacement	0,3 mm	0,28 mm
Character of fracture	Single crack	Single crack

Figure 5.14: Comparison of numerical simulation results with experimental test for applied velocity v=1,375 m/s.

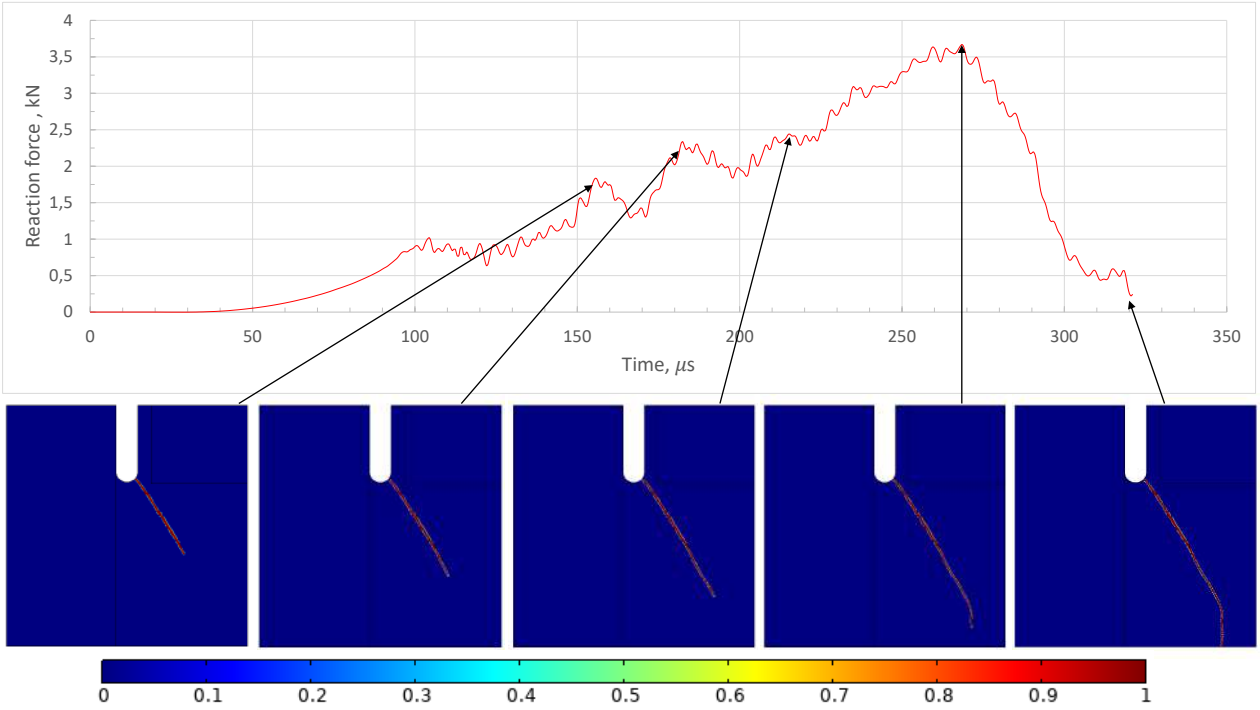

Figure 5.15: Contour plots of evolution of damage for applied velocity v=1,375 m/s.

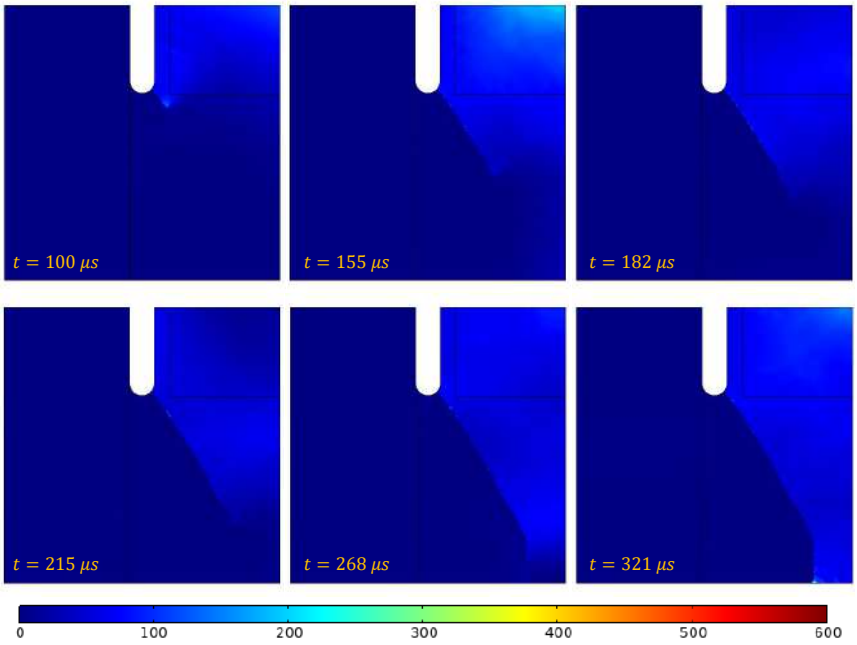

Figure 5.16: Contour plots of evolution of kinetic energy for applied velocity v=1,375 m/s.

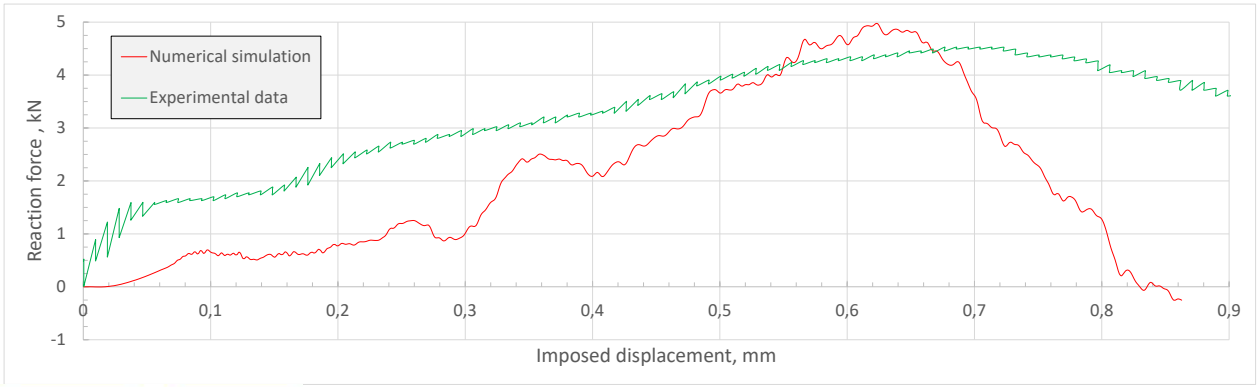

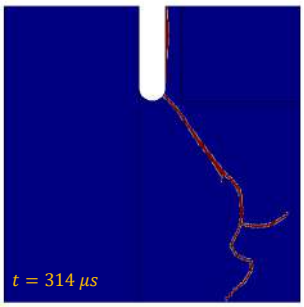

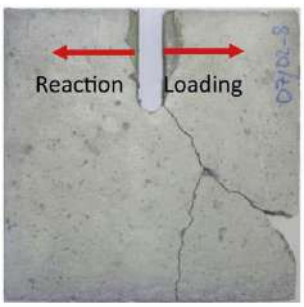

	Numerical simulation	Experimental data
Maximum reaction force	4,99 kN	4,59 kN
Imposed displacement	0,63 mm	0,68 mm
Character of fracture	Branching	Branching

Figure 5.17: Comparison of numerical simulation results with experimental test for applied velocity v=3,268 m/s.

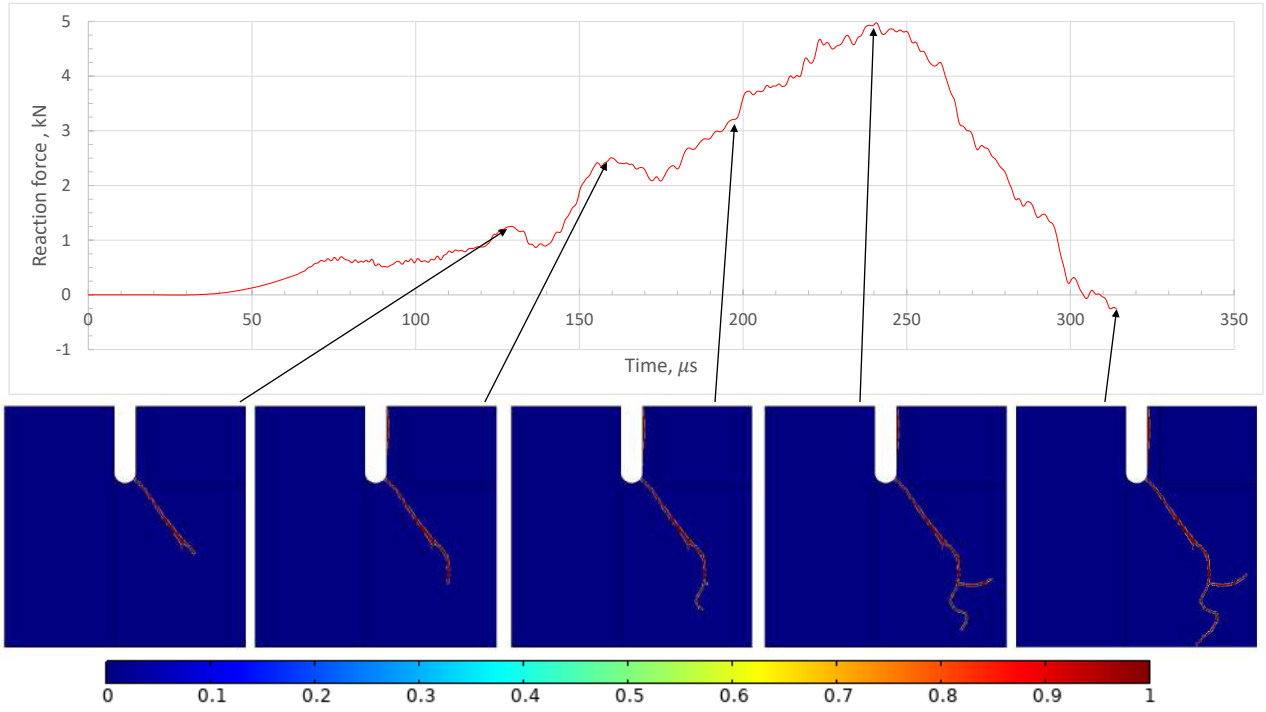

Figure 5.18: Contour plots of evolution of damage for applied velocity v=3,268 m/s.

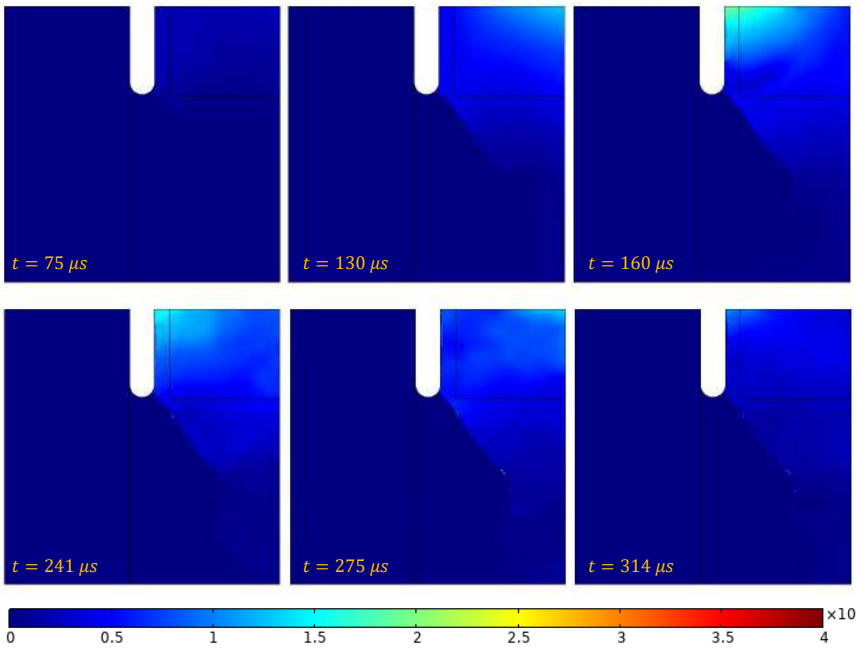

Figure 5.19: Contour plots of evolution of kinetic energy for applied velocity v=3,268 m/s.

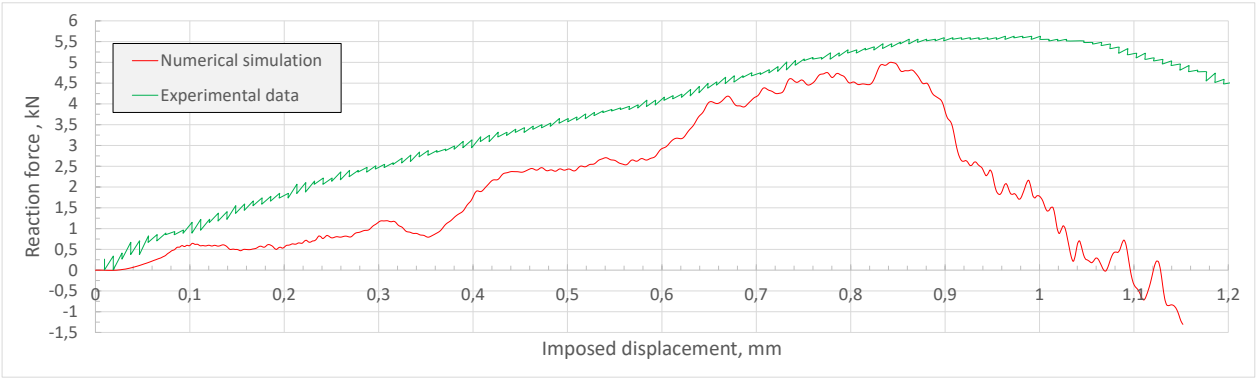

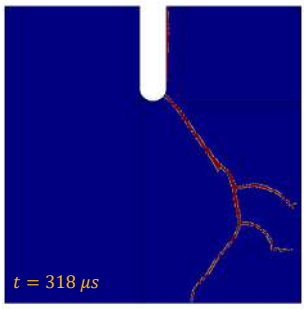

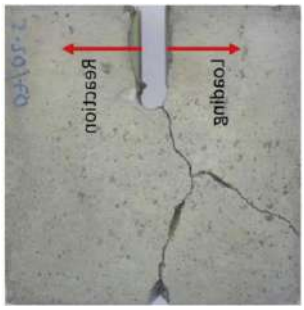

	Numerical simulation	Experimental data
Maximum reaction force	5,00 kN	5,66 kN
Imposed displacement	0,85 mm	0,99 mm
Character of fracture	Multiple branching	Branching

Figure 5.20: Comparison of numerical simulation results with experimental test for applied velocity v=4,298 m/s.

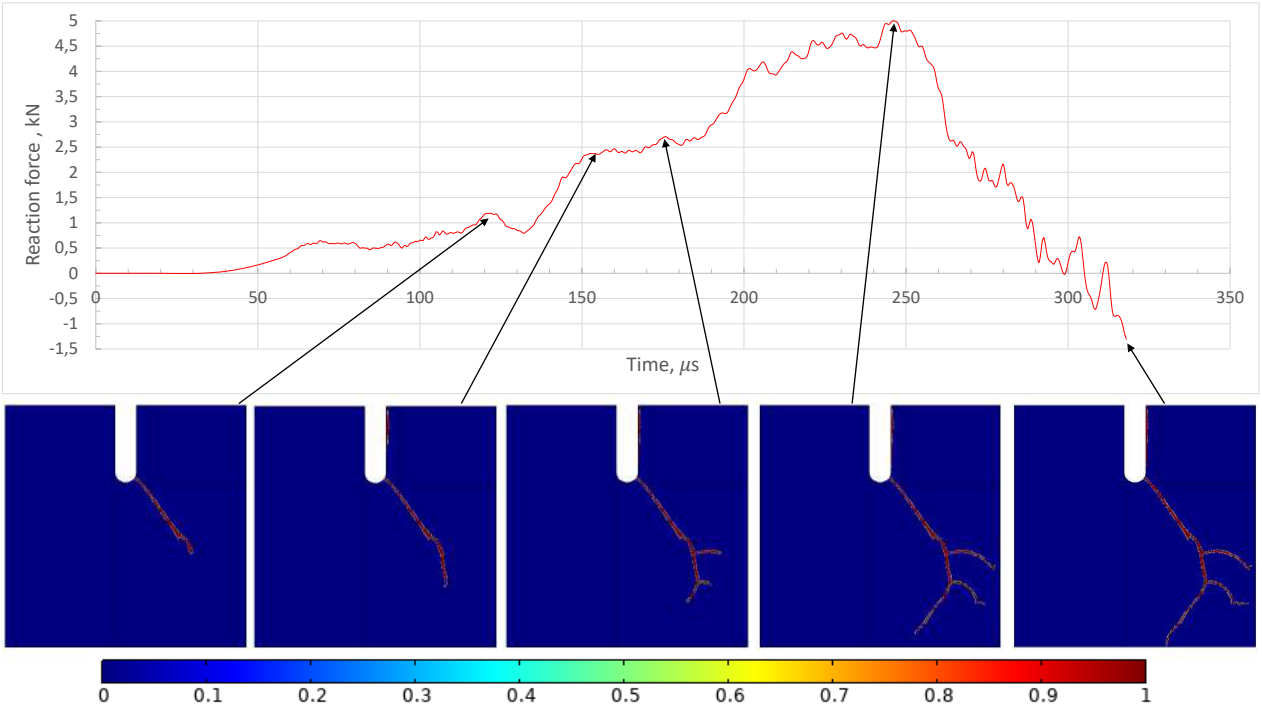

Figure 5.21: Contour plots of evolution of damage for applied velocity v=4,298 m/s.

Figure 5.22: Contour plots of evolution of kinetic energy for applied velocityv=4,298 m/s.

Figure 5.23: Comparison of diagrams reaction force versus imposed displacement for di erent loading rate.

Chapter 6

Conclusion and perspectives

The main findings of the work can be listed as follows:

- For non-homogeneous deformations, every material point of a continuum evolves in a different way.
- Strain gradients in the continuum model not only regularize the (elastic) results, but are necessary from a physical viewpoint to correctly describe the damage-induced evolution of the characteristic length scale as well as chirality and better characterization of anisotropy.
- Including strain gradients allow to capture size-dependent phenomena and to obtain mesh-independent boundary layer in numerical simulations.
- Except for the plastic dissipation energy, there are no additional assumptions, such as flow rules, needed to specify the plastic behavior.
- Including at micro-scale additional pantographic grain-pair interactions that store elastic energy in response to strain gradients, we can control at macro-scale the thickness of the localization zones that form as failure (fracture) nucleates from certain prescribed weakness
- Strain gradient leads to have mesh independent results in both quasi static and dynamic problems.
- Strain gradient regularization gives better convergence with respect to finite element size.
- The simulated dynamic fracture results conform the accuracy and capability of the developed approach in modeling catastrophic multiple cracks under impact loading conditions. Inertia forces were detected and show the interesting results with different loading rate.

So far, all the calculations in this work have been done in 2D Euclidean space to keep things simple. However, it would be natural for the model to move towards considering 3D space in the future. This would be challenging because it would require expensive numerical calculations. Nonetheless, it is an important step to improve the model's ability to accurately describe the mechanical behavior of real materials, such as concrete.

Bibliography

[1] B.E. Abali, W.H. Müller, and F. dell'Isola. Theory and computation of higher gradient elasticity theories based on action principles. *Archive of Applied Mechanics*, pages 1–16, 2017.

[2] M. Ambati, T. Gerasimov, and L. Lorenzis. A review on phase-field models of brittle fracture and a new fast hybrid formulation. *Computational Mechanics*, 55(2), 2015.

[3] L. Ambrosio, A. Lemenant, and G. Royer-Carfagni. A variational model for plastic slip and its regularization viaγ-convergence. *Journal of Elasticity*, 110(2):1–35, 2013.

[4] H. Amor, J-J. Marigo, and C. Maurini. Regularized formulation of the variational brittle fracture with unilateral contact: numerical experiments. *Journal of the Mechanics and Physics of Solids*, 57(8):1209–1229, 2009.

[5] Ivo Babuska and J.Tinsley Oden. Verification and validation in computational engineering and science: basic concepts. *Computer Methods in Applied Mechanics and Engineering*, 193(36):4057–4066, 2004.

[6] Emilio Barchiesi, Anil Misra, Luca Placidi, and Emilio Turco. Granular micromechanics-based identification of isotropic strain gradient parameters for elastic geometrically nonlinear deformations. *ZAMM - Journal of Applied Mathematics and Mechanics / Zeitschrift fÃŒr Angewandte Mathematik und Mechanik*, 101(11):e202100059, 2021.

[7] B. Bourdin, G. Francfort, and J-J. Marigo. Numerical experiments in revisited brittle fracture. *Journal of the Mechanics and Physics of Solids*, 48(4):797–826, 2000.

[8] B. Bourdin, G. Francfort, and J-J. Marigo. The variational approach to fracture. *Journal of elasticity*, 91(1):5–148, 2008.

[9] Stella Brach, Erwan Tanné, Blaise Bourdin, and Kaushik Bhattacharya. Phase-field study of crack nucleation and propagation in elastic–perfectly plastic bodies. *Computer Methods in Applied Mechanics and Engineering*, 353:44–65, 2019.

[10] Tinh Quoc Bui, Hung Tran, Xiaofei Hu, and Cheng-Tang Wu. Simulation of dynamic brittle and quasi-brittle fracture: a revisited local damage approach. *International Journal of Fracture*, 236(3-4):59–85, 2022.

[11] Cadoni, E., Caverzani, A., and di Priscoi, M. Dynamic behaviour of hpfrcc in tension. *EPJ Web of Conferences*, 26:01014, 2012.

[12] Pietro Carrara, Marreddy Ambati, Roberto Alessi, and Laura De Lorenzis. A framework to model the fatigue behavior of brittle materials based on a variational phase-field approach. *Computer Methods in Applied Mechanics and Engineering*, 361:112731, 2020.

[13] Chih-Hung Chen, Eran Bouchbinder, and Alain Karma. Instability in dynamic fracture and the failure of the classical theory of cracks. *Nature Physics*, 13(12):1186–1190, Dec 2017.

[14] B. Chiaia, O. Kumpyak, L. Placidi, and V. Maksimov. Experimental analysis and modeling of two-way reinforced concrete slabs over different kinds of yielding supports under short-term dynamic loading. *Engineering Structures*, 96:88–99, 2015.

[15] L. Contrafatto, M. Cuomo, and L. Greco. Meso-scale simulation of concrete multiaxial behaviour. *European Journal of Environmental and Civil Engineering*, pages 1–16, 2016.

[16] Yehui Cui, Xiangguo Zeng, Vincent B.C. Tan, and Zhilang Zhang. Experimental and numerical studies of niti dynamic fracture behaviors under the impact loading. *International Journal of Mechanical Sciences*, 235:107724, 2022.

[17] M. Cuomo and A. Nicolosi. A poroplastic model for hygro-chemo-mechanical damage of concrete. In *EURO-C; Computational modelling of concrete structures Conference, EURO-C; Computational modelling of concrete structures*, pages 533–542, 2006.

[18] Michele De Angelo, Luca Placidi, Nima Nejadsadeghi, and Anil Misra. Non-standard timoshenko beam model for chiral metamaterial: Identification of stiffness parameters. *Mechanics Research Communications*, 103:103462, 2020.

[19] Francesco dell'Isola and Stefano Vidoli. Continuum modelling of piezoelectromechanical truss beams: an application to vibration damping. *Archive of Applied Mechanics*, page 19, 1998.

[20] O. Essersi, Mostapha Tarfaoui, S. Boyd, R.A. Shenoi, and F. Meraghni. Experimental study of dynamic behaviour of aluminum/aluminum and composite/composite double lap joints. *Applied Mechanics and Materials*, 62:155–163, 8 2011.

[21] Jianguang Fang, Chengqing Wu, Timon Rabczuk, Chi Wu, Guangyong Sun, and Qing Li. Phase field fracture in elasto-plastic solids: a length-scale insensitive model for quasi-brittle materials. *Computational Mechanics*, 66(4):931–961, 2020.

[22] F. Freddi and G. Royer-Carfagni. Plastic flow as an energy minimization problem. numerical experiments. *Journal of Elasticity*, 1(116):53–74, 2014.

[23] Francesco Freddi and Gianni Royer Carfagni. Phase-field slip-line theory of plasticity. *Journal of the Mechanics and Physics of Solids*, 94, 04 2016.

[24] M. Froli and G. Royer-Carfagni. A mechanical model for the elastic–plastic behavior of metallic bars. *International journal of solids and structures*, 37(29):3901–3918, 2000.

[25] F. Galvez, D. Cendon, N. Garcia, A. Enfedaque, and V. Sanchez-Galvez. Dynamic fracture toughness of a high strength armor steel. *Engineering Failure Analysis*, 16(8):2567–2575, 2009. Special issue honouring Professor Manuel Elices on the occasion of his 70th birthday.

[26] I. Giorgio. Numerical identification procedure between a micro-cauchy model and a macro-second gradient model for planar pantographic structures. *Zeitschrift für angewandte Mathematik und Physik*, 67(4)(95), 2016.

[27] I. Giorgio, R. Grygoruk, F. dell'Isola, and D.J. Steigmann. Pattern formation in the three-dimensional deformations of fibered sheets. *Mechanics Research Communications*, 69:164–171, 2015.

[28] Ivan Giorgio, Alessandro Ciallella, and Daria Scerrato. A study about the impact of the topological arrangement of fibers on fiber-reinforced composites: Some guidelines aiming at the development of new ultra-stiff and ultra-soft metamaterials. *International Journal of Solids and Structures*, 203:73–83, 2020.

[29] Ivan Giorgio, Antonio Culla, and Dionisio Del Vescovo. Multimode vibration control using several piezoelectric transducers shunted with a multiterminal network. *Archive of Applied Mechanics*, 79(9):859–879, 2009.

[30] Ivan Giorgio, Francesco dell'Isola, and Anil Misra. Chirality in 2d cosserat media related to stretch-micro-rotation coupling with links to granular micromechanics. *International Journal of Solids and Structures*, 202:28–38, 2020.

[31] Ivan Giorgio, Philip Harrison, Francesco dell'Isola, Jafar Alsayednoor, and Emilio Turco. Wrinkling in engineering fabrics: a comparison between two different comprehensive modelling approaches. *Proceedings of the Royal Society A*, 474, 2018.

[32] Lu Hai and Jie Li. A rate-dependent phase-field framework for the dynamic failure of quasi-brittle materials. *Engineering Fracture Mechanics*, 252:107847, 2021.

[33] P. Harrison, D. Anderson, M.F. Alvarez, E. Bali, and Y. Mateos. Measuring and modelling the in-plane bending stiffness and wrinkling behaviour of engineering fabrics. *EUROMECH Colloquium 569: Multiscale Modeling of Fibrous and Textile Materials, Chatenay-Malabry*, 2016.

[34] Ri hong Cao, Rubing Yao, Tao Hu, Changsong Wang, Kaihui Li, and Jingjing Meng. Failure and mechanical behavior of transversely isotropic rock under compression-shear tests: Laboratory testing and numerical simulation. *Engineering Fracture Mechanics*, 241:107389, 2021.

[35] Xu Huang, Amir Reza Tabkhi, Vahid Sadeghian, and Oh-Sung Kwon. Impact of loading rate during hybrid simulation on seismic response of steel structures. *Earthquake Engineering & Structural Dynamics*, 51(12):2813–2836, 2022.

[36] H.H. Jama, G.N. Nurick, M.R. Bambach, R.H. Grzebieta, and X.L. Zhao. Steel square hollow sections subjected to transverse blast loads. *Thin-Walled Structures*, 53:109–122, 2012.

[37] A. Kezmane, B. Chiaia, O. Kumpyak, V. Maksimov, and L. Placidi. 3d modelling of reinforced concrete slab with yielding supports subject to impact load. *European Journal of Environmental and Civil Engineering*, 21(7-8):988–1025, 2017.

[38] K. Khaled and Gouda Mohamed. Modelling of the influence of tensile test speed on the fracture load. *ASM Science Journal*, 12:2019, 12 2019.

[39] Aditya Kumar, Blaise Bourdin, Gilles A Francfort, and Oscar Lopez-Pamies. Revisiting nucleation in the phase-field approach to brittle fracture. *Journal of the Mechanics and Physics of Solids*, 142:104027, 2020.

[40] J. Larsen, Christopher. A new variational principle for cohesive fracture and elastoplasticity. *Mechanics Research Communications*, 58:133 – 138, 2014.

[41] Qinghua Li, Xiao Jiang, Tian Zeng, and Shilang Xu. Experimental investigation on strain rate effect of high-performance fiber reinforced cementitious composites subject to dynamic direct tensile loading. *Cement and Concrete Research*, 157:106825, 2022.

[42] T.Y. Li, J-J. Marigo, D. Guilbaud, and S. Potapov. Variational approach to dynamic brittle fracture via gradient damage models. In *Applied mechanics and materials*, volume 784, pages 334–341. Trans Tech Publ, 2015.

[43] K K Mahato, M Biswal, D K Rathore, R K Prusty, K Dutta, and B C Ray. Effect of loading rate on tensile properties and failure behavior of glass fibre/epoxy composite. *IOP Conference Series: Materials Science and Engineering*, 115(1):012017, feb 2016.

[44] J-J. Marigo, C. Maurini, and K. Pham. An overview of the modelling of fracture by gradient damage models. *Meccanica*, 2016.

[45] Corrado Maurini, Francesco Dell'Isola, and Joël Pouget. On models of layered piezoelectric beams for passive vibration control. *Journal de Physique IV Colloque*, page 10, 2004.

[46] Vaclav Mentl and Jan Dzugan. Impact compression and tensile testing by means of a charpy pendulum. In *WIT Transactions on The Built Environment*, volume 98, pages 55–61, 2008.

[47] R. D. Mindlin. Micro-structure in linear elasticity. *Archive for Rational Mechanics and Analysis*, 16(1):51–78, Jan 1964.

[48] A. Misra. Effect of asperity damage on shear behavior of single fracture. *Engineering Fracture Mechanics*, 69(17):1997–2014, 2002.

[49] A. Misra and P. Poorsolhjouy. Granular micromechanics model for damage and plasticity of cementitious materials based upon thermomechanics. *Mathematics and Mechanics of Solids*, page 1081286515576821, 2015.

[50] A.l Misra and V. Singh. Thermomechanics-based nonlinear rate-dependent coupled damage-plasticity granular micromechanics model. *Continuum Mechanics and Thermodynamics*, 27(4-5):787, 2015.

[51] Anil Misra, Placidi Luca, and Emilio Turco. Variational methods for discrete models of granular materials. *Encylopedia of continuum mechanics. Berlin: Springer-Verlag. Heidelberg, ISBN: 978-3-662-53605-6, doi: 10.1007/978-3-662-53605-6*, 2020.

[52] Anil Misra, Nima Nejadsadeghi, Michele De Angelo, and Luca Placidi. Chiral metamaterial predicted by granular micromechanics: verified with 1d example synthesized using additive manufacturing. *Continuum Mechanics and Thermodynamics*, pages 1–17, 2020.

[53] Nima Nejadsadeghi, Luca Placidi, Maurizio Romeo, and Anil Misra. Frequency band gaps in dielectric granular metamaterials modulated by electric field. *Mechanics Research Communications*, 95:96–103, 2019.

[54] Zdzisław Nowak, Zbigniew L. Kowalewski, and Tadeusz Szymczak. Low velocity perforation of thick magnesium alloy am60 plates impacted by rigid conical-nose impactor. *Archives of Civil and Mechanical Engineering*, 23(1):5, Oct 2022.

[55] William L Oberkampf, Timothy G Trucano, and Charles Hirsch. Verification, validation, and predictive capability in computational engineering and physics . *Applied Mechanics Reviews*, 57(5):345–384, 12 2004.

[56] J. Ožbolt, K. K. Rah, and D. Meštrović. Influence of loading rate on concrete cone failure. *International Journal of Fracture*, 139(2):239–252, May 2006.

[57] Joško Ožbolt, Josipa Bošnjak, and Emiliano Sola. Dynamic fracture of concrete compact tension specimen: Experimental and numerical study. *International Journal of Solids and Structures*, 50(25):4270–4278, 2013.

[58] Joško Ožbolt, Akanshu Sharma, and Hans-Wolf Reinhardt. Dynamic fracture of concrete - compact tension specimen. *International Journal of Solids and Structures*, 48(10):1534–1543, 2011.

[59] Benoit Paermentier, Steven Cooreman, Patricia Verleysen, Sarath Chandran, Sam Coppieters, and Reza Talemi. A dynamic tensile tear test methodology to characterise dynamic fracture behaviour of modern high-grade pipeline steels. *Engineering Fracture Mechanics*, 272:108687, 2022.

[60] Anoop Kumar Pandouria, Sanjay Kumar, and Vikrant Tiwari. Experimental study of dynamic fracture behavior of al7075-t651 under different loading rates. *Materials Today Communications*, 33:104529, 2022.

[61] Sansit Patnaik and Fabio Semperlotti. Variable-order fracture mechanics and its application to dynamic fracture. *npj Computational Materials*, 7(1):27, Feb 2021.

[62] L. Placidi. A variational approach for a nonlinear 1-dimensional second gradient continuum damage model. *Continuum Mechanics and Thermodynamics*, 27(4-5):623, 2015.

[63] L. Placidi, U. Andreaus, and I. Giorgio. Identification of two-dimensional pantographic structure via a linear d4 orthotropic second gradient elastic model. *Journal of Engineering Mathematics*, pages 1–21, 2016.

[64] Luca Placidi. A variational approach for a nonlinear one-dimensional damage-elasto-plastic second-gradient continuum model. *Continuum Mechanics and Thermodynamics*, 28(1-2):119–137, 2016.

[65] Luca Placidi and Emilio Barchiesi. Energy approach to brittle fracture in strain-gradient modelling. *Proceedings of the Royal Society A: Mathematical, Physical and Engineering Sciences*, 474(2210):20170878, 2018.

[66] Luca Placidi, Emilio Barchiesi, and Anil Misra. A strain gradient variational approach to damage: a comparison with damage gradient models and numerical results. *Mathematics and Mechanics of Complex Systems*, 6(2):77–100, 2018.

[67] Luca Placidi, Anil Misra, and Emilio Barchiesi. Two-dimensional strain gradient damage modeling: a variational approach. *Zeitschrift für angewandte Mathematik und Physik*, 69(3):56, 2018.

[68] Luca Placidi, Anil Misra, and Emilio Barchiesi. Simulation results for damage with evolving microstructure and growing strain gradient moduli. *Continuum Mechanics and Thermodynamics*, 31(4):1143–1163, 2019.

[69] Leslie Philip Pook. *Linear elastic fracture mechanics for engineers: theory and applications*. WIT press, 2000.

[70] Payam Poorsolhjouy and Anil Misra. Effect of intermediate principal stress and loading-path on failure of cementitious materials using granular micromechanics. *International Journal of Solids and Structures*, 108:139–152, 2017.

[71] K. Ravi-Chandar and W. G. Knauss. An experimental investigation into dynamic fracture: I. crack initiation and arrest. *International Journal of Fracture*, 25(4):247–262, Aug 1984.

[72] K. Ravi-Chandar and W. G. Knauss. An experimental investigation into dynamic fracture: Ii. microstructural aspects. *International Journal of Fracture*, 26(1):65–80, Sep 1984.

[73] K. Ravi-Chandar and W. G. Knauss. An experimental investigation into dynamic fracture: Iii. on steady-state crack propagation and crack branching. *International Journal of Fracture*, 26(2):141–154, Oct 1984.

[74] K. Ravi-Chandar and W. G. Knauss. An experimental investigation into dynamic fracture: Iv. on the interaction of stress waves with propagating cracks. *International Journal of Fracture*, 26(3):189–200, Nov 1984.

[75] B. Reddy. The role of dissipation and defect energy in variational formulations of problems in strain-gradient plasticity. part 1: polycrystalline plasticity. *Continuum Mechanics and Thermodynamics*, 23:527–549, 2011.

[76] B. Reddy. The role of dissipation and defect energy in variational formulations of problems in strain-gradient plasticity. part 2: Single-crystal plasticity. *Continuum Mechanics and Thermodynamics*, 23:527–549, 2011.

[77] D. Scerrato, I. Giorgio, A. Della Corte, A. Madeo, N. Dowling, and F. Darve. Towards the design of an enriched concrete with enhanced dissipation performances. *Cement and Concrete Research*, 84:48–61, 2016.

[78] D. Scerrato, I. Giorgio, A. Della Corte, A. Madeo, and A. Limam. A micro-structural model for dissipation phenomena in the concrete. *International Journal for Numerical and Analytical Methods in Geomechanics*, 2015.

[79] Daria Scerrato, Ivan Giorgio, Angela Madeo, Ali Limam, and Felix Darve. A simple non-linear model for internal friction in modified concrete. *International Journal of Engineering Science*, 80, 02 2014.

[80] L. E. Schwer. An overview of the ptc 60/v& v 10: Guide for verification and validation in computational solid mechanics. *Eng. with Comput.*, 23(4):245–252, dec 2007.

[81] Kazuki Shibanuma, Shengwen Tu, Shota Suzuki, Zhuocheng Yu, Ryoma Kato, and Asato Hatamoto. Ductile crack propagation path depending on material properties: Experimental results and discussions based on numerical simulations. *Materials & Design*, 223:111158, 2022.

[82] P. Sicsic and J-J. Marigo. From gradient damage laws to griffith's theory of crack propagation. *Journal of Elasticity*, pages 1–20, 2013.

[83] Yury Solyaev. Steady-state crack growth in nanostructured quasi-brittle materials governed by second gradient elastodynamics. *Applied Sciences*, 13(10), 2023.

[84] M. Spagnuolo, K. Barcz, A. Pfaff, F. dell'Isola, and P. Franciosi. Qualitative pivot damage analysis in aluminum printed pantographic sheets: numerics and experiments. *Mechanics Research Communications*, 2017.

[85] Erwan Tanné, Tianyi Li, Blaise Bourdin, J-J Marigo, and Corrado Maurini. Crack nucleation in variational phase-field models of brittle fracture. *Journal of the Mechanics and Physics of Solids*, 110:80–99, 2018.

[86] The Minerals Metals & Materials Society (TMS). *Verification & Validation of Computational Models Associated with the Mechanics of Materials*. TMS, Pittsburgh, PA, 2019.

[87] Keiro Tokaji, Takeshi Ogawa, and Yukio Harada. Evaluation on limitation of linear elastic fracture mechanics for small fatigue crack growth. *Fatigue & Fracture of Engineering Materials & Structures*, 10(4):281–289, 1987.

[88] Ali Reza Torabi, Kazem Hamidi, Abdol Saleh Rahimi, and Sergio Cicero. Notch fracture in polymeric specimens under compressive stresses: The role of the equivalent material concept in estimating the critical stress of polymers. *Applied Sciences*, 11(5), 2021.

[89] Ilia Vindokurov, Yulia Pirogova, Mikhail Tashkinov, and Vadim V. Silberschmidt. Effect of heat treatment on elastic properties and fracture toughness of fused filament fabricated peek for biomedical applications. *Polymers*, 14(24), 2022.

[90] Ola Wall. Dynamic crack propagation in large steel specimens. *Engineering Fracture Mechanics*, 69(7):835–849, 2002.

[91] Pan Wu, Feng Yang, Ziguang Chen, and Florin Bobaru. Stochastically homogenized peridynamic model for dynamic fracture analysis of concrete. *Engineering Fracture Mechanics*, 253:107863, 2021.

[92] Junrui Xu, Dong Cao, Junjia Cui, Xu Zhang, and Guangyao Li. Experimental research on tensile behavior of advanced high-strength steel dp600 at high strain rate. *Journal of Materials Engineering and Performance*, 28(4):2411–2420, Apr 2019.

[93] S.L. Yan, H. Yang, H.W. Li, and G.Y. Ren. Experimental study of macro-micro dynamic behaviors of 5a0x aluminum alloys in high velocity deformation. *Materials Science and Engineering: A*, 598:197–206, 2014.

[94] Wen Yang, Vincent R. Sherman, Bernd Gludovatz, Eric Schaible, Polite Stewart, Robert O. Ritchie, and Marc A. Meyers. On the tear resistance of skin. *Nature Communications*, 6(1):6649, Mar 2015.

[95] Y. Yang and A. Misra. Micromechanics based second gradient continuum theory for shear band modeling in cohesive granular materials following damage elasticity. *International Journal of Solids and Structures*, 49(18):2500–2514, 2012.

[96] M E Yildizdag, Luca Placidi, and Emilio Turco. Modeling and numerical investigation of damage behavior in pantographic layers using a hemivariational formulation adapted for a hencky-type discrete model. *Continuum Mechanics and Thermodynamics*, pages 1–14, 2022.

[97] Bo Yin and Michael Kaliske. Fracture simulation of viscoelastic polymers by the phase-field method. *Computational Mechanics*, 65(2):293–309, Feb 2020.

[98] Bin Zhang, Jin Wang, Yang Wang, Yu Wang, and Ziran Li. Strain-rate-dependent tensile response of ti-5al-2.5sn alloy. *Materials*, 12(4):659, feb 2019.

[99] Ming zhi Xing, Yong gang Wang, and Zhao xiu Jiang. Dynamic fracture behaviors of selected aluminum alloys under three-point bending. *Defence Technology*, 9(4):193–200, 2013.

[100] W.Z. Zhong, I.A. Mbarek, A. Rusinek, R. Bernier, T. Jankowiak, and G. Sutter. Development of an experimental set-up for dynamic force measurements during impact and perforation, coupling to numerical simulations. *International Journal of Impact Engineering*, 91:102–115, 2016.

[101] G. Zou, C. Zhao, Z. Chang, W. Zhao, Y. Fan, S. Liu, and B. Zhang. Experimental study on dynamic fracture toughness of compact tension specimens. *Experimental Techniques*, 43(1):57–64, Feb 2019.